

---

QUANTUM METROLOGY WITH  
EINSTEIN-PODOLSKY-ROSEN  
ENTANGLED ATOMS

---

Von der QUEST-Leibniz-Forschungsschule der  
Gottfried Wilhelm Leibniz Universität Hannover

zur Erlangung des Grades

**Doktor der Naturwissenschaften**  
**- Dr. rer. nat. -**

genehmigte Dissertation von

M. Sc. Ilka Kruse, geb. Geisel,  
geboren am 05.10.1987 in Hamburg

2015

**Referent:** PD Dr. Carsten Klempt,  
Institut für Quantenoptik, Leibniz Universität Hannover

**Korreferent:** Prof. Dr. Wolfgang Ertmer,  
Institut für Quantenoptik, Leibniz Universität Hannover

**Korreferent:** Prof. PhD Géza Tóth,  
Department of theoretical physics, University of the Basque  
Country

**Tag der Promotion:** 14.12.2015

# ABSTRACT

---

The fascination of entanglement lies both in its importance to the fundamentals of quantum mechanics as well as in its various applications. The realization of highly correlated Einstein-Podolsky-Rosen (EPR) entangled states is of fundamental interest, since it provides a basis to test the validity of quantum mechanics. The applications of entangled states in quantum information include quantum cryptography and quantum key distribution. Another interesting application is quantum-enhanced metrology where non-classical states enhance the precision of atom interferometers. This thesis comprises advances towards the fundamental scientific aspects as well as metrological applications.

This work presents the first realization of EPR entanglement with massive particles. Spin-changing collisions in a Bose-Einstein condensate create EPR correlations between the  $m_F = \pm 1$  Zeeman sub-levels of the  $F = 1$  ground state of  $^{87}\text{Rb}$ . These correlations arise between phase and amplitude quadratures of the system. We show an EPR entanglement parameter of  $0.18(3)$ , which is 2.4 standard deviations below the EPR threshold of  $1/4$ . The state also satisfies the inseparability criterion with a value of  $0.85$ , which is 15 standard deviations below the classical limit of 2. Furthermore, we fully reconstruct the underlying many-particle state by quantum state tomography.

The second main result of this thesis is the demonstration of a sub-shot-noise frequency standard. A three-mode interferometer is initialized with a two-mode squeezed vacuum state in two input ports, while the third input port is populated with a classical Bose-Einstein condensate. This scheme is highly versatile, due to the fact that the preparation of the squeezed vacuum state is independent of the number of particles within the interferometer or the exact interferometer sequence, making it easily transferable to different experimental situations. Our frequency standard shows a minimal fractional instability of  $6.1 \cdot 10^{-10}$  and a sensitivity of 1.5 dB below shot-noise.

In summary, our results show a new method to utilize entangled states of matter to outperform the precision of classical interferometry which is independent of the system size. They open a path for novel tests of quantum mechanics with massive particles.

**Key words:** Einstein-Podolsky-Rosen entanglement, quantum metrology, automatized optimization



# ZUSAMMENFASSUNG

---

Die Faszination von Verschränkung liegt sowohl in ihrer Bedeutung für die Grundlagen der Quantenmechanik als auch in ihren zahlreichen Anwendungen. Die Erzeugung von stark korrelierten Einstein-Podolsky-Rosen verschränkten Zuständen ist von fundamentalem Interesse, da sie eine Basis zur Überprüfung der Gültigkeit der Quantenmechanik bietet. Anwendungen im Bereich der Quanteninformatik beinhalten Quantenverschlüsselung sowie Quantenschlüsselaustausch. Eine weitere interessante Anwendung ist die quantenverstärkte Präzisionsmetrologie. Diese Doktorarbeit umfasst sowohl grundlegende wissenschaftliche Aspekte als auch metrologische Anwendungen.

Die folgende Arbeit präsentiert die erste Realisierung von EPR Verschränkung mit massebehafteten Teilchen. Spin-ändernde Stöße in einem Bose-Einstein Kondensat erzeugen EPR Korrelationen zwischen den  $m_F = \pm 1$  Zeeman Unter-niveaus des  $F = 1$  Grundzustands in  $^{87}\text{Rb}$ . Diese Korrelationen treten zwischen den Quadraturen der Phase und der Amplitude des Systems auf. Wir zeigen einen EPR Verschränkungsparameter von  $0.18(3)$ , der die EPR Schwelle von  $1/4$  um  $2.4$  Standardabweichungen unterschreitet. Mit einem Wert von  $0.85$  unterbietet der Zustand ebenso die klassische Grenze des Inseparabilitätskriteriums von  $2$  um  $15$  Standardabweichungen. Des Weiteren rekonstruieren wir den zugrunde liegenden Viel-Teilchen Zustand vollständig durch Quantenzustandstomographie.

Das zweite Hauptergebnis dieser Arbeit ist die Demonstration eines Frequenzstandards unterhalb des Schrotrauschlimits. Ein drei-Moden Interferometer wird in zwei Eingängen mit einem zwei-Moden gequetschten Vakuumzustand initialisiert, während der dritte Eingang mit einem klassischen Bose-Einstein-Kondensat bevölkert wird. Da dieses System unabhängig von der Anzahl der Teilchen im Interferometer und der genauen Interferometer-Sequenz ist, kann es leicht an geänderte experimentelle Gegebenheiten angepasst werden. Unser Frequenzstandard hat eine minimale partielle Instabilität von  $6.1 \cdot 10^{-10}$  und eine Sensitivität die  $1.5$  dB unter der Schrotrauschgrenze liegt.

Zusammenfassend zeigen unsere Ergebnisse eine neue Methode, die unter Ausnutzung von verschränkten Zuständen von Materie die Genauigkeit eines klassischen Interferometers, unabhängig von der Größe des Systems, unterbietet. Zusätzlich eröffnen die vorgestellten Resultate neue Möglichkeiten zur Überprüfungen der Quantenmechanik mit massebehafteten Teilchen.

**Schlagwörter:** Einstein-Podolsky-Rosen-Verschränkung, Quantenmetrologie, automatisierte Optimierung



# CONTENTS

---

<b>1</b>	<b>Introduction</b>	<b>1</b>
<b>2</b>	<b>Entanglement in atomic ensembles</b>	<b>5</b>
2.1	Entangled states . . . . .	5
2.1.1	Representation of spins . . . . .	6
2.1.2	Dicke states and spin squeezing . . . . .	8
2.1.3	Entanglement witnesses . . . . .	9
2.2	Methods to create entangled atoms . . . . .	13
2.2.1	Quantum non-demolition measurements . . . . .	13
2.2.2	One-axis twisting Hamiltonian . . . . .	15
2.2.3	Two-mode squeezing . . . . .	16
2.3	Experimental realization . . . . .	18
2.3.1	Preparing the atomic ensemble . . . . .	18
2.3.2	Spin dynamics process . . . . .	22
<b>3</b>	<b>Einstein-Podolsky-Rosen correlations</b>	<b>27</b>
3.1	The original EPR proposal . . . . .	27
3.2	Inferred Heisenberg inequalities . . . . .	30
3.2.1	EPR variables for the two-mode squeezed state . . . . .	32
3.2.2	Atomic homodyning . . . . .	34
3.2.3	Analysis of the experimental data . . . . .	37
3.3	Full state tomography . . . . .	39
3.3.1	Maximum Likelihood analysis and state reconstruction . . . . .	41
3.4	One-way steering . . . . .	47
<b>4</b>	<b>Sub-shot-noise interferometry</b>	<b>51</b>
4.1	Introduction to interferometry . . . . .	51
4.1.1	Atom interferometry . . . . .	52
4.1.2	Atomic clocks . . . . .	54
4.1.3	Sub-shot-noise interferometry . . . . .	56

---

4.2	The three-mode interferometer . . . . .	57
<b>5</b>	<b>Automatized optimization</b>	<b>67</b>
5.1	The optimization algorithm . . . . .	67
5.1.1	Differential Evolution . . . . .	68
5.1.2	Limited Lifetime Differential Evolution . . . . .	70
5.2	Simulation . . . . .	71
5.3	Experimental application . . . . .	74
<b>6</b>	<b>Outlook</b>	<b>79</b>
	<b>List of publications</b>	<b>97</b>
	<b>Curriculum vitae</b>	<b>99</b>



---

# INTRODUCTION

Today, entanglement is viewed as one of the core features of quantum mechanics. Due to this close link, entangled states of particles can be used to perform tests of quantum mechanics. At the same time, these highly correlated states are interesting for applications such as quantum-enhanced metrology. The possibilities to realize entangled states of particles in an experimental laboratory setting have drastically increased in the last decades. Experimental research on entanglement started in photonic systems with the investigation of pair-wise entanglement in 1950 [1]. A source produces two beams, typically called signal and idler beam, where each photon from the first beam is entangled with one photon from the second beam. The sources of pair-wise entanglement have been improved tremendously to create bright states of squeezed vacuum with up to 2500 photons per beam [2]. The maximum number of entangled photon has advanced to up to eight photons [3]. In solid state systems tripartite entanglement has been demonstrated in superconducting circuits [4] as well as in defect centers in diamond [5]. In ionic systems, entanglement of up to 14 atoms has been realized [6].

Several approaches have been used to create entanglement in neutral atomic ensembles. On the one hand, conditional approaches, such as schemes relying on quantum non-demolition measurements, are investigated. They have been used to generate entanglement between two macroscopic atomic ensembles [7] as well as spin-squeezing in an atomic ensemble inside a cavity [8]. Measurement-based schemes can also be used to create entangled states of around 3000 atoms by the detection of a single photon [9]. On the other hand, non-conditional approaches can be applied to atomic systems. A non-linear interaction can be used to provide a so-called one-axis twisting Hamiltonian that induces spin squeezing in the ensemble [10]. The interaction strength can be tuned by either varying the scattering length via Feshbach resonances [11] or by adjusting the trap overlap

for the involved states [12]. A two-mode squeezed state in an atomic system can be realized by a process comparable to parametric down conversion in optics experiments [13–16]. These atomic entangled states can be used both for fundamental research as well as applications such as quantum-enhanced metrology.

The discussion of entanglement started in 1935 when Einstein, Podolsky and Rosen published their seminal paper on the completeness of quantum mechanics [17]. They consider a highly correlated system of two spatially separated particles with two non-commuting observables like position and momentum. The outcome of possible measurements has a continuous spectrum and these observables are therefore called continuous variables. The measurement of position or momentum of one particle can now be used to predict the outcome of the measurement of the other particle with absolute certainty. This is possible, even though a classical interaction of these two particles is prohibited. Due to their concept of "*physical reality*", which is nowadays known as local realism, they argue that the measurement results would have had to be predetermined. This led to the conclusion that quantum mechanics must be incomplete. Today, this discrepancy of local realism with quantum mechanics is known as the EPR paradox. The type of continuous variable correlations that are needed for the EPR paradox are termed EPR entanglement. In his reply, Schrödinger coined the term "*entanglement*" for this type of correlation. He also introduced the idea of the measurement on one particle "*steering*" the outcome of the measurement on the other particle [18, 19].

EPR entanglement with continuous variables was first experimentally demonstrated by Ou et al. [20] with a two-mode squeezed vacuum state generated via optical down-conversion. Today, the highest degree of EPR entanglement is 27.7 dB below the classical limit [21]. Even though realizations with photons have the advantage of easier spatial separation compared to massive particles, EPR entangled states with massive particles are highly desirable. Their close similarity to the original EPR proposal and the fact that they may be more tightly bound to the concept of local realism [22, 23] makes them an interesting object to study. While inseparability has been shown for Gaussian states of two collective atomic modes [7, 15, 24], the stronger EPR entanglement has not yet been shown in massive particles.

We utilize spin-changing collisions to create a two-mode squeezed vacuum state in an ultracold ensemble. This state has an EPR entanglement parameter of 0.18(3), which is 2.4 standard deviations below the threshold of 1/4. The state is fully characterized by a tomographic reconstruction of the underlying many-particle quantum state. This reconstruction is obtained via an unbiased Maximum Likelihood algorithm.

Schrödinger's reply to the original EPR paper and his discussion of "*steering*" already revealed the directionality of the EPR entanglement [18]. While most

experiments to demonstrate EPR entanglement rely on the symmetry of the system, it is possible to show steering in one direction, while it is prohibited in the other. This has first been realized in an optical system with two entangled Gaussian modes [25]. We use a conceptually similar approach to demonstrate this one-way steering in an atomic system.

Not only is entanglement very interesting from a fundamental point of view, it can also be utilized in various applications like sub-shot-noise interferometry. The same two-mode squeezed state that shows these strong EPR correlations can also improve an atomic frequency standard. The sensitivity of atom interferometers with classical input states is bound by the standard quantum limit (SQL), stemming from the shot noise in the experiment. With entangled input states this limit can be overcome, as has been shown in multiple experiments [15, 26–28]. However, the measurement of a physical property with a sensitivity below the SQL is not trivial. The following table shows an overview of measurements below the SQL.

Ref.	measurement type	system	preparation	sensitivity below SQL [dB]
[29]	magnetometer	laser cooled atoms	QND measurement	2.0
[30]	magnetometer	BEC	one-axis twisting Hamiltonian	3.8
[24]	magnetometer	atoms at room temperature	QND measurement	1.5
[31]	magnetometer	nuclear spin of molecule	Hadamard and C-NOT gate	19.5
[32]	microwave intensity	BEC	one-axis twisting Hamiltonian	4
[33]	clock	laser cooled atoms	QND measurement	1.1
[34]	clock	atoms in a cavity	QND measurement	4.5
[35]	clock	ions	generalized Ramsey pulses	0.75

In all these experiments, the interferometers have been enhanced, by populating both interferometer states symmetrically with an entangled many body state. This has the disadvantage, that the generation of these input states is typically highly dependent on the particle number. Therefore, a simple increase in atom number, which also enhances the sensitivity of the interferometer, necessitates and adjustment of the process used for the generation of entanglement.

It has been shown in optics that the sensitivity of an interferometer can also be improved by initializing one of the input ports by a squeezed vacuum state instead of leaving it dark [36]. While this technique is widely used in optics experiments [37], it has not previously been demonstrated in an atom optics setup. Here we show the first realization of such a sub-shot-noise interferometer and build a frequency standard with a sensitivity of 1.5 dB below the SQL. This frequency standard is based on a novel three mode interferometry scheme, which is insensitive to magnetic field fluctuations in first order.

The presented thesis is structured as follows. The second chapter gives an introduction into the characterization of entangled states, before discussing different methods to create entangled states in atomic systems. The apparatus used for the experiments in the following chapters is presented and the spin dynamics process that generates a two-mode squeezed state in this system is reviewed. In the third chapter the realization of Einstein-Podolsky-Rosen entanglement in an atomic system is presented. After an overview of the original EPR proposal, the EPR variables for the two-mode squeezed state are discussed and a full tomography of the state is presented. The directionality of EPR entanglement is examined and first experimental data presented. The fourth chapter discusses the use of sub-shot-noise interferometry for frequency standards. It gives an overview of the use of interferometers in modern atom optics before presenting the sub-shot-noise frequency standard, that is realized by squeezing the vacuum state of one of the interferometric input ports. In the fifth chapter, an introduction to optimization approaches is given before presenting a solution for optimizing an atom optic experiment in the presence of a noisy environment, based on an evolutionary algorithm. The final chapter summarizes the main results of this thesis and gives an outlook to future work.

---

# ENTANGLEMENT IN ATOMIC ENSEMBLES

In his 1935 reply to the just previously published Einstein-Podolsky-Rosen paradox (EPR paradox) [17], Schrödinger coined the term "Verschränkung" as well as the notion of separability. Verschränkung, later translated as "entanglement", and separability are now basic concepts of modern quantum mechanics [18, 19]. Schrödinger suggested that the paradox of entanglement solves itself by degradation of the state as the entangled parties move apart, such that EPR correlated states are not physically realizable. A detailed discussion of the EPR paradox as well as the generalization of EPR correlations and their experimental realization will be presented in chapter 3.

The following chapter will first formally define entanglement and methods to quantify it, before presenting some experimental realizations of spin-squeezed systems. The experimental procedure that has been used for the experiments in the following chapters is presented and the preparation of an entangled state via spin dynamics is explained.

## 2.1 Entangled states

The mathematical description of any quantum-mechanical system utilizes a Hilbert space  $\mathcal{H}$ . Pure states of the system are represented by state vectors with unit length in this Hilbert space. One can now consider a multipartite system that consists of  $N$  subsystems, each represented by its own Hilbert space  $\mathcal{H}_k$ . These subsystems can for example correspond to the different particles in a physical system. The total Hilbert space  $\mathcal{H}$  is given by the tensor product of these subsystem spaces  $\mathcal{H} = \otimes_{k=1}^N \mathcal{H}_k$ .

Any pure state that doesn't show correlations can now be expressed as a tensor product of the subsystem states  $|\psi\rangle = |\psi_1\rangle \otimes \cdots \otimes |\psi_N\rangle$ , where  $\rho_i = |\psi_i\rangle\langle\psi_i|$  is the associated density matrix for each subsystem state. A measurement of

this state on the subsystem  $i$  will not influence the outcome of a following measurement on the subsystem  $j$ .

A classically correlated state however can be written as a convex linear combination of these product states

$$\rho = \sum_i p_i \rho_i^{(1)} \otimes \cdots \otimes \rho_i^{(N)}. \quad (2.1)$$

States of this form are called separable states. A state that is not separable must show more than classical correlations and is thus entangled. While this negative definition is theoretically concise it isn't well suited for an experimental proof of entanglement. For a more detailed discussion, please refer to Ref. [38]. Due to the relevance for the presented experiments, the following sections will be devoted to spin squeezed states.

### 2.1.1 Representation of spins

When dealing with composite spin systems, a visualization helps to form an intuitive idea of an experiment and its outcome. One possible approach is the use of the Bloch sphere or the Bloch vector representation. This representation was first introduced in the context of nuclear magnetic resonance [39]. It can be easily extended to the case of a two level atom [40] as well as to more complex systems with  $N$  two-level atoms.

We first consider a single two-level particle with eigenstates  $|\uparrow\rangle, |\downarrow\rangle$  of the  $\hat{\sigma}_z$  operator. The two levels can for example be realized by two energy states of the system. This two-level system can then be described in terms of the pseudo-spin operators  $\hat{s}_i$ . They are defined as

$$\begin{aligned} \hat{s}_x &= \frac{1}{2}(|\downarrow\rangle\langle\uparrow| + |\uparrow\rangle\langle\downarrow|) = \frac{1}{2}\hat{\sigma}_x \\ \hat{s}_y &= \frac{1}{2i}(|\downarrow\rangle\langle\uparrow| - |\uparrow\rangle\langle\downarrow|) = \frac{1}{2}\hat{\sigma}_y \\ \hat{s}_z &= \frac{1}{2}(|\uparrow\rangle\langle\uparrow| - |\downarrow\rangle\langle\downarrow|) = \frac{1}{2}\hat{\sigma}_z, \end{aligned} \quad (2.2)$$

where  $\hat{\sigma}_i$  are the Pauli matrices. They satisfy the commutation relations

$$[\hat{s}_i, \hat{s}_j] = i\epsilon_{ijk}\hat{s}_k, \quad (2.3)$$

with  $i, j, k$  associated to three orthogonal directions. While  $\hat{s}_z$  depends only on the population of the two spin states,  $\hat{s}_x$  and  $\hat{s}_y$  correspond to the real and imaginary parts of the coherence.

Any pure state of the system can now be written as

$$|\psi\rangle = e^{i\varphi/2} \cos \theta |\uparrow\rangle + e^{-i\varphi/2} \sin \theta |\downarrow\rangle \quad (2.4)$$

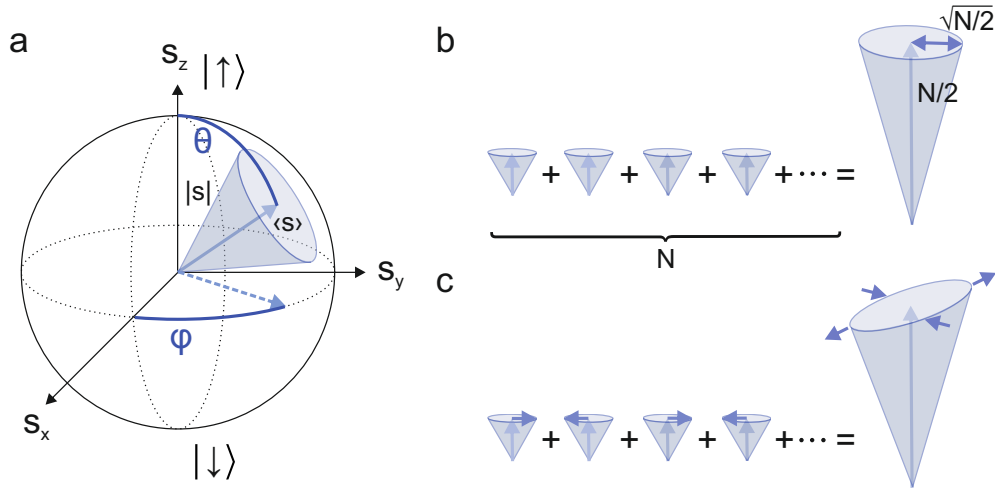


**Figure 2.1: Depiction of spin states.** **a** The spin state on the Bloch sphere is depicted as a cone, where the center of the cone corresponds to the expectation value of the spin  $\langle \vec{s} \rangle$ . The disk that is spanned by the cone corresponds to the uncertainty of the perpendicular spin components. **b** The single particle spins of a symmetric system can be added to form the collective spin of the system which has a maximum length of  $J_{\max} = N/2$ . If these spins are uncorrelated, the addition results in the coherent spin state which has equal uncertainty in both orthogonal directions. **c** If the single particle spins are appropriately correlated, the addition results in a squeezed spin state. It is characterized by the fact that the uncertainty in one direction is reduced while it is enhanced in the other. (Depiction b and c based on Ref. [10])

with  $-\frac{\pi}{2} \leq \theta < \frac{\pi}{2}, 0 \leq \varphi < 2\pi$ . The expectation values of the spin operators thus correspond to a vector

$$\langle \vec{s} \rangle = \frac{1}{2} \begin{pmatrix} \sin 2\theta \cos \varphi \\ \sin 2\theta \sin \varphi \\ \cos 2\theta \end{pmatrix} \quad (2.5)$$

on a sphere with radius  $1/2$ , where the poles represent the basis  $|\uparrow\rangle, |\downarrow\rangle$ . As shown in Fig. 2.1a, the angles  $\theta$  and  $\varphi$  are the polar coordinates of the Bloch vector. Thus, pure states of the system will be represented on the surface of the Bloch sphere. The Bloch vector of a mixed state will always lie within the Bloch sphere.

Due to the non-vanishing commutator Eq. (2.3), the Heisenberg uncertainty relation  $(\Delta s_y)^2 (\Delta s_z)^2 \geq \frac{1}{4} |\langle s_x \rangle|^2$  for the spin expectation values arises. Thus, the length  $|\vec{s}| = \sqrt{s(s+1)} = 3/4$  of the spin differs from the length  $|\langle \vec{s} \rangle| = 1/2$  of the expectation value. Therefore, the spin is better depicted as a cone, where the orientation of the cone is given by the mean  $\langle \vec{s} \rangle$  and the disc that is spanned by the cone corresponds to the uncertainty of the spin components.

This picture can now be extended to multiple spins. A collective spin can be formed by adding the individual spins of the  $N$  particles involved  $\vec{J} = \sum_{i=1\dots N} \vec{s}^{(i)}$  (See Fig. 2.1b). The collective spin operators will obey the same commutation relations given by Eq. (2.3) as the single particle operators. Thus, the collective spin operators will also be subject to the Heisenberg uncertainty relations

$$(\Delta J_k)^2(\Delta J_l)^2 \geq \frac{1}{4}|\langle J_m \rangle|^2. \quad (2.6)$$

The following will be restricted to systems that are symmetric under particle exchange, thus the collective spin is at its maximum  $J_{\max} = N/2$ . For large  $N$ , the length of the spin can be approximated as  $|\vec{J}| = \sqrt{J(J+1)} \approx J$ . In second quantization, the collective spin operators can be written as

$$\begin{aligned} J_x &= \frac{1}{2}(a^\dagger b + b^\dagger a) \\ J_y &= \frac{1}{2i}(a^\dagger b - b^\dagger a) \\ J_z &= \frac{1}{2}(a^\dagger a - b^\dagger b), \end{aligned} \quad (2.7)$$

where  $a, a^\dagger$  and  $b, b^\dagger$  are the associated annihilation and creation operators for the  $|\uparrow\rangle$  and  $|\downarrow\rangle$  states.

Using  $J_i$  instead of  $s_i$  as the axes a generalized many-particle Bloch sphere can be introduced. The Bloch vector is given by the expectation value  $\langle \vec{J} \rangle$  of the collective spin and the sphere has the a maximal radius of  $J = N/2$ . The state is again depicted as a cone or an arrow with an uncertainty ellipse. For the coherent spin state the uncertainty becomes spherical with a diameter of  $\sqrt{N}$ , directly corresponding to shot noise.

## 2.1.2 Dicke states and spin squeezing

### Spin squeezing

A collective spin state that is constructed from  $N$  uncorrelated single spins with the same expectation value  $\langle \vec{J} \rangle$  is called coherent spin state. This state satisfies the minimal uncertainty relation Eq. (2.6) with equal uncertainties in the orthogonal components as depicted in Fig. 2.1b. If one now finds a method to entangle the single-particle spins in an appropriate manner, the uncertainties in one orthogonal direction might be reduced while being enhanced in the other (see Fig. 2.1c). This state is called a spin-squeezed state [10]. The degree of squeezing of these states and their usefulness in metrological tasks can be evaluated through measures of entanglement as described in chapter 2.1.3. Different ways to experimentally produce such states are discussed in chapter 2.2.



## Dicke states

States that are simultaneous eigenstates of both the collective spin operator (or in more general cases the angular momentum operator)  $\vec{J}^2$  and its projection on the  $z$  component  $J_z$  are called Dicke states [41]. They can be expressed in terms of the effective angular momentum quantum number  $j = (N_\uparrow + N_\downarrow)/2 = N/2$  and the  $z$ -projection quantum number  $m = (N_\uparrow - N_\downarrow)/2$  as states  $|j, m\rangle$ , where  $N_\uparrow$  and  $N_\downarrow$  are the number of particles in the two spin states. Except for states with  $m = \pm j$ , Dicke states are entangled.

Symmetric Dicke states are those Dicke states that are symmetric under particle exchange and have a maximal  $J$ . The symmetric  $N$ -particle Dicke state [42] with  $m$  excitations is defined as

$$|m, N\rangle := \binom{N}{m}^{-1/2} \sum_k P_k |\uparrow_1, \dots, \uparrow_m, \downarrow_{m+1}, \dots, \downarrow_N\rangle, \quad (2.8)$$

where  $P_k$  corresponds to all  $\binom{N}{m}$  distinct permutations of the spins. The entanglement properties of the state  $|m, N\rangle$  do not change if its quantization axis is reversed  $|m - N, N\rangle$ . Dicke states  $|1, N\rangle$  with only one excitation are also known as  $W$ -states. These  $W$ -states are extremely robust against particle loss [43].

High fidelity Dicke states with small particle numbers have been created with up to 6 photons [44, 45] and up to 8 ions [46]. Different heralded approaches, relying on the detection of single photons, can be used to prepare atomic  $W$ -states with up to 2910 atoms [9, 47]. In a scheme that utilizes a fiber-optical cavity on an atom chip, 41 atoms have been prepared in a  $W$ -state [47]. It has recently been shown in Ref. [48] that quantum Zeno dynamics can also be employed for the fast creation of  $W$ -like-states with up to 36 atoms. Atomic systems can also be used to create Dicke states of the form  $|N/2, N\rangle$  with large number of atoms. Such a Dicke-like state has been realized with an entanglement depth of 68 atoms [49].

## 2.1.3 Entanglement witnesses

### Spin squeezing parameter

To quantify the amount of spin squeezing, different measures can be used. Spin-squeezing parameters that rely on the knowledge of collective angular momentum components only, have the advantage that they are experimentally useful even if individual particles cannot be addressed. The easiest spin squeezing parameter can be directly derived from the Heisenberg uncertainty Eq. (2.6).

For a spin state the mean-spin direction is defined by  $\vec{n}_0 = \frac{\langle \vec{J} \rangle}{|\langle \vec{J} \rangle|}$ . If one now considers a  $J_m$  to be parallel to the mean-spin direction  $\vec{n}_0$ , a coherent state would

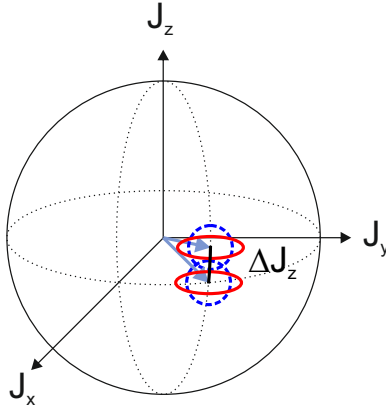


**Figure 2.2: Phase estimation visualized on the generalized Bloch sphere.** Depicted in dashed blue are the uncertainties for coherent spin states. Here the phase difference  $\Delta J_y$  can not be resolved. Depicted in solid red are the uncertainty ellipses for two spin squeezed states for which it is possible to resolve the rotation difference  $\Delta J_y$ .

yield equal uncertainties  $(\Delta J_{k,l})^2 = N/4$  in the  $k$  and  $l$  directions, where  $J_k$  and  $J_l$  are orthogonal to  $J_m$ . Spin squeezing could thus generally be defined as the case where  $(\Delta J_{\vec{n}_\perp})^2 < N/4$ . Here  $\vec{n}_\perp$  refers to a direction perpendicular to the mean-spin direction  $\vec{n}_0$ .

A squeezing parameter that quantifies the amount of squeezing can then be defined according to Ref. [10] as

$$\xi_S^2 = \frac{\min[(\Delta J_{\vec{n}_\perp})^2]}{N/4}. \quad (2.9)$$

The state is thus considered spin squeezed if  $\xi_S^2 < 1$ . However, this parameter is only meaningful if the regarded state is situated on the surface of the Bloch sphere with radius  $N/2$  and not for states inside the Bloch sphere where  $\langle \vec{J}^2 \rangle \approx 0$ .

A different spin-squeezing parameter was proposed in Ref. [50]. This spin squeezing parameter has the advantage, that it is directly related to the improvement of Ramsey-type experiments [51], which are explained in more detail in chapter 4. In these experiments, an effective rotation on the Bloch sphere, typically around  $J_y$ , is estimated. As depicted in Fig. 2.2 employing spin squeezed states can enhance the resolution of this estimation.

The associated spin squeezing parameter is defined with respect to the phase

sensitivity  $\Delta\phi_{\text{CSS}} = 1/\sqrt{N}$  of the coherent spin state as

$$\xi_R^2 = \frac{(\Delta\phi)^2}{(\Delta\phi_{\text{CSS}})^2} = \frac{\min[(\Delta J_{\vec{n}_1})^2] N}{|\langle \vec{J} \rangle|^2}. \quad (2.10)$$

The two parameters are related via  $\xi_R^2 = \left(\frac{N/2}{|\langle \vec{J} \rangle|}\right)^2 \xi_S^2$  and  $\xi_R^2 \geq \xi_S^2$  since  $N/2 \geq |\langle \vec{J} \rangle|$ .

For the symmetric state where  $|\langle \vec{J} \rangle| = N/2$ , the two measures are equal.

$\xi_R^2$  can be generalized to

$$\xi^2 = \frac{N(\Delta J_{\vec{n}_1})^2}{\langle \vec{J}_{\vec{n}_2} \rangle^2 + \langle \vec{J}_{\vec{n}_3} \rangle^2} \quad (2.11)$$

to accommodate random orthogonal directions  $\vec{n}_1, \vec{n}_2, \vec{n}_3$ , which can be useful in an experimental setup with constraints on the possible measurement directions. This generalized parameter indicates entanglement for  $\xi^2 < 1$  [52] and reduces to  $\xi_R^2$  if  $\vec{n}_2$  is chosen to be  $\vec{n}_0$  and  $\vec{n}_1 = \vec{n}_\perp$ . For the coherent state, both parameters  $\xi_R^2$  and  $\xi^2$  are equal to one. They thus indicate spin squeezing for values smaller than one.

While these spin squeezing parameters work well for most spin-squeezed states, they are not reliable for the detection of entanglement in Dicke states. Therefore a more general spin squeezing parameter has to be introduced.

### Generalized spin squeezing parameter

In their discussion of Dicke states in spinor Bose-Einstein condensates Raghavan et al. [53] propose a squeezing parameter  $\xi_D^2$  that also evaluates the entanglement of Dicke states. They argue that a state is spin squeezed along the direction  $J_{\vec{n}}$  if its expectation value  $\langle J_{\vec{n}} \rangle$  is the same as for the coherent spin state, namely  $N/2$  but the variance  $(\Delta J_{\vec{n}})^2$  is reduced. The spin squeezing parameter is thus defined as

$$\xi_D^2 = \frac{N(\Delta J_{\vec{n}})^2}{\frac{N^2}{4} - \langle J_{\vec{n}} \rangle^2}. \quad (2.12)$$

In Ref. [54] a complete set of four spin squeezing inequalities is presented, where a violation of any of the inequalities indicates entanglement. These inequalities are complete with respect to  $\langle J_i \rangle$  and  $(\Delta J_i)^2$ , meaning that each state that can possibly be detected as entangled by the knowledge of  $\langle J_i \rangle$  and  $(\Delta J_i)^2$  only is in fact detected by the inequalities. One of these inequalities can be reformulated as a generalized spin squeezing parameter

$$\xi_{\text{gen}}^2 = \frac{(N-1)(\Delta J_m)^2}{\langle J_k^2 \rangle + \langle J_l^2 \rangle - N/2}. \quad (2.13)$$

This parameter has been used to verify a spin squeezed Dicke-like state with 8000 atoms at 11.4(5) dB below shot noise and an entanglement depth of at least 28 atoms [49]. In the case of symmetric Dicke states  $\xi_{gen}^2$  and  $\xi_D^2$  are equivalent. For the coherent spin state  $\xi_D^2 = \xi_{gen}^2 = 1$ .

A more thorough overview of these squeezing parameters is given in Ref. [51].

### Quantum Fisher information

While  $\xi_R^2$  is connected to the improvement of the phase sensitivity that a spin squeezed state provides in a Ramsey-type measurement it is unable to quantify the metrological usefulness of more general states. However, it has been shown that one can introduce a criterion for entanglement that is based on the quantum Fisher information  $F_Q$  which is directly related to the usefulness of a state with respect to sub-shot-noise estimation of rotation angles [55].

The quantum Fisher information is the quantum mechanical generalization of the Fisher information that was introduced in 1925 [56]. It was developed in the framework of statistical information theory as a measure for the information content of a statistical distribution.

The Cramer-Rao bound [57], which is a fundamental limit to the phase sensitivity is given as

$$\Delta\phi_{est} \geq \frac{1}{F_Q[\rho, J_{\vec{n}}]}, \quad (2.14)$$

where  $F_Q[\rho, J_{\vec{n}}]$  is the quantum Fisher information with respect to the interferometric input state  $\rho$  and the angular momentum operator  $J_{\vec{n}}$  in an arbitrary direction.  $F_Q$  can be defined as  $F_Q[\rho, J_{\vec{n}}] = 4(\Delta R)^2$  where  $R$  is the Hamiltonian that solves  $\{R, \rho\} = i[J_{\vec{n}}, \rho]$ . While in general  $(\Delta R)^2 \leq (\Delta J_{\vec{n}})^2$  the equality is reached for pure states. From the Cramer-Rao bound the entanglement criterion

$$\chi^2 = \frac{N}{F_Q[\rho, J_{\vec{n}}]} \quad (2.15)$$

can be derived. It is the comparison of the achievable entanglement enhanced phase sensitivity to shot noise

$$\Delta\phi_{est} \geq \frac{\chi}{\sqrt{N}}. \quad (2.16)$$

The quantum Fisher information is bound by  $F_Q < N^2$  and a state shows useful entanglement if  $F_Q > N$ . The upper bound of  $\chi^2$  for any input state is given by  $\chi^2 = \xi^2$  [58].

Especially noticeable,  $\chi^2$  also provides a measure for states that are not spin squeezed but nonetheless useful for quantum enhanced metrology. An example for such a state is the maximally excited Dicke state. It has been shown in

Ref. [26] that such a state, with  $F_Q/N = 1.45$ , reaches an interferometric sensitivity of 1.61 dB under shot noise. Another example, relying on a state tomography to extract the quantum Fisher information, reaches a maximum of  $F_Q/N = 1.51$  for a superposition of Dicke states [48]. An experimental method to extract the quantum Fisher information of a state without performing a full state tomography has been presented in Ref. [59]. Here, a maximal quantum Fisher information of  $F_Q/N = 2.2$  has been obtained for a spin squeezed state.

## 2.2 Methods to create entangled atoms

There are several methods available to create ensembles of entangled atoms. The different methods operate in very different regimes of atomic ensembles reaching from atoms in hot vapor cells to Bose-Einstein condensed ensembles. Methods that are feasible for one set of experimental parameters, such as particle number, density or temperature, cannot trivially be transferred to different conditions. The following will give an overview of some experimental realizations of entangled atoms.

### 2.2.1 Quantum non-demolition measurements

Performing a quantum non-demolition measurement on the collective spin of an atomic ensemble can be used to create a spin squeezed state in the ensemble. This spin squeezed state can afterwards be employed as the input state of an interferometer. The experiment starts with a coherent state on the equator of the Bloch sphere, depicted in dashed blue in Fig. 2.3a. This state has a shot noise limited  $J_z$  uncertainty. If now a perfect  $J_z$  measurement is performed, the state collapses into a Dicke state with  $|J \approx N/2, m \approx 0\rangle$ . This state has minimal  $J_z$  uncertainty but maximal  $J_x$  and  $J_y$  uncertainty. It is depicted by the dash-dotted red line parallel to the equator. Due to the uncertainty of the coherent state the resulting state in consecutive experiments will always have a somewhat different position on the  $J_z$ -axis. This is an example for heralded state preparation, where the measurement process is a necessary condition for the entanglement. The prepared states are therefore also termed heralded Dicke states.

In order to be able to use the state for interferometry after the measurement is performed one must find a way to do a non destructive measurement. Such a measurement is also referred to as a quantum non-demolition measurement. This type of measurement is typically weaker than a destructive measurement in the sense that the information obtained in the measurement has a bigger uncertainty. That means that the state doesn't exhibit a full collapse of the wave function as in a perfect measurement. In the Bloch sphere picture this corresponds to the coherent state being squeezed along the  $J_z$  axis and anti-squeezed

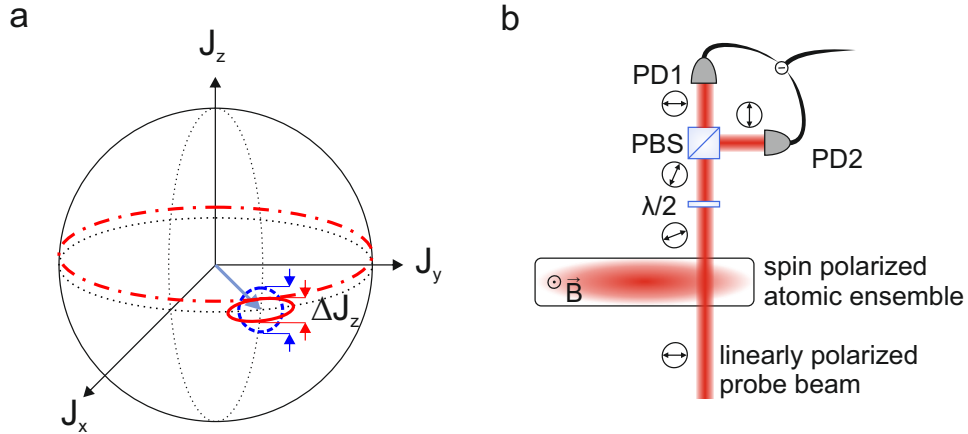


**Figure 2.3: Quantum non-demolition measurement as a tool to create spin squeezing.** **a** After a perfect  $J_z$  measurement the coherent state (dashed blue) collapses into a Dicke state (dash-dotted red) around the equator. For a weaker measurement, the state is spin squeezed (solid red). **b** The spin coherent ensemble is probed by an off resonant light field which is sent onto a polarizing beam splitter to analyze the imprinted Faraday rotation [27]. The polarization of the probe beam compared to the spin polarization axis of the ensemble determines the measurement axis of the angular momentum.

in the  $x$ - $y$ -plane (see solid red ellipse in Fig. 2.3a). Since the squeezed state doesn't necessarily have the same expectation value  $\langle J_z \rangle$  as the coherent state that is used for preparation the outcome of the quantum non-demolition measurement has to be recorded in order to use the squeezed state as an interferometric input state. This type of squeezing is called conditional squeezing.

This type of spin squeezing in atomic systems has first been demonstrated in vapor cells [60] of room temperature atoms. It can also be used to produce entanglement between two macroscopic ensembles of  $10^{12}$  atoms each [7]. Experimentally, the quantum non-demolition measurement can be realized by employing the Faraday rotation that is imprinted onto a light field when it passes through an atomic ensemble. This rotation can be measured via the polarization imbalance after probing the ensemble. To this end the probe is sent onto a polarizing beam splitter and the two outputs are measured and compared (see Fig. 2.3b). If the probing beam is chosen to be off-resonant, a quantum non-demolition measurement can be achieved.

In cold atomic systems, spin squeezing through collective measurements has been shown with atoms inside a cavity [8]. A similar cavity assisted measurement scheme was used to improve the phase resolution of a Ramsey-type experiment to 10.2(6) dB below shot noise [61].

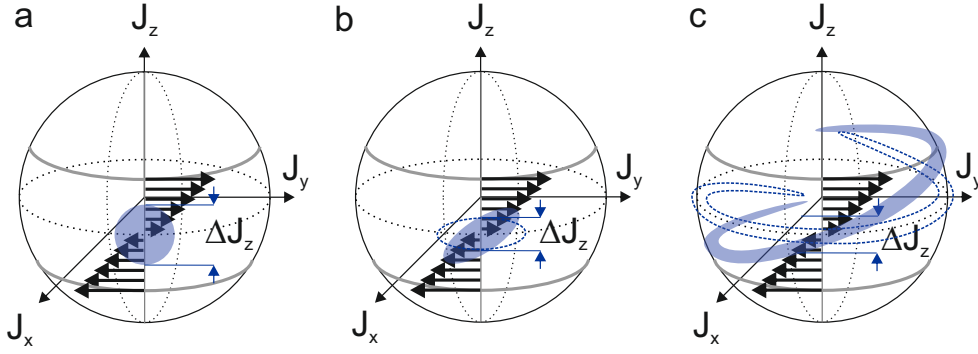


**Figure 2.4: One-axis twisting Hamiltonian depicted on the Bloch sphere.** **a** The twisting action of the one-axis twisting Hamiltonian that acts on the coherent state is depicted as black arrows. The twisting grows larger as one leaves the proximity of the equator. **b** After a certain interaction time the ideally spin squeezed state is reached. The spin squeezed axis is angled towards the  $J_z$ -axis of measurement. Thus the state has to be turned around this axis before evaluation of  $\Delta J_z$ . This is depicted as the dashed blue curve. **c** If the interaction is left on longer than the time needed for ideal squeezing an over squeezing occurs and even after the ideal rotation  $\Delta J_z$  will be larger than in the previous case. This is due to the deviation of the spin squeezed state from a perfect geodesic.

### 2.2.2 One-axis twisting Hamiltonian

The utilization of a nonlinear pairwise interactions in an atomic ensemble presents a different approach to generate spin squeezing. The one-axis twisting Hamiltonian was first proposed in Ref. [10] and is defined as

$$H_{\text{out}} = \chi J_z^2 = \frac{\chi}{4} \sum_{k,l=1}^N \sigma_{kz} \sigma_{lz}, \quad (2.17)$$

where  $\chi$  is the coupling constant and  $\sigma_{iz}$  are the single particle Pauli matrices.

The effect of the one-axis twisting Hamiltonian is depicted in Fig. 2.4. The twisting or shearing action is depicted by the black arrows on the Bloch sphere. The twisting force vanished at the equator and increases, with opposing sign, on the two hemispheres. Fig. 2.4a shows the coherent state. Fig. 2.4b shows the ideally twisted state after a certain interaction time. The squeezing of the state will be under an angle such that the state has to be rotated towards the equator if the squeezing should be transformed into a minimal  $J_z$  uncertainty. If the interaction is left on for a longer time the state is over twisted as shown in Fig. 2.4c. The uncertainty ellipse of the state will show a deviation from the

perfect geodesic and thus the uncertainty in the squeezed direction will grow larger again.

Experimentally, this Hamiltonian can be implemented by a non-linear beam splitting sequence [10]. The Hamiltonian corresponding to such a beam splitting pulse is

$$H_{nlbs} = \delta J_z + \Omega J_\phi + \chi J_z^2. \quad (2.18)$$

$\delta J_z$  leads to a precession around the  $z$ -axis, where  $\delta$  is the detuning of the coupling pulse between the two states.  $\Omega J_\phi$  describes a rotation of the spin around the axis  $J_\phi = \cos \phi J_x - \sin \phi J_y$  with the Rabi frequency  $\Omega$  and a phase  $\phi$ . The non-linear interaction is given by

$$\chi = \frac{g_{\uparrow\uparrow}}{2} \int d\vec{r} |\phi_{\uparrow}|^4 + \frac{g_{\downarrow\downarrow}}{2} \int d\vec{r} |\phi_{\downarrow}|^4 - g_{\uparrow\downarrow} \int d\vec{r} |\phi_{\uparrow}|^2 |\phi_{\downarrow}|^2, \quad (2.19)$$

where  $g_{ij}$  are the coupling constants and  $\phi_i$  the mean field wave functions [62]. In order to tune this interaction strength one can either tune the coupling constants or the wave function overlap.

Gross et al. [11] took the first approach to show that such a nonlinear process can be used to surpass the classical precision limit of an interferometer. To realize a spin-1/2 system, two hyperfine states of Bose-Einstein condensed atomic ensembles in spherical dipole traps were employed. Since they assume perfect wave function overlap the non-linear interaction  $\chi$  depends only on the difference of the intrastate and interstate couplings:  $\chi \propto g_{\uparrow\uparrow} + g_{\downarrow\downarrow} - 2g_{\uparrow\downarrow}$ . The coupling constants are proportional to the  $s$ -wave scattering lengths as  $g_{ij} = 4\pi\hbar^2 a_{ij}/m$ . The interstate scattering length  $a_{\uparrow\downarrow}$  can be tailored via a magnetic Feshbach resonance and thus the interaction  $\chi$  is tuned.

At the same time a second approach to the one-axis twisting Hamiltonian was also realized [28]. Again the spin-1/2 system is realized by two hyperfine states of a Bose-Einstein condensate, which is in this approach magnetically trapped in a chip trap. Here, the  $s$ -wave coupling constants are kept almost identical such that the interaction is governed by the spatial mode overlap. The spatial overlap is tuned by a state dependent trapping potential that introduces an energy shift to one of the states due to an off-resonant microwave coupling [12]. By completely separating the two components the interaction strength is maximized to  $\chi \propto g_{\uparrow\uparrow} + g_{\downarrow\downarrow}$ . With this approach, an improvement of 2.5 dB below the standard quantum limit is achieved.

### 2.2.3 Two-mode squeezing

The above presented squeezed states through quantum non-demolition measurement and the one-axis twisting Hamiltonian are so called one-mode squeezed states. The observed fluctuations are those of one total system described by the



collective operators  $J_i$ . Another type of spin squeezed states are two-mode squeezed states, where the entanglement of the system is between spin components of the two subsystems.

In accordance to Eq. 2.1 a bipartite state is separable if and only if it can be written as

$$\rho = \sum_i p_i \rho_i^{(1)} \otimes \rho_i^{(2)}. \quad (2.20)$$

Since the entanglement now involves the two parts of a bipartite system, a new set of observables has to be introduced. These are composed out of the single system spin operators

$$J_\alpha^\pm = J_\alpha^{(1)} \pm J_\alpha^{(2)}, \quad (2.21)$$

where  $J_\alpha^{(i)}$  are the spin operators of the single systems. A criterion for two mode squeezing can then be given as [63]

$$(\Delta J_z^{(+)})^2 + (\Delta J_y^{(-)})^2 < \langle J_x^{(+)} \rangle. \quad (2.22)$$

Atomic two mode squeezed states can also be generated by different experimental techniques such as performing a quantum non-demolition measurement on two systems [7] or by utilizing spin changing collisions in a Bose-Einstein condensate [16, 64]. The latter will be explained in more detail in chapter 2.3.2.

In optics, two-mode squeezed states are commonly produced via parametric down conversion. A coherent pump laser at frequency  $\omega_A + \omega_B$  is directed onto a nonlinear optical crystal. The nonlinearity of the crystal leads to the transformation of a pump photon into a signal and an idler photon with frequencies  $\omega_A$  and  $\omega_B$ . For a graphic representation refer to Fig. 2.5a. The entanglement properties of the signal and idler beam qualify this setup for applications in quantum information [65]. In the degenerate case, where  $\omega_A = \omega_B$ , the process can be employed for the creation of squeezed light [66].

If the depletion of the pump beam is negligible, the Hamiltonian of the process can be approximated by

$$H = i\hbar(\kappa^* \hat{a}_A^\dagger \hat{a}_B^\dagger - \kappa \hat{a}_A \hat{a}_B), \quad (2.23)$$

where  $\hat{a}_{A/B}$  are the annihilation operators for signal and idler mode. A two-mode squeezing operator can be defined with  $\xi = \kappa t$  as

$$\hat{S}(\xi) = \exp(\xi^* \hat{a}_A^\dagger \hat{a}_B^\dagger - \xi \hat{a}_A \hat{a}_B). \quad (2.24)$$

If this operator acts on the vacuum state  $|N_A, N_B\rangle = |0, 0\rangle$  it generates a two-mode squeezed state

$$\hat{S}(\xi) |0, 0\rangle = |\Psi\rangle = \sum_{n=0}^{\infty} c_n |n, n\rangle, \quad (2.25)$$

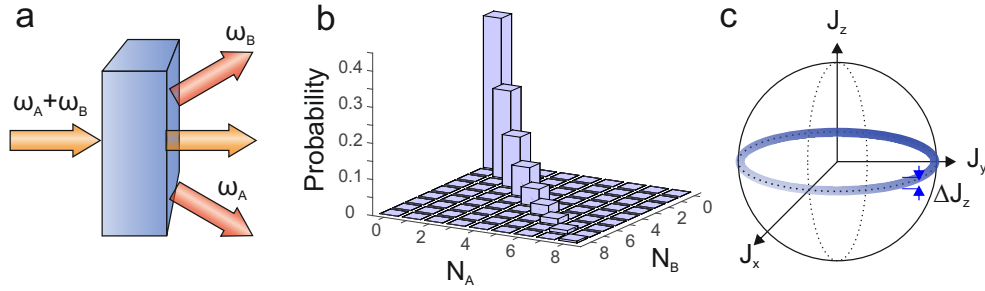


**Figure 2.5: Parametric down conversion and the two-mode squeezed state.** **a** A nonlinear medium transforms a photon from the pump beam with frequency  $\omega_A + \omega_B$  into highly entangled signal and idler photons with frequencies  $\omega_A$  and  $\omega_B$ . **b** Elements  $\langle N_A, N_B | \rho | N_A, N_B \rangle$  of the density matrix for the ideal two-mode squeezed state with  $\xi = 1$ . **c** The two-mode squeezed state can be depicted by a ring around the equator with a low uncertainty  $\Delta J_z$  in  $J_z$  direction and completely undefined  $J_x$  and  $J_y$  directions.

which is a superposition of twin-Fock states  $|N_A, N_B\rangle = |n, n\rangle$  with the coefficients  $c_n = \tanh^n \xi / \cosh \xi$ . The population of such a state is depicted by the diagonal elements of its density matrix in Fig. 2.5b.

Measuring the  $J_z$  component of the perfect two-mode squeezed state will collapse the state such that the number difference  $N_A - N_B = 0$  and therefore  $\Delta J_z$  is minimal. The phase on the other hand is completely undefined. This state can then be depicted as a ring around the equator of the Bloch sphere (Fig. 2.5c) and is an example for a heralded Dicke state.

In quantum optics two-mode squeezed states generated by parametric down conversion have been used to show the first EPR correlated states [20]. A similar approach has been taken in several atom optics experiments [13–15, 67]. The generation of such an atomic two-mode squeezed state is described in the following chapter.

## 2.3 Experimental realization

### 2.3.1 Preparing the atomic ensemble

The following briefly describes the experimental setup and the procedure to obtain a Bose-Einstein condensate. A more thorough description of the setup and the experimental sequence can be found elsewhere [68].

All experiments are conducted with  $^{87}\text{Rb}$ . The experimental sequence begins with the loading of a three-dimensional magneto-optical trap (MOT) from the background gas. During the loading, the  $^{87}\text{Rb}$  pressure in the MOT cell is

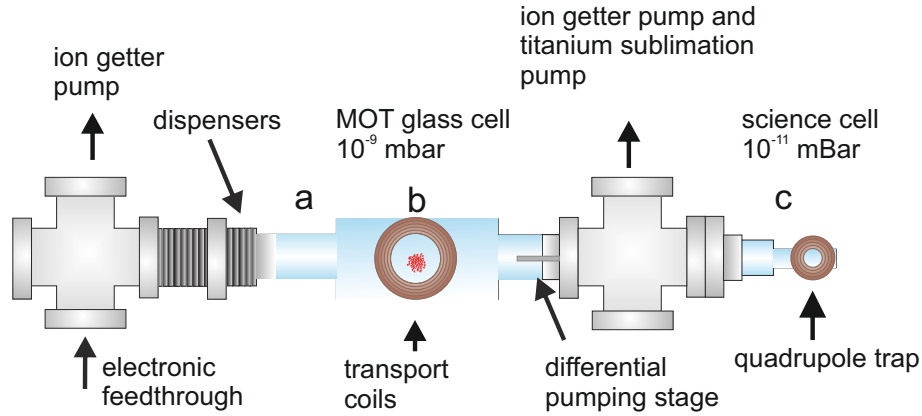


**Figure 2.6: Sketch of the vacuum system viewed from the top.** **a** The MOT is loaded from the background gas provided by the dispensers that are situated inside the bellow on the left side of the MOT cell. **b** After molasses cooling and state preparation the atomic ensemble is transferred to a magnetic trap supplied by the transport coils. This set of coils is used to transfer the ensemble from the MOT cell through the differential pumping stage into the science cell. **c** The science cell provides better vacuum conditions in the order of  $10^{-11}$  mBar. The atoms are transferred into a hybrid trap, consisting of a magnetic quadrupole trap and a crossed beam dipole trap, and a radio-frequency evaporation is applied. Finally the pre-cooled ensemble is transferred fully to the dipole trap in which it is further cooled to quantum degeneracy. All further experiments take place in this crossed-beam dipole trap. The vacuum system is equipped with two ion getter pumps and a titanium sublimation pump.

temporarily increased by light induced desorption [69] that is realized by illuminating the cell with UV-light. After the MOT loading phase of 10 s the UV-light is switched off and the pressure quickly drops. The  $^{87}\text{Rb}$  is supplied by dispensers that are mounted inside a bellow to the left of the MOT cell (see Fig. 2.6). The dispensers are regularly heated up by applying a current of 4.5 A for 50 min. During this time  $^{87}\text{Rb}$  is dispensed and deposited on the surfaces of the MOT cell.

After the MOT is fully loaded, the magnetic field is switched off and the lasers are detuned to allow for a short molasses cooling phase. This ends by optically pumping the atoms into the  $|F, m_F\rangle = |2, 2\rangle$  hyperfine ground state which is magnetically trappable. The atoms are transferred into a quadrupole trap that is supplied by two coils in anti-Helmholtz configuration that are mounted on a horizontal translation stage. Within 1.3 s the atoms are transported into the science cell. They pass through a differential pumping stage that allows for better vacuum conditions of  $10^{-11}$  mbar while the vacuum in the MOT cell goes up to  $10^{-9}$  mBar during MOT loading. An ultra-high vacuum in the science cell

is crucial for the following experiments since every collision of the ensemble with background gas leads to losses and dephasing of the prepared state.

Through an adiabatic ramping process the atoms are transferred from the transport coils to the magnetic potential of a quadrupole trap before a crossed beam dipole trap is ramped up to form a hybrid trap [70]. Radio-frequency evaporation [71] pre-cools the atoms before the magnetic field is slowly ramped down such that the atoms remain in the dipole trap. The dipole trap consists of two horizontal laser beams at a wavelength of 1064 nm with beam waists of 51.4  $\mu\text{m}$  and 26.8  $\mu\text{m}$  and maximal output powers of 3 W and 750 mW, respectively.

After the magnetic trap is fully switched off and the atoms are trapped only in the dipole potential, the evaporative cooling commences. The beam power is slowly reduced to 35 mW and 14 mW, which brings the atomic ensemble to quantum degeneracy. For the subsequent experiments a stronger confinement is needed and so the beam powers are adiabatically increased again to 250 mW and 30 mW.

After 130 ms of evaporation in the dipole trap the atoms are transferred from the  $|2, 2\rangle$  state first to  $|1, 1\rangle$ . A resonant light pulse extracts atoms remaining in the  $F = 2$  manifold before the atoms are transferred to the final state  $|1, 0\rangle$  via  $|2, 0\rangle$  using microwave transitions. The states  $|1, \pm 1\rangle$  are cleaned of remaining atoms by a microwave coupling to  $|2, \pm 2\rangle$  before a second resonant light pulse on the  $F = 2$  manifold completes the state preparation. The evaporation continues for another 320 ms, resulting in a BEC in  $|1, 0\rangle$  containing roughly 10,000 atoms and only a low thermal background.

After experiments have been performed in the science cell, the atoms are detected with a state dependent detection. The whole experimental cycle amounts to 23 s.

### State dependent detection

During the time of free fall before the detection, a strong magnetic gradient is applied. The atoms are thus exposed to a state dependent force, where high-field seeking and low-field seeking states are moved in opposite directions due to the linear Zeeman effect. The magnetically insensitive states experience only a weaker force that is due to the quadratic Zeeman effect. The splitting is applied in the vertical direction.

A resonant light beam illuminates the ensembles. The atoms scatter light and thus reduce the intensity in the beam, leaving a shadow on the CCD camera that is used for detection. This picture is compared with a picture of the unperturbed beam. The comparison is then used to estimate the number of atoms in each

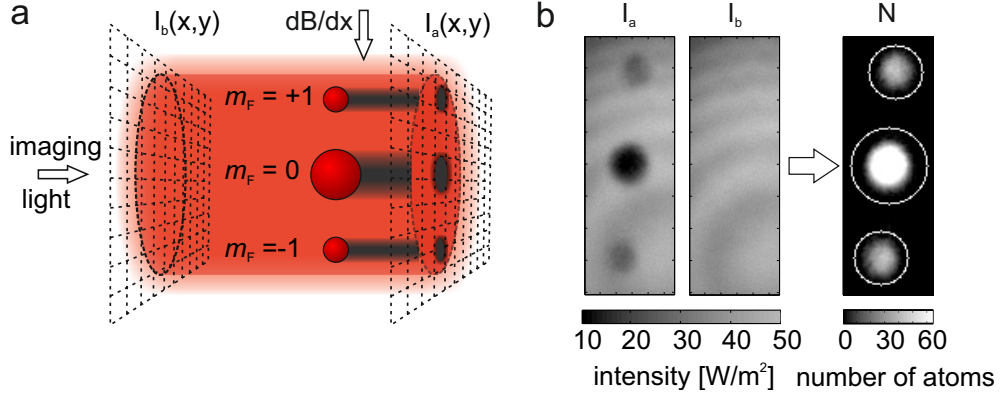


**Figure 2.7: Absorption imaging.** **a** Schematic illustration of the absorption imaging. The intensity of the incoming light  $I_b(x, y)$  is recorded on a CCD camera, yielding intensity measurements  $I_b^{(i)}$  on each pixel  $i$ . A strong magnetic field gradient separates the atoms into the different Zeeman components. The atoms scatter light and thus reduce the intensity in the beam, leaving a shadow on the CCD image  $I_a(x, y)$ . **b** The intensity measurement of the beam in the presence of the atomic ensembles  $I_a$  is compared to the unperturbed beam intensity  $I_b$ . The number of atoms  $N$  per pixel is calculated.

state. The number of atoms  $N^{(i)}$  per pixel  $i$  is calculated via

$$N^{(i)} = \frac{A_{px}}{\sigma_0} \left( \alpha \ln \left( \frac{I_b^{(i)}}{I_a^{(i)}} \right) + \beta \frac{I_b^{(i)} - I_a^{(i)}}{I_s} \right), \quad (2.26)$$

where  $A_{px}$  is the area of the single pixel,  $\omega_0$  is the resonant scattering cross section, and  $\alpha$  and  $\beta$  are corrections that have to be introduced to accommodate for deviations from the ideal situation.

To accurately estimate the number of atoms, first the intensity calibration of the camera has to be determined experimentally. Assuming a linear error in the gain of the camera, this gives the correction factor  $\beta$  for the intensity. Secondly, the saturation intensity has to be determined experimentally, since it can differ from the ideal case for resonant,  $\sigma^+$ -polarized light.  $\alpha \propto 1 + 4(\delta/\Gamma)^2$ , where  $\Gamma$  is the line width of the transition, also accounts for a detuning  $\delta$  that is unavoidable during the detection due to the acceleration the atoms experience from the imaging beam. Experimentally, the effective saturation intensity  $\alpha I_s$  is determined by preparing two atomic ensembles with the same atom number. That can either be achieved via spin dynamics or via a well tuned radio-frequency transition from  $m_F = 0$  to  $m_F = \pm 1$ . Assuming the intensity calibration of the camera is correct, one can now find  $\alpha$  by minimizing the fluctuations  $\Delta(N_{+1} - N_{-1})$  of the atom number difference of the two states [72]. In our system  $\alpha = 1.598$ .

A third effect that has to be taken into account is a deviation from the linear

scaling of the atom number estimation due to the non-linear part of Eq. (2.26). This can lead to an underestimation of the number of atoms, and therefore to an underestimation of the fluctuations of the number of atoms. Multiple effects contribute to this deviation. A strong intensity variation over the area of a single pixel can lead to non-linearity. Therefore, the pixel size should be small compared to the size of the atomic cloud. The other effects are related to the imaging time. During the illumination of the cloud, the atoms diffuse due to the recoil of scattered photons. Also, the cloud is pushed in the imaging direction and thus out of the focus of the detection. Thus, the detection time has to be chosen long enough to allow for sufficient scattering, but short enough to avoid these effects. This can be experimentally verified, by measuring two systems with a fixed total atom number. One of the systems is distributed on two clouds, while the other is in a single cloud, with a therefore higher density. If these two measurements show no deviation in the total atom number, a non-linearity of the detection can be excluded. If that is not the case, one can introduce a corrected particle number  $N_{true} = N + N^3/c^2$ . The rescaling factor  $c$  is determined by minimizing the fluctuations between the two atom number measurements. In our system  $c = 90,491$  which leads to an underestimation of 5% for 20,000 atoms. For a more detailed discussion of the calibration techniques see Ref. [73].

The detection requires a high precision in order to observe sub shot noise fluctuations in the counting statistics of the two  $|1, \pm 1\rangle$  states. The shot noise limit scales as  $\sqrt{N}$  so for the 10,000 atoms of the initial BEC shot noise is at 100 atoms. But not only the initial BEC needs to be detected with high precision but more importantly also the two pseudo-spin states. In the following experiments, these are typically populated by 1,000 to 2,000 atoms. Thus the limit for the detection has to be better than few tens of atoms. The implemented detection allows for an estimation of the number of atoms in a single state with the precision of 16 atoms.

### 2.3.2 Spin dynamics process

In chapter 2.2, different methods to create single-mode as well as two-mode squeezed states have been presented. The following section describes the collisional process that is employed to create a two-mode squeezed state in this experiment. The two-mode squeezed state will be created in the Zeeman  $m_F = \pm 1$  levels of the  $F = 1$  manifold.

Fig. 2.8a shows the effective potential two atoms experience during an interaction. The hyperfine states of two atoms with large interatomic distance is described by the respective spins  $\vec{F}_{in,1}$  and  $\vec{F}_{in,2}$ . If the atoms get closer, their hyperfine states form a collective state  $\vec{G} = \vec{F}_{in,1} + \vec{F}_{in,2}$ . When the atoms leave the interaction region they are again described by the individual states  $\vec{F}_{out,1}$  and

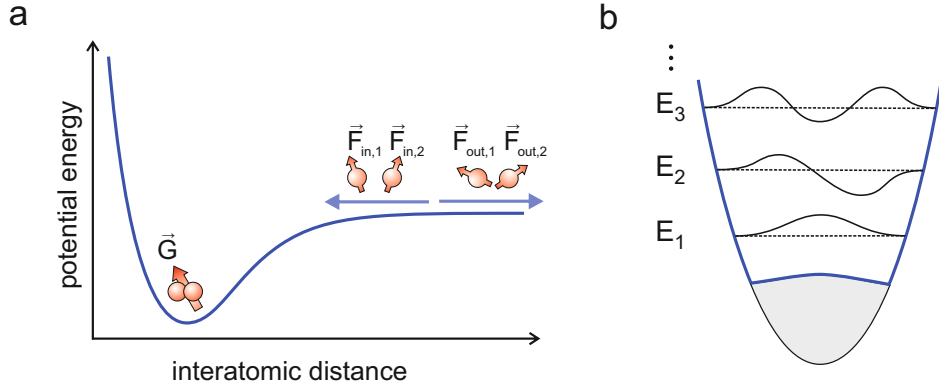


**Figure 2.8: Collisional interaction and the effective trapping potential.** **a** In the limit of larger inter atomic distance the hyperfine state of two particles is described by  $\vec{F}_{in,1}$  and  $\vec{F}_{in,2}$  respectively. If the two atoms get closer, their hyperfine states couple to form a collective state  $\vec{G} = \vec{F}_{in,1} + \vec{F}_{in,2}$ . After the collision the atoms are again described by single hyperfine states  $\vec{F}_{out,1}$  and  $\vec{F}_{out,2}$  that can have changed through the collision. **b** The black parabola depicts the trapping potential with eigenenergies  $E_n$  (dashed, black) and the corresponding eigenstates (solid black). The effective potential for atoms in  $m_F = \pm 1$ , depicted in blue, consists of the external potential and the repulsive mean-field interaction with the condensate in  $m_F = 0$  which is illustrated in grey.

$\vec{F}_{out,2}$ . These states can change with respect to the incoming states while  $\vec{G}$  is conserved and thus the atoms may undergo a spin-changing collision.

### Theoretical description

The condensate is initially in the  $|E, m_f\rangle = |1, 0\rangle$  state where, under certain conditions, spin-changing collisions between two atoms occur, lifting one atom into the state  $|1, 1\rangle$  while the other drops to the state  $|1, -1\rangle$ . The Hamiltonian governing this collisional interaction can be written as [74]

$$H = 2UC(a_0^\dagger a_0^\dagger a_{+1} a_{-1} + a_{+1}^\dagger a_{-1}^\dagger a_0 a_0), \quad (2.27)$$

where  $U = -3.351 \frac{\text{Hz}}{10^{14} \text{cm}^{-3}}$  describes the density dependent collision rate of two atoms undergoing a spin changing collision to  $m_F = \pm 1$  and the inverse process.  $a_{m_F}$  are the annihilation operators for the involved Zeeman-levels, whereas

$$C = \int d\vec{r} n_{m_F=0}(\vec{r}) |\phi_{\pm 1}(\vec{r})|^2 \quad (2.28)$$

is the spatial overlap of the wave functions, where  $\phi_{\pm 1}(\vec{r})$  is the wave function of the resonant mode and  $n_{m_F=0}(\vec{r})$  is the density of the initial condensate in  $m_F = 0$ .

If one assumes a large initial condensate with  $N$  atoms and only negligible depletion by the spin changing collisions, the Hamiltonian can be written in the parametric approximation with  $a_0 = \sqrt{N}$  and  $\Omega = 2CNU \in \mathbb{R}$  as

$$H \approx \Omega(a_{+1}a_{-1} + a_{+1}^\dagger a_{-1}^\dagger). \quad (2.29)$$

The structure of this Hamiltonian is equivalent to that of parametric down conversion Eq. (2.23), thus it is not surprising that the emerging state is again the two-mode squeezed state

$$|\Psi\rangle = \sum_{n=0}^{\infty} \frac{(-i \tanh \xi)^n}{\cosh \xi} |n, n\rangle \quad (2.30)$$

where  $\xi = \Omega t$ . Note, that the small difference in the coefficients compared to Eq. (2.25) is due to the different choice of phase. However, this does not affect the general properties of the states.

To fully describe the spin dynamics process, not only the spin changing interactions have to be taken into account but also the external and internal degrees of freedom. Under the assumption that atoms in  $m_F = \pm 1$  have the same spatial wave function and if one sets the zero energy point to the energy of an atoms in the groundstate of the  $m_F = 0$  condensate, the full Hamiltonian can be expressed as

$$H = (E_n + q)(a_{+1}^\dagger a_{+1} + a_{-1}^\dagger a_{-1}) + \Omega(a_{+1}a_{-1} + a_{+1}^\dagger a_{-1}^\dagger). \quad (2.31)$$

$E_n + q$  describes the potential energy of an atom in the  $n$ th excited  $m_F = \pm 1$  state of the effective trapping potential (see Fig. 2.8b), where  $2q$  is defined as the excess energy that two atoms in the  $m_F = \pm 1$  state have compared to two atoms in  $m_F = 0$  due to the quadratic Zeeman shift.

If the involved energies are expressed as a detuning  $\delta_n = E_n + q$ , the time evolution of the Hamiltonian Eq. (2.31) in the interaction picture becomes

$$H(t) = \Omega(a_{+1}a_{-1}e^{-2i\delta_n t} + a_{+1}^\dagger a_{-1}^\dagger e^{2i\delta_n t}). \quad (2.32)$$

$\xi \propto \Omega e^{2i\delta_n t}$  acts as a complex squeezing parameter which changes its angle in the complex plane with the time  $t$ . Assuming unchanging overlap of the spatial modes, this rotation has the same effect as a time reversal and an oscillation of the population in the  $m_F = \pm 1$  states arises [75]. The start of the spin changing collisions can either happen spontaneously due to quantum mechanical fluctuations in the spin orientation or it can be triggered by a seed in the  $m_F = \pm 1$  modes. The following experiments rely on the spontaneous process.

Spin changing collisions are suppressed and the  $m_F = 0$  condensate is stable if  $\delta_n \gg \Omega$  for all eigenenergies  $E_n$  of the system.



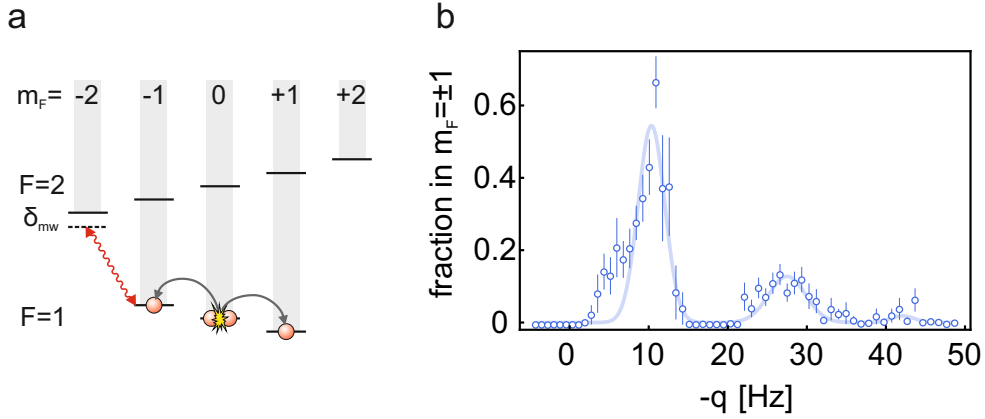


**Figure 2.9: Dressing and spin dynamics resonance scan.** **a** A detuned microwave is introduced to the transition  $|F, m_F\rangle = |1, -1\rangle \rightarrow |F, m_F\rangle = |2, -2\rangle$ . Thereby the  $|F = 1, m_F = -1\rangle$  state is shifted such that the resonance condition is fulfilled and spin changing collisions are possible. **b** Spin dynamics resonance scan. The fraction of atoms in the  $m_F \pm 1$  state is recorded for different values of the access energy  $q$ . At  $\approx -10$  Hz the energetic ground state of the trap is populated, while at  $q \approx -28$  Hz and  $q \approx -42$  Hz higher trap modes are populated. The blue line is a guide to the eye. Error bars indicate the standard deviation of 11 experimental cycles.

### Experimental realization of spin changing collisions

In the experimental sequence a homogeneous magnetic field of 2.6 G is used to define a quantization axis for the Zeeman levels  $m_F$ . Due to the influence of the quadratic Zeeman effect,  $q \approx 500$  Hz at this magnetic field. For the aforementioned dipole trap and atom numbers,  $\Omega$  is typically in the few Hz regime. This means that  $\delta_n \gg \Omega$  is fulfilled and spin changing collisions are suppressed.

One way to overcome this energy gap is to introduce a microwave dressing. By applying an off-resonant microwave to the transition  $|F, m_F\rangle = |1, -1\rangle \rightarrow |F, m_F\rangle = |2, -2\rangle$ , the energies of the two states are shifted by [76]

$$\begin{aligned} \Delta E_{|1,-1\rangle} &= \frac{\delta_{mw}}{2} \left( \sqrt{1 + \frac{\Omega_{mw}^2}{\delta_{mw}^2}} - 1 \right) \\ \Delta E_{|2,-2\rangle} &= - \frac{\delta_{mw}}{2} \left( \sqrt{1 + \frac{\Omega_{mw}^2}{\delta_{mw}^2}} - 1 \right). \end{aligned} \quad (2.33)$$

$\Omega_{mw}$  is the undetuned Rabi-frequency of the transition and  $\delta_{mw}$  is the detuning. If the dressing is now chosen such that  $\Delta E_{|1,-1\rangle}$  exactly compensates the quadratic Zeeman shift a resonance condition is reached, where two atoms in the  $m_F = 0$  condensate can undergo a spin changing collision to the energetic groundstate

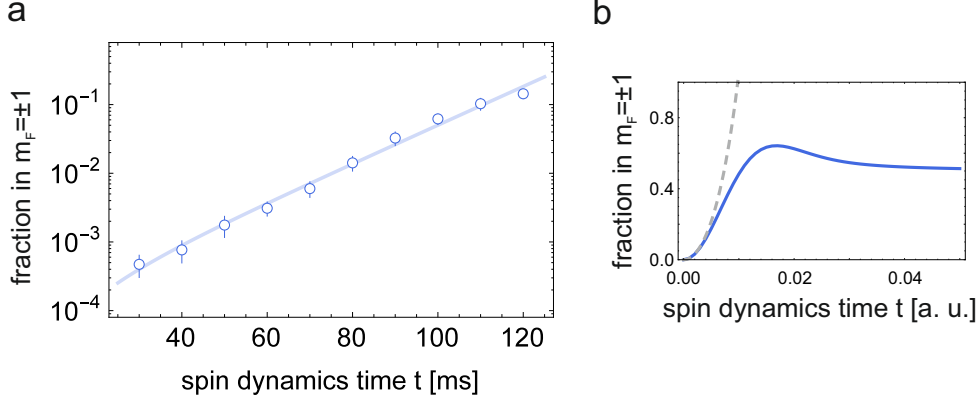


**Figure 2.10: Measurement of the spin dynamics rate  $\Omega$ .** For different spin dynamics times  $t$  the fraction of atoms in the states  $m_F \pm 1$  is evaluated. The time evolution is fitted by  $N_{+1} = N_{-1} = \sinh^2(|\Omega|t)$ , with  $|\Omega| = 2\pi \cdot 5.15$  Hz, as indicated by the blue line. Error bars indicate the standard deviation of 13 experimental cycles. **b** For short time scales the time dependence can be approximated by a hyperbolic growth (dashed grey line). Once the parametric approximation is not valid anymore, saturation sets in (solid blue line) [73, 77].

$E_0$  of the  $m_F = \pm 1$  state as indicated in Fig. 2.9a. If the energy level  $\Delta E_{|1,-1\rangle}$  is further shifted such that  $E_n + q = 0$  for  $n > 0$  higher trap modes are populated.

Fig. 2.9b shows a spin dynamics resonance scan, where the access energy  $q$  is tuned via the detuning  $\delta_{mw}$  of the microwave dressing. The population of the states  $m_F = \pm 1$  is recorded. Around  $q \approx -10$  Hz the groundstate for  $m_F = \pm 1$  is populated, while the population increase at  $q \approx -28$  Hz and  $q \approx -42$  Hz corresponds to the population of higher trap modes.

Fig. 2.10a shows a measurement of the time dependence of the transferred atoms during the spin dynamics process. For short time scales, where the parametric approximation is valid, the time dependence can be approximated by  $N_{+1} = N_{-1} = \sinh^2(\Omega t)$ , where  $N_{+1}$  and  $N_{-1}$  are the number of atoms in the  $m_F = \pm 1$  levels. Here we fit  $\Omega = 2\pi \cdot 5.15$  Hz. For longer time scales where  $N_{+1} + N_{-1} \ll N$  is no longer valid, the parametric approximation is not applicable and a saturation process due to the depletion of the  $m_F = 0$  condensate will cause a deviation from the hyperbolic scaling (see Fig. 2.10b).

A more detailed explanation of this multiresonant behavior, including the underlying instability rates that are directly linked to Bogoliubov excitations in the initial condensate, can be found in Refs. [13, 78].

---

# EINSTEIN-PODOLSKY-ROSEN CORRELATIONS

In 1935 Einstein, Podolsky and Rosen published a paper with the title "*Can quantum-mechanical description of physical reality be considered complete*" [17]. They consider two particles with correlated position and anti-correlated momenta. If a measurement of the momentum is performed on the first particle, a perfect prediction about the momentum measurement of the second particle is possible. The same holds for the position measurement. They now argue, that if one can make these predictions due to a measurement on a different, non-interacting system, a simultaneous reality of the possible measurements, i.e. position and momentum, exists and therefore, the quantum mechanical description must be incomplete. To them, the contradiction of such systems with the concept of a local reality was especially surprising. This seeming paradox became later known as the EPR paradox.

The following chapter will first give a short introduction to the historical argument of EPR. Afterwards the more generalized inferred Heisenberg inequalities will be discussed, including the first realization of EPR correlated atomic ensembles. The state will be fully characterized by a state tomography and the directionality of EPR correlations will be examined. The main results of this chapter are published in Ref. [79].

## 3.1 The original EPR proposal

In their original proposal, EPR consider a state with perfect correlations. They assume two particles interact until a time  $t_0$ . After  $t_0$  they separate with opposing momenta  $p_A$  and  $p_B$  until they are located at perfectly correlated positions  $x_A$  and

$x_B = x_A + x_0$ . A sketch of the situation is shown in Fig. 3.1. The wave function of the system for any time  $t > t_0$  can then be written as

$$\Psi(x_A, x_B) = \int_{-\infty}^{\infty} e^{i(x_A - x_B + x_0)p} dp. \quad (3.1)$$

This state is an example for an inseparable state. One can now rewrite this state as a superposition of the eigenfunctions of the momentum operators  $\hat{p}_{A/B} = (-i\partial/\partial x_{A/B})$  as

$$\Psi(x_A, x_B) = \int_{-\infty}^{\infty} e^{-i(x_B - x_0)p} e^{ix_A p} dp, \quad (3.2)$$

such that it becomes directly apparent, that a measurement of  $\hat{p}_A$  with outcome  $p_A = p$  would immediately determine the outcome of a measurement of  $\hat{p}_B$  as  $p_B = -p$ .

Now the same holds true for the position operators  $\hat{x}_{A/B} = x_{A/B}$ . The wave function can be expressed in their basis as

$$\Psi(x_A, x_B) = \int_{-\infty}^{\infty} \int_{-\infty}^{\infty} e^{i(x' - x_B + x_0)p} \delta(x_A - x') dp dx', \quad (3.3)$$

therefore a measurement of  $\hat{x}_A$  with outcome  $x_A = x$  predetermines the outcome of a subsequent measurement of  $\hat{x}_B$  to be  $x_B = x + x_0$ .

EPR now argued, that the measurement outcomes are governed by what they call a "physical reality" and the measurement on system  $A$  does not disturb system  $B$  in any way. If one now assumes EPR's understanding of reality, which is nowadays known as local realism, the measurement outcome has to have been predetermined by associated elements of reality  $\mu_B^{x/p}$ , before the two sub-systems  $A$  and  $B$  stopped interacting due to their spatial separation.

The elements of reality  $\mu_B^{x/p}$  act here as hidden variables, that are predetermined but not accessible until the measurement of  $\hat{x}_A$  or  $\hat{p}_A$  is performed. Since it is not known beforehand which measurement (position or momentum) will be performed, both  $\mu_B^x$  and  $\mu_B^p$  have to predetermine the respective measurement outcomes with absolute certainty. This is contrary to quantum mechanics since  $\hat{x}_B$  and  $\hat{p}_B$  are non-commuting variables and thus obey the Heisenberg uncertainty relation. Therefore if one assumes the infallibility of local realism, the conclusion must be that quantum mechanics is not complete.

Bohr replied to EPR's paper within two month, arguing that the concepts of a physical reality that is assigned to the systems and that of local realism, while interesting from a philosophical point of view, do not challenge quantum mechanics [80]. Schrödinger's reply involved the formulation of the idea of

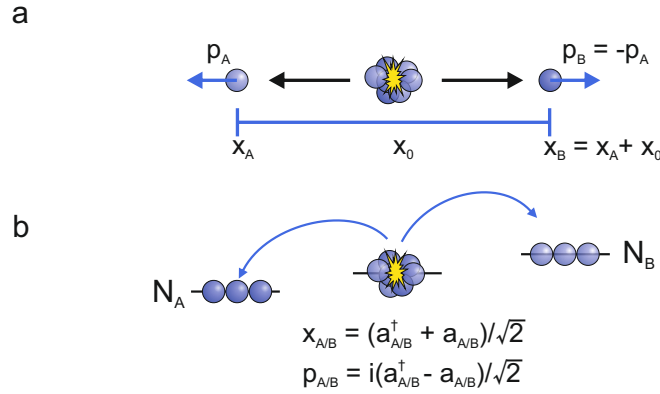


**Figure 3.1: Sketch of the original EPR proposal and the realization in the continuous variable case.** **a** EPR originally proposed a system where two particles  $A$  and  $B$  have perfectly anti-correlated momenta  $p_A$  and  $p_B$  and perfectly correlated positions  $x_A$  and  $x_B$ . **b** In the continuous variable case that is here implemented via spin dynamics correlations appear in amplitude and phase quadratures  $x_{A/B}$  and  $p_{A/B}$ . The quadratures are defined as functions of the creation and annihilation operator  $a_{A/B}^\dagger$  and  $a_{A/B}$  of the two involved Zeeman levels  $A$  and  $B$ .

entangled and separable states as well as his famous gedankenexperiment now known as Schrödinger's cat [19].

While EPR argue, that the description of the wave function is not complete, they suggest, that it might be possible to formulate a complete description. In the 1970's Bell [81] as well as Clauser et al. [82] showed that such a local hidden variable theory can not coincide with quantum mechanics. They provide inequalities, known as Bell's and CHSH inequalities, whose violation would indicate a failure of EPR's local realism.

Experimental approaches to show such a violation are called Bell tests and have been performed in various settings. The first reported violation was measured utilizing the correlations between the polarizations of photons, that were emitted by an atomic cascade of calcium [83]. An atomic Bell test was first realized with two  $\text{Be}^+$  ions in a linear Paul trap [84].

All experimental realizations up to now suffer from loopholes, either that of locality, meaning the insufficient spatial separation between the two parties, or that of limited detection efficiency. The locality loophole can only be closed, if a classical interaction between the two parties during the detection process is impossible. This is the case if  $x_0 > ct_{det}$ , where  $x_0$  is the spatial separation and  $t_{det}$  is the time needed for the detection process. These loopholes could allow for the existence of a highly artificial local hidden variable theory. For a detailed discussion of the current state of research on Bell nonlocality, please refer to

Ref. [85].

The first realization of continuous-variable entanglement, satisfying the EPR criterion was achieved in 1992 in a photonic system generated by optical parametric down-conversion [20]. Since then, EPR entanglement has been shown in different setups, including systems where position and momentum of two photonic beams are measured [21, 86]. With  $\Delta^2(x_1 - x_2)\Delta^2(p_1 + p_2) = 4.2 \cdot 10^{-4}$ , where  $1/4$  is the threshold for EPR entanglement, this experiment achieved the highest degree of entanglement yet. While several experiments have shown inseparability in accordance to  $\Delta^2(x_1 - x_2) + \Delta^2(p_1 + p_2) < 2$  [87, 88], EPR entanglement with massive particles has not been shown up to now [7, 15, 24].

EPR entanglement is not just interesting from a fundamental point of view. The strong correlations the states exhibit are also interesting for various applications. EPR correlations can be used for quantum key distribution schemes as described in Ref. [89], where the strong correlations enable secure distribution. Another application are quantum teleportation and entanglement swapping, which was first proposed with EPR correlated states [90, 91]. Using a protocol that includes EPR correlations as well as classical communication the receiver can produce an exact replica of the senders state. The loopholes that are relevant in Bell tests, would also be of interest here, since they could be exploited by a third party if these states were used for quantum cryptography.

## 3.2 Inferred Heisenberg inequalities

The setting that is described by EPR requires perfect correlations and anti-correlations between two particles, which is not realizable in practice. Therefore, the EPR argument has to be extended to include realistic experiments. This is achieved by replacing the perfect pairwise correlations by stochastic probability distributions, meaning that a measurement on subsystem  $A$  does not allow a prediction of the outcome at subsystem  $B$  with absolute certainty. The argument that is now introduced follows Reid et al. [92].

Again  $\hat{x}_{A/B}$  and  $\hat{p}_{A/B}$  are two non-commuting observables in the systems  $A$  and  $B$ . While the measurement outcome  $x_B$  does not allow for a certain prediction of the measurement result at  $A$ , it can still be used to make an estimate  $x_{est}(x_B)$  of the result  $x_A$ . This estimate will have an error, that can be expressed as the deviation of the estimator  $x_{est}(x_B)$  from the actual result  $x_A$  as

$$\Delta_{inf}^2(x|x_B) = \int dx P(x|x_B) [x - x_{est}(x_B)]^2. \quad (3.4)$$

$P(x|x_B)$  is the conditional distribution that describes the probability to obtain the measurement result  $x$  in system  $A$  if  $x_B$  was previously measured in system  $B$ . The best estimate for  $x_A$  is therefore the mean of  $P(x|x_B)$  and the error of the

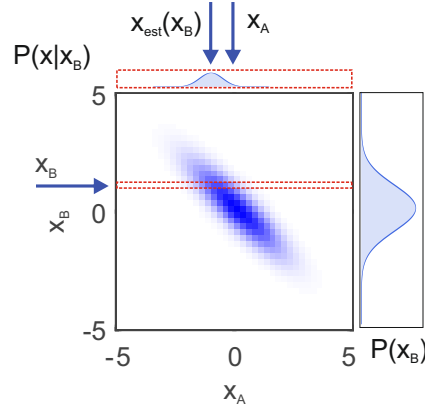


**Figure 3.2: Two dimensional probability distribution  $P(x_A|x_B)$ .** The probability of a measurement  $\hat{x}_B$  yielding the outcome  $x_B$  is  $P(x_B)$ , which is the accumulated probability over the here horizontal direction. The conditional probability to measure  $x_A$  after  $x_B$  was measured is given by  $P(x|x_B)$ , as marked in red. The best estimate  $x_{est}(x_B)$  for  $x_A$  is now the mean of this distribution and the error is defined via the distance of the actual measurement  $x_A$ .

estimate becomes the variance  $\Delta^2(x|x_B)$  of  $P(x|x_B)$ . The situation is depicted in Fig. 3.2.

Therefore, the minimal inference error  $\Delta_{inf}^2 x$  averaged over all possible measurement outcomes  $x_B$  for the measurement  $\hat{x}_B$ , with probability  $P(x_B)$  is

$$V_{A/B}^x = (\Delta_{inf}^2 x)_{min} = \int dx_B P(x_B) \Delta^2(x|x_B). \quad (3.5)$$

An analogous definition for the inferred minimal variance  $V_{A/B}^p$  for the second pair of observables  $\hat{p}_{A/B}$  can be obtained.

Now the argument of local reality has to be generalized to the case of probability distributions instead of perfect correlations. For the local reality argument to hold true, there still need to be elements of reality  $\mu_A^{x/p}$  associated with the variable. The difference is, that these elements don't predict the outcomes with absolute certainty, but the predicted values are now given by probability distributions  $P(x|\mu_A^x)$  and  $P(p|\mu_A^p)$ . The probability distribution  $P(x|\mu_A^x)$  is now represented by the conditional distribution  $P(x|x_B)$ . The variance of this probability distribution is  $\Delta^2(x|\mu_A^x)$ . Similarly, the variance  $\Delta^2(p|\mu_A^p)$  is defined.

Following the same argument as in the original EPR paper,  $\mu_A^x$  and  $\mu_A^p$  have to be defined simultaneously and therefore a joined probability distribution

$P(\mu_A^x|\mu_A^p)$  can be introduced. The inferred variance can then be expressed as

$$\begin{aligned} V_{A/B}^x &= \int d\mu_A^x P(\mu_A^x) \Delta^2(x|\mu_A^x) \\ &= \int d\mu_A^x d\mu_A^p P(\mu_A^x|\mu_A^p) \Delta^2(x|\mu_A^x), \end{aligned} \quad (3.6)$$

where  $P(\mu_A^x) = P(x_B)$  is the probability for the occurrence of the element  $\mu_A^x$ .

If one now assumes that the state that is described by a particular set of elements  $\mu_A^{x/p}$  has an equivalent quantum mechanical description, the probabilities associated with this state have to obey the typical relations in quantum mechanics. Therefore, if  $\Delta^2 x_{A/B} \Delta^2 p_{A/B} \geq 1/4$  holds, so must  $\Delta^2(x|\mu_A^x) \Delta^2(p|\mu_A^p) \geq 1/4$ . Due to Eq. (3.6) and the Cauchy-Schwarz inequality

$$V_{A/B}^x V_{A/B}^p < 1/4 \quad (3.7)$$

would therefore show a violation of local realism and thus show EPR correlations of the state [23].

Another interesting criterion, which is also a sufficient condition for EPR correlations, is  $V_{A/B}^x + V_{A/B}^p < 1$ . It utilizes the same format as the inseparability criterion [88, 93]

$$V_{A/B}^x + V_{A/B}^p < 2, \quad (3.8)$$

which is necessary and sufficient to characterize bipartite Gaussian states with respect to Eq. (2.1).

### 3.2.1 EPR variables for the two-mode squeezed state

In chapters 2.2.3 and 2.3.2 the two-mode squeezed state was discussed. To find EPR correlations for this state new observables have to be introduced. These are equivalent to the position and momentum from the original proposal as indicated in Fig. 3.1.

$$\begin{aligned} \hat{x}_{A/B} &= \frac{1}{\sqrt{2}} (\hat{a}_{A/B}^\dagger + \hat{a}_{A/B}), \\ \hat{p}_{A/B} &= \frac{i}{\sqrt{2}} (\hat{a}_{A/B}^\dagger - \hat{a}_{A/B}), \end{aligned} \quad (3.9)$$

are the orthogonal phase and amplitude quadratures of the system with  $\hat{a}_{A/B}$  being the annihilation operators for the two modes.  $\Delta^2 \hat{x}_{A/B} \Delta^2 \hat{p}_{A/B} \geq 1/4$  is the associated Heisenberg uncertainty relation.

The time evolution  $e^{iHt} \hat{\delta} e^{-iHt}$  of an operator  $\hat{\delta}$  can be inferred from its interaction operator  $H = \Omega(\hat{a}_A \hat{a}_B + \hat{a}_A^\dagger \hat{a}_B^\dagger)$  as

$$\begin{aligned} \hat{x}_{A/B}(t) &= \hat{x}_{A/B}(0) \cosh \xi + \hat{x}_{B/A}(0) \sinh \xi \\ \hat{p}_{A/B}(t) &= \hat{p}_{A/B}(0) \cosh \xi - \hat{p}_{B/A}(0) \sinh \xi, \end{aligned} \quad (3.10)$$

where  $\hat{x}_{A/B}(0)$  and  $\hat{p}_{A/B}(0)$  are the initial amplitudes at  $t = 0$ . For times  $t \rightarrow \infty$ , the squeezing parameter  $\xi$  goes to infinity and  $\hat{x}_A \rightarrow \hat{x}_B$  and  $\hat{p}_A \rightarrow -\hat{p}_B$ . This implies perfect correlations as in the original EPR paradox for infinitely large times  $t$ .



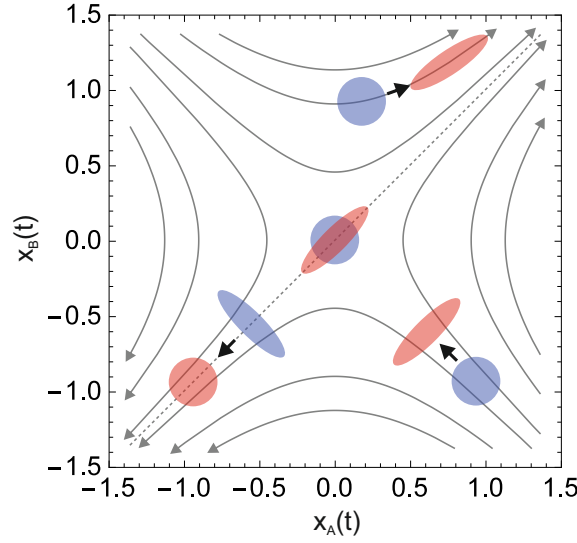


**Figure 3.3: Time evolution of the  $\hat{x}_{A/B}$  quadratures.** The gray solid lines depict the time evolution of the quadratures as given by Eqs. (3.10), with the arrows pointing in the direction of positive time. For infinitely large times, where  $\xi$  goes towards infinity, all states accumulate on the line  $x_A = x_B$  (dashed gray). The time evolution of a few states is depicted exemplarily. The initial states are marked in blue and the evolved states in red. (Depiction based on Ref. [94])

The time evolution of  $\hat{x}_{A/B}(t)$  is depicted in Fig. 3.3 for different initial values of  $\hat{x}_{A/B}(0)$  in solid gray. The time evolution of any given state (blue) can be estimated along those lines, while the dashed gray line corresponds to the extremum of  $\xi \rightarrow \infty$ . For the case of  $\hat{p}_{A/B}(t)$  the graph would be mirrored along the horizontal axis.

Starting with the pure vacuum state  $|0, 0\rangle$ , the variance of an operator  $\hat{\delta}$  can be determined via

$$\begin{aligned} \Delta^2 \hat{\delta} &= \langle 0, 0 | e^{iHt} \hat{\delta}^2 e^{-iHt} | 0, 0 \rangle \\ &= \langle 0, 0 | (e^{iHt} \hat{\delta} e^{-iHt})^2 | 0, 0 \rangle. \end{aligned} \quad (3.11)$$

The variances of the sum and difference of the quadratures are therefore squeezed and anti-squeezed with

$$\begin{aligned} V_x^\pm &= \Delta^2(\hat{x}_A \pm \hat{x}_B) = e^{\pm 2\xi} \\ V_p^\pm &= \Delta^2(\hat{p}_A \pm \hat{p}_B) = e^{\mp 2\xi}. \end{aligned} \quad (3.12)$$

This implies EPR correlations according to  $V_x^+ V_p^- < 1/4$  for all states where  $\xi > 1/2 \ln(2) \approx 0.35$ . Now the question arises how these variables can be accessed experimentally.

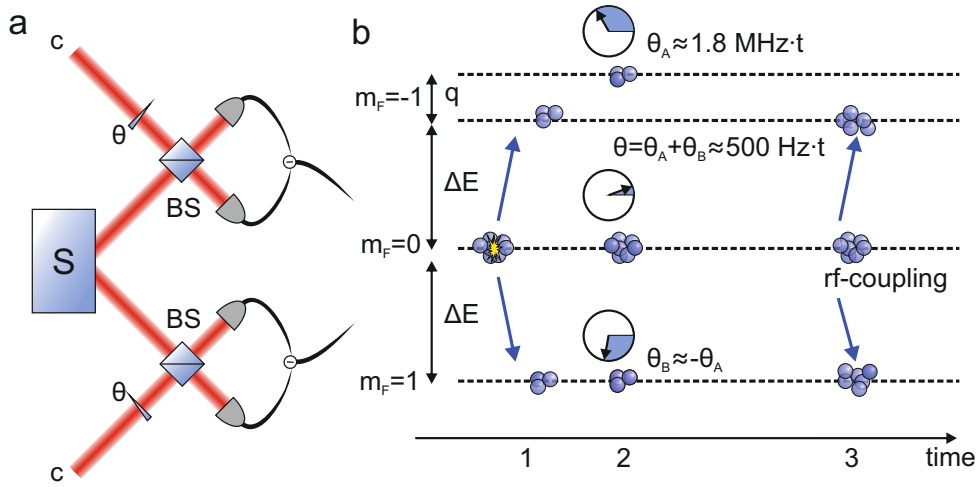


**Figure 3.4: Optical and atomic two-mode homodyne detection.** **a** Optical homodyne detection. A two-mode squeezed state is generated by a process  $S$  for example a non-linear medium. The two modes are sent to two independent detection zones, where the squeezed state is mixed on a beam splitter (BS) with a strong coherent state (c) that acts as a reference oscillator. The coherent state has a variable phase  $\theta$  imprinted by a phase shifter. The two output ports of the beam splitter are measured by photo diodes and the signals are subtracted. **b** Atomic homodyne detection. The state is produced via a spin dynamics process at time 1. The remaining condensate in the  $m_F = 0$  state acts as the local oscillator and has a phase imprinted upon it by an energy shift of the  $m_F = -1$  state relative to the  $m_F = 1$  state. This phase accumulates during time 2 with 500 Hz. At time 3 a radio-frequency pulse couples the  $m_F = 0$  condensate to the  $m_F = \pm 1$  states. This coupling acts as a three port beam splitter. At the end a state dependent detection is applied.

### 3.2.2 Atomic homodyning

In quantum optics, homodyne detection is a widely spread tool to analyze non-classical states of light. The state of interest is mixed on a beam splitter with a strong coherent light field. This light field has a variable phase that is tuned to access either the amplitude or the phase quadrature of the squeezed state. For a two-mode squeezed state, this setup has to be doubled to analyze both modes as indicated in Fig. 3.4a.

To perform atomic homodyning, the strong coherent light field is replaced by a strong coherent atomic state like the BEC in  $m_F = 0$ . The two beam splitters from the optical case are replaced by a radio-frequency coupling that simultaneously couples the  $m_F = 0$  condensate to the  $m_F = \pm 1$  states. The variable phase of the local oscillator could be imprinted onto the BEC in the  $m_F = 0$  state by a resonant

microwave  $\pi$ -pulse to  $|2, 0\rangle$ , a variable waiting time to tune the phase, and a second  $\pi$ -pulse.

In our case, the phase is imprinted by a different scheme. The phase evolution of the atomic ensembles in  $m_F = \pm 1$  compared to that in  $m_F = 0$  can be utilized to imprint an effective phase onto the  $m_F = 0$  condensate. The relative phase between  $m_F = \pm 1$  is completely randomized due to magnetic field noise and does not play a role in the atomic homodyning. If the energy difference of  $m_F = \pm 1$  to  $m_F = 0$  is equal, the phase accumulation happens at the same rate with different signs for  $m_F = \pm 1$ , leading to a vanishing effective phase for  $m_F = 0$ . By introducing an energy shift  $q$  in the  $m_F = -1$  state compared to the  $m_F = +1$  state an effective phase is accumulated in  $m_F = 0$  (see Fig 3.4b). As explained in chapter 2.3.2 this energy shift is naturally set by the quadratic Zeeman shift. It is compensated during the preparation of the state and the radio-frequency coupling via a microwave dressing. For a homogeneous field of 2.6 G the phase accumulates with 500 Hz.

After the radio-frequency pulse for homodyning, the atoms in the three modes are detected via the state dependent detection described in chapter 2.3.1. The number of atoms in each of the three modes is calculated and can be used to access the quadratures.

To this end, the homodyning pulse must be analyzed in more detail. The radio-frequency coupling can be described by a three mode unitary operation  $e^{-iH\tau/\hbar}$  with the coupling Hamiltonian

$$H = \frac{\hbar\Omega_{+1}}{2\sqrt{2}} (\hat{a}_A^\dagger \hat{a}_0 + \hat{a}_A \hat{a}_0^\dagger) + \frac{\hbar\Omega_{-1}}{2\sqrt{2}} (\hat{a}_B^\dagger \hat{a}_0 + \hat{a}_B \hat{a}_0^\dagger), \quad (3.13)$$

and the Rabi frequencies  $\Omega_{\pm 1}$  for the transition  $m_F = 0 \rightarrow m_F = \pm 1$ .  $\Omega_{\pm 1}$  are not necessarily equal. To calculate how this operator acts on the three modes, the commutators

$$\begin{aligned} [H, \hat{a}_A] &= -\frac{\hbar\Omega_{+1}}{2\sqrt{2}} \hat{a}_0, \\ [H, \hat{a}_B] &= -\frac{\hbar\Omega_{-1}}{2\sqrt{2}} \hat{a}_0, \\ [H, \hat{a}_0] &= -\frac{\hbar}{2\sqrt{2}} (\Omega_{+1}\hat{a}_A + \Omega_{-1}\hat{a}_B) \end{aligned} \quad (3.14)$$

need to be considered. With  $\Omega = \sqrt{(\Omega_{+1}^2 + \Omega_{-1}^2)}/2$ , the rescaled Rabi frequencies  $\tilde{\Omega}_{\pm 1} = \Omega_{\pm 1}/\Omega$  can be defined. The transformation of the three modes can then be expressed as

$$\begin{pmatrix} \hat{a}_A \\ \hat{a}_B \\ \hat{a}_0 \end{pmatrix}_{out} = \begin{pmatrix} \frac{\tilde{\Omega}_{+1}^2 C + \tilde{\Omega}_{-1}^2}{2} & \frac{\tilde{\Omega}_{+1}\tilde{\Omega}_{-1}(C-1)}{2} & \frac{\tilde{\Omega}_{+1}S}{i\sqrt{2}} \\ \frac{\tilde{\Omega}_{+1}\tilde{\Omega}_{-1}(C-1)}{2} & \frac{\tilde{\Omega}_{-1}^2 C + \tilde{\Omega}_{+1}^2}{2} & \frac{\tilde{\Omega}_{-1}S}{i\sqrt{2}} \\ \frac{\tilde{\Omega}_{+1}S}{i\sqrt{2}} & \frac{\tilde{\Omega}_{-1}S}{i\sqrt{2}} & C \end{pmatrix} \begin{pmatrix} \hat{a}_A \\ \hat{a}_B \\ \hat{a}_0 \end{pmatrix}_{in}, \quad (3.15)$$

with  $C = \cos(\Omega\tau/2)$  and  $S = \sin(\Omega\tau/2)$ .

Since the parametric approximation is only valid to a limited degree, it is feasible to introduce the number conserving quadratures

$$\begin{aligned}\hat{x}_{A/B} &= \frac{\hat{a}_0^\dagger \hat{a}_{A/B} + \hat{a}_{A/B}^\dagger \hat{a}_0}{\sqrt{2n_0}} = \sqrt{\frac{n_0}{2}} J_x, \\ \hat{p}_{A/B} &= \frac{\hat{a}_0^\dagger \hat{a}_{A/B} - \hat{a}_{A/B}^\dagger \hat{a}_0}{i\sqrt{2n_0}} = \sqrt{\frac{n_0}{2}} J_y,\end{aligned}\quad (3.16)$$

with  $n_i = \langle \hat{a}_i^\dagger \hat{a}_i \rangle_{in}$  being the average number of atoms in the mode  $i$  before the homodyne radio-frequency pulse. The number of atoms in the three modes after homodyning is described by  $N_i = \langle \hat{a}_i^\dagger \hat{a}_i \rangle_{out}$ , which is directly accessible in the experiment. For the presented experiments, the initial population  $n_{A/B}$  of the modes  $A$  and  $B$  before homodyning is small compared to the pump mode with  $(n_A + n_B)/n_0 \approx 10^{-4}$ . Thus, the total number of atoms in the system can be approximated as

$$N_{tot} = \langle N_A + N_B + N_0 \rangle = n_A + n_B + n_0 \approx n_0. \quad (3.17)$$

The quadrature difference  $x_A - x_B$  can be obtained by the difference of the number of atoms in the two output modes. This difference can now be expressed according to Eq. (3.15) as

$$\begin{aligned}\frac{N_A - N_B}{\sqrt{s^2 N_{tot}}} &\approx \frac{s\sqrt{N_{tot}}(\tilde{\Omega}_{+1}^2 - \tilde{\Omega}_{-1}^2)}{2} + \frac{\tilde{\Omega}_{+1}[c(\tilde{\Omega}_{+1}^2 - \tilde{\Omega}_{-1}^2) + 2\tilde{\Omega}_{-1}^2]}{2} \hat{x}_A \\ &\quad + \frac{\tilde{\Omega}_{-1}[c(\tilde{\Omega}_{+1}^2 - \tilde{\Omega}_{-1}^2) - 2\tilde{\Omega}_{-1}^2]}{2} \hat{x}_B,\end{aligned}\quad (3.18)$$

to the leading order of  $n_0$  and by setting  $a_0^\dagger a_0 \approx n_0 \approx N_{tot}$  such that fluctuations in the number of particles in  $m_F = 0$  are neglected. In the experiment  $\Omega_{+1} \approx \Omega_{-1}$  to an accuracy of 1.7% and  $c(\tilde{\Omega}_{+1}^2 - \tilde{\Omega}_{-1}^2) \ll 2\tilde{\Omega}_{\pm 1}^2$ . The quadrature difference can therefore be simplified to

$$\hat{x}_A - \hat{x}_B = \frac{N_A - N_B - s^2(\tilde{\Omega}_{+1}^2 - \tilde{\Omega}_{-1}^2)N_{tot}/2}{\sqrt{s^2 N_{tot}}}. \quad (3.19)$$

Similarly the quadrature sum can be obtained from the sum of the number of atoms in the two output modes. Again regarding the leading order in  $n_0$ , the sum is expressed as

$$\frac{N_A + N_B}{\sqrt{s^2 c^2 N_{tot}}} \approx \frac{s\sqrt{N_{tot}}}{c} + \tilde{\Omega}_{+1} \hat{x}_A + \tilde{\Omega}_{-1} \hat{x}_B. \quad (3.20)$$

Taking into account that  $\tilde{\Omega}_{+1} \approx \tilde{\Omega}_{-1} \approx 1$  the quadrature sum simplifies to

$$\hat{x}_A + \hat{x}_B = \frac{N_A + N_B - s^2 N_{tot}}{\sqrt{s^2 c^2 N_{tot}}}. \quad (3.21)$$

In the experiment, the mean transfer from  $m_F = 0$  to  $m_F = \pm 1$  and the mean difference in transfer can be used to calculate

$$\begin{aligned} \langle \frac{N_A + N_B}{N_{tot}} \rangle &\approx s^2 = 1 - c^2, \\ \text{and} & \\ \langle \frac{N_A - N_B}{N_{tot}} \rangle &\approx \frac{1}{2} s^2 (\tilde{\Omega}_{+1} - \tilde{\Omega}_{-1}). \end{aligned} \quad (3.22)$$

If one now takes the phase imprinted on the  $m_F = 0$  condensate into account,  $\hat{x}_{A/B}$  and  $\hat{p}_{A/B}$  can be expressed by one common operator as

$$\begin{aligned} \hat{X}_{A/B}(\theta) &= \hat{x}_{A/B} \cos(\theta - \pi/4) + \hat{p}_{A/B} \sin(\theta - \pi/4) \\ &= \frac{\hat{a}_{A/B}^\dagger \hat{a}_0 e^{i(\theta - \pi/4)} - \hat{a}_0^\dagger e^{-i(\theta - \pi/4)} \hat{a}_{A/B}}{\sqrt{2n_0}}. \end{aligned} \quad (3.23)$$

This means that the phase shift  $\theta$  can be used to change the observation from the amplitude to the phase quadrature as well as to intermediate angles of observation.

### 3.2.3 Analysis of the experimental data

The first step of the experiment is the preparation of 20,000 atoms in a BEC in the  $m_F = 0$  state. To ensure that no other levels are populated at this point a cleaning procedure is implemented that transfers any residual atom in  $|F = 1, m_F = \pm 1\rangle$  via microwave transitions to the  $F = 2$  manifold from which they are removed by a resonant light pulse.

27 ms of spin dynamics on the first resonance are used to prepare the initial state. During this time, a microwave dressing is adiabatically ramped on and applied to the transition  $|1, -1\rangle \rightarrow |2, -2\rangle$  such that the energy level of  $|1, -1\rangle$  is shifted and the resonance condition is reached. Afterwards, the dressing is ramped down to allow for a variable evolution time, ranging from 25  $\mu$ s to 1150  $\mu$ s, which sets the relative phase  $\theta$  between the  $m_F = 0$  condensate and the  $m_F = \pm 1$  modes by utilizing the natural quadratic Zeeman shift of  $\sim 500$  Hz at 2.6 G. For the atomic homodyning, a resonant radio-frequency pulse at 1.834 MHz is applied for 30  $\mu$ s to the transition  $|1, 0\rangle \rightarrow |1, \pm 1\rangle$ .

In Fig. 3.5a, the variances  $V_{\hat{X}(\theta)}^\pm = \Delta^2(\hat{X}_A(\theta) \pm \hat{X}_B(\theta))$ , that are defined according to Eq. (3.23), are plotted against the local oscillator phase  $\theta$ . For  $\theta = 0$  none of the variances are squeezed. The variance of the quadrature difference reaches its minimum at  $\theta = 0.75\pi$  and the variance of the quadrature sum is minimized at  $\theta = 1.25\pi$ .

From these variances, the EPR correlations can be quantified by Reid's criterion as shown in Fig. 3.5b. At the minimum,  $V_x^+ V_p^- = 0.18(3)$  which is 2.4 standard deviations below the classical limit of  $1/4$ . The data also fulfills the inseparability criterion with  $V_x^+ + V_p^- = 0.85(8)$ , as shown in 3.5c, which is 15 standard deviations below the classical limit of 2.

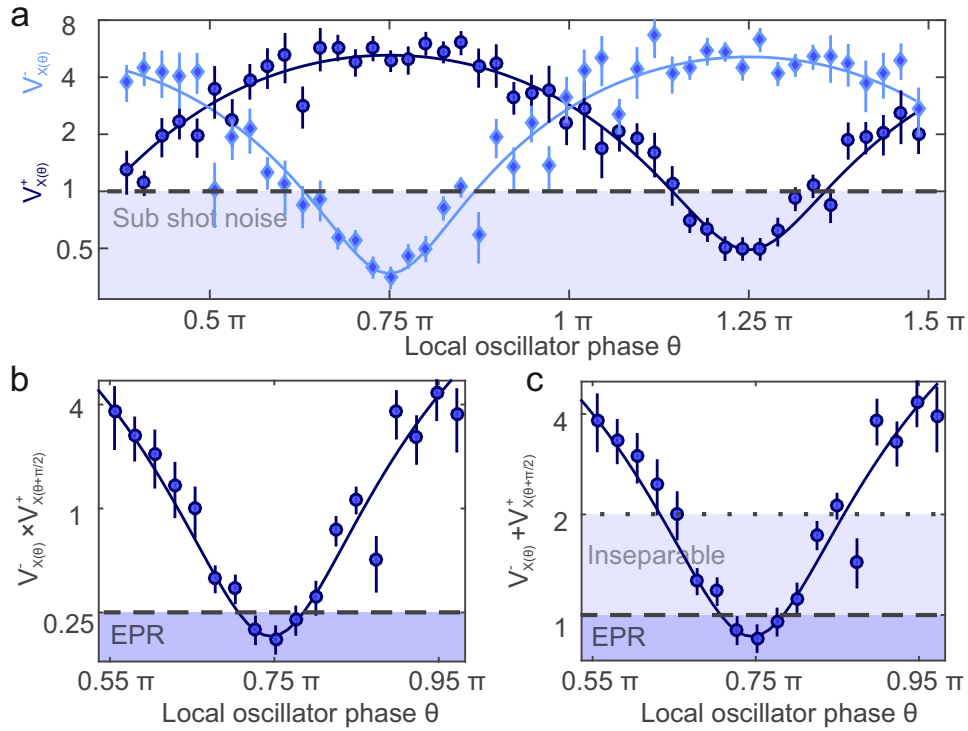


**Figure 3.5: Variance of quadrature sum and difference for multiple phases  $\theta$  of the local oscillator and EPR criteria.** **a** Variance of the quadrature sum  $V_{X(\theta)}^+$  and difference  $V_{X(\theta)}^-$  measured for different phases  $\theta$  of the local oscillator. The dashed line indicates shot noise. **b** Product EPR parameter  $V_{X(\theta+\pi/2)}^+ V_{X(\theta)}^-$  as a function of the local oscillator phase  $\theta$ . Values under the dashed line indicate a violation of the Heisenberg uncertainty and thus EPR correlations of the initial state. **c** Sum of the quadrature variance as a function of  $\theta$ . Values under the dotted line indicate inseparability, while the dashed line indicates another sufficient criterion for EPR correlations.

The produced initial state is robust against environmental influences as can be seen in Fig. 3.6. After an evolution time of 10 ms of the phase  $\theta$ , which corresponds to  $\theta > 21\pi$ , the sum of the quadrature variances still indicates inseparability.

The EPR correlations were also investigated for different spin dynamics times  $t$  as shown in Figs. 3.7a/b. The local oscillator phase is fixed to  $\theta \approx 0.75\pi$  and  $\theta \approx 1.25\pi$  to only record the  $\hat{x}$  and  $\hat{p}$  quadratures. For increasing evolution times, the variances  $V_x^-$  and  $V_p^+$  quickly drop below the classical threshold of 1, while the anti-squeezed variances  $V_x^+$  and  $V_p^-$  exhibit an exponential increase. The dashed lines correspond to the ideal squeezing and anti-squeezing behavior

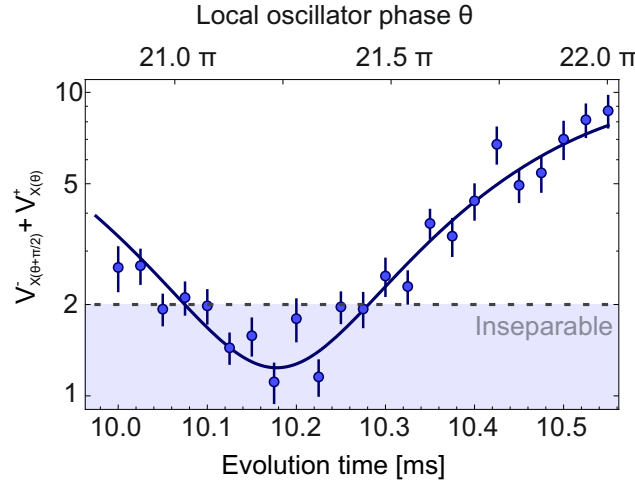


**Figure 3.6: Inseparability criterion after a long evolution time.** The inseparability of the state is still detected after an evolution time of 10 ms. The minimum corresponds to a phase of  $\theta = 21.25 \pi$ .

according to

$$\begin{aligned} V_{X(\theta)}^+ &= \cos^2(\theta - \pi/4)e^{-2\xi} + \sin^2(\theta - \pi/4)e^{2\xi}, \\ V_{X(\theta)}^- &= \sin^2(\theta - \pi/4)e^{-2\xi} + \cos^2(\theta - \pi/4)e^{2\xi}, \end{aligned} \quad (3.24)$$

with the squeezing parameter  $\xi = \Omega t$ . The spin dynamics rate  $\Omega$  was measured independently to be  $\Omega = 2\pi 5.1$  Hz. The increase in the squeezed variances after a spin dynamics time of  $\sim 25$  ms is explained by a simple noise model with radio-frequency intensity noise of 0.4 % and phase noise of the local oscillator of  $0.044 \pi$ . While the phase noise influences  $V_x^-$  and  $V_p^+$  equally, the radio-frequency intensity noise induces correlated fluctuations of the Rabi frequencies  $\Omega_{\pm 1}$  and therefore mainly influences the measurement of the quadrature sum. The phase noise is simulated by the convolution of a Gaussian distribution, with the width corresponding to the phase noise, with the ideal variance Eq. (3.24), while the radio frequency noise leads to a simple increase of 0.122 in the variance  $V_{X(\theta)}^+$ .

The measured data can be used to evaluate the EPR correlations as shown in Fig. 3.7c. The data quickly drops below the EPR threshold of  $1/4$  and reaches a minimum at  $\sim 27$  ms of spin dynamics time. The increase afterwards is well described by the product of the noise models from Figs. 3.7a/b.

### 3.3 Full state tomography

Full reconstruction of an atomic state allows for a complete characterization of said state. Up to now, atomic tomography of an atomic state was either

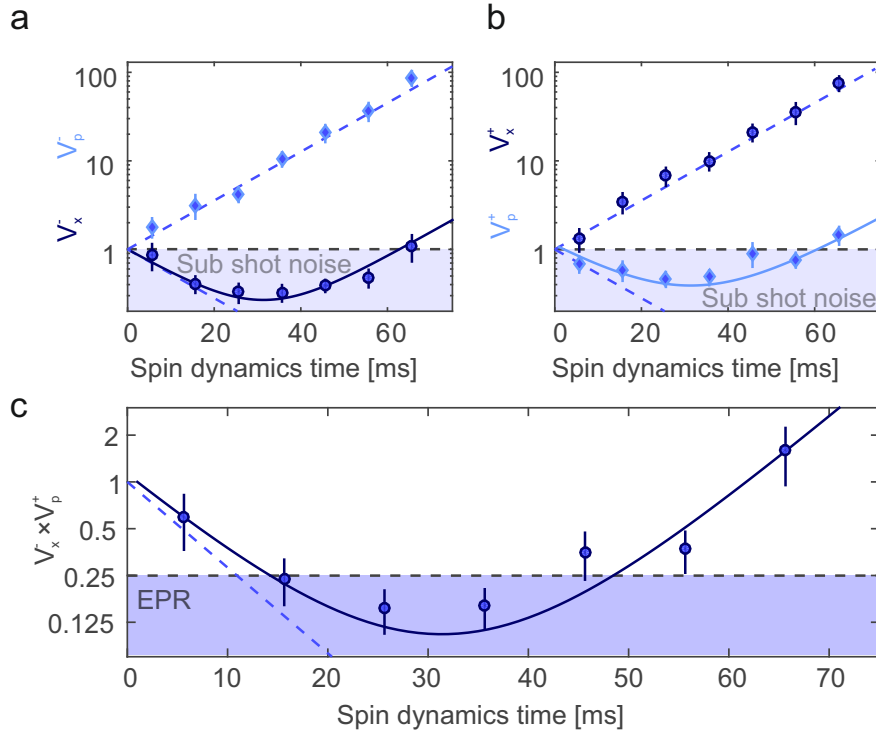


**Figure 3.7: EPR correlation as a function of spin dynamics time.** a/b The variance of the four two-mode quadratures as a function of the spin dynamics time. The data follows the ideal squeezing/anti-squeezing behavior as indicated by the dashed lines. c The EPR parameter as a function of the spin dynamics time. The behavior of the squeezed quadratures and therefore the EPR parameter is reproduced by a simple noise model as indicated by the solid lines.

demonstrated by the reconstruction of the Husimi Q-distribution [47, 59] or the Wigner function [95]. Both of these methods are restricted to the fully symmetric subspace and thus do not allow for a full reconstruction.

In quantum optics, methods were developed [96] to achieve a full state reconstruction. Reconstructions of an optical two-mode squeezed state by homodyne tomography have been performed, but assume either Gaussian states or average over all phase relations, such that the coherence properties can not be investigated [97, 98].

However, by employing a Maximum Likelihood reconstruction it is possible to obtain an unbiased, positive semidefinite density matrix of the state, that is free of any a-priori hypothesis [96, 99]. To this end, the total of 2864 homodyne measurements from the data set in Fig. 3.5 can be exploited. They cover all tomography angles  $\theta$  with increased statistics at the minima of the quadrature



variances, therefore serving as a complete set of tomography variables.

### 3.3.1 Maximum Likelihood analysis and state reconstruction

The subsequent description of the Maximum Likelihood analysis follows that of Lvovsky and Raymer [96]. The Maximum Likelihood algorithm is aimed at finding the density matrix that has the highest probability of yielding the experimental data given, while being physically plausible.

#### The classical case

Let  $\vec{r}$  be a set of parameters that characterizes the system under investigation with  $r_i > 0$  and  $\sum_i r_i = 1$ . This set of parameters should now be reconstructed from a set of measurements on the system. The probability  $p_{\vec{r}}(j)$  to obtain a certain outcome, indexed by  $j$ , is related linearly to  $\vec{r}$  by

$$p_{\vec{r}}(j) = \sum_i r_i h_{ij}. \quad (3.25)$$

The proportionality factors  $h_{ij}$  are known positive numbers, that characterize the measurement by giving the relation of the underlying state  $\vec{r}$  to the probabilities of the measurement outcomes  $p_{\vec{r}}(j)$ . For  $N$  repeated measurements each outcome is recorded  $n_j$  times. For the ideal case the parameter set  $\vec{r}$  can now be reconstructed by solving a system of linear equations

$$p_{\vec{r}}(j) \approx n_j/N = \sum_i r_i h_{ij}. \quad (3.26)$$

However, this system can only be solved, if the number of equations  $j$  is larger than the number of parameters  $i$  that are to be reconstructed. For a good reconstruction  $p_{\vec{r}}(j) \approx n_j/N$  has to be fulfilled, which requires a large number of measurements  $N$ . In the case that this is not possible an alternative is to find the parameter set  $\vec{r}$  with the largest probability of generating the set of measurement outcomes  $n_j$ . This is achieved by maximizing the probability or likelihood

$$\mathcal{L}(\vec{r}) = \prod_i [p_{\vec{r}}(j)]^{n_j}. \quad (3.27)$$

An iterative algorithm, called expectation-maximization algorithm, is initialized by a random parameter set  $\vec{r}$  and increases the likelihood in each step by applying

$$r_i^{(k+1)} = r_i^{(k)} \sum_j \frac{h_{ij} r_j^{(k)}}{p_{\vec{r}}(j)}. \quad (3.28)$$

A global optimum will be reached eventually since the likelihood is a convex function, such that for any two parameter sets  $\vec{r}_1$  and  $\vec{r}_2$

$$\mathcal{L}\left(\frac{\vec{r}_1 + \vec{r}_2}{2}\right) \geq \frac{\mathcal{L}(\vec{r}_1) + \mathcal{L}(\vec{r}_2)}{2} \quad (3.29)$$

holds.

### Quantum states

For a quantum mechanical state that is described by its density matrix  $\rho$  the probabilities for each measurement result can be described as

$$p_\rho(j) = \text{Tr}[\Pi_j \rho], \quad (3.30)$$

where  $\Pi_j$  is a positive operator with  $\sum_j \Pi_j = \mathbb{1}$ . Even though this again produces a set of linear equations, the elements of the density matrix are not necessarily positive or real and their sum not equal to 1. Therefore the approach for the classical case is not valid in the quantum case and a non-negative operator

$$R(\rho) = \frac{1}{N} \sum_j \frac{n_j}{p_\rho(j)} \Pi_j \quad (3.31)$$

has to be defined. The state  $\rho_{ML}$  is the maximum-likelihood state if  $n_j/N \approx p_\rho(j)$  and thus  $R = \sum_j \Pi_j = \mathbb{1}$ . The density matrix  $\rho_{ML}$  that maximizes Eq. (3.27) has to obey the equations [100]

$$\begin{aligned} R(\rho_{ML})\rho_{ML} &= \rho_{ML}R(\rho_{ML}) = \rho_{ML}, \\ R(\rho_{ML})\rho_{ML}R(\rho_{ML}) &= \rho. \end{aligned} \quad (3.32)$$

Again an iterative procedure can be found, that maximizes the likelihood Eq. (3.27). The repetitive iterations

$$\rho^{(k+1)} = \mathcal{N}[R(\rho^{(k)})\rho^{(k)}R(\rho^{(k)})], \quad (3.33)$$

are applied on an initial density matrix like  $\rho^{(0)} = \mathcal{N}[\mathbb{1}]$ , where  $\mathcal{N}$  denotes the normalization to a unit trace. It should be noted, that this procedure does not necessarily approach the global optimum. But even though counter examples exist [101], in practice this situation highly unlikely.

### Homodyne tomography

To reconstruct a state from homodyne tomography, the algorithm has to be slightly adapted. The collected measurements of the quadratures  $\hat{X}_A$  and  $\hat{X}_B$

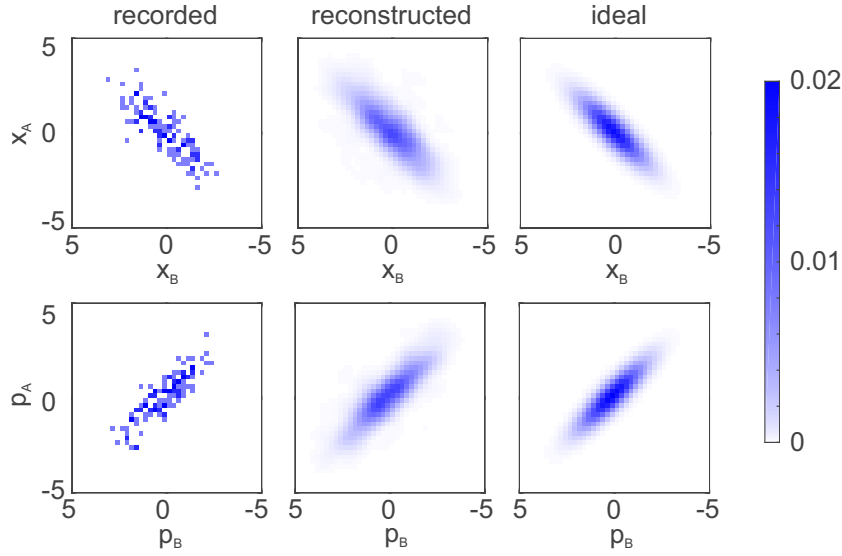


**Figure 3.8: Two dimensional probability distributions.** Recorded distributions of the quadratures (first column), reconstructed distributions (second column) and ideal distributions for a two-mode squeezed state with the reconstructed squeezing parameter  $\xi_{fit} = 0.63$ .

can be binned in 2D histograms for each recorded value of  $\theta$ . This is shown exemplary for  $\hat{X}_{A/B}(0.75\pi) = \hat{p}_{A/B}$  and  $\hat{X}_{A/B}(1.25\pi) = \hat{x}_{A/B}$  in Fig. 3.8. The width of the bins is chosen to be  $dX = 0.25$  and the square bin  $[X_A, X_A + dX], [X_B, X_B + dX]$  is indicated by  $X$ . While in principle smaller bins allow for a reconstruction with higher fidelity, in this case the result did not change significantly for smaller bins, while increasing the computation time drastically. The likelihood function can then be written as

$$\mathcal{L}(\{n_{X,\theta}\}|\rho) = \frac{N!}{\prod_{X,\theta} n_{X,\theta}!} \prod_{X,\theta} p_\rho(X, \theta)^{n_{X,\theta}}, \quad (3.34)$$

with  $n_{X,\theta}$  being the number of measurements in the bin  $X$  for phase  $\theta$  with  $\sum_{X,\theta} n_{X,\theta} = N$  where  $N$  is the total number of measurements. For the case of homodyne tomography the joint probability  $p_\rho(X, \theta) = p_\rho(X|\theta)P(\theta)$  is expressed in terms of  $P(\theta)$ , the fraction of measurements done at angle  $\theta$  and the conditional probability  $p_\rho(X|\theta) = \langle X| U_\theta^\dagger \rho U_\theta |X\rangle$ , where  $|X\rangle = |X_A, X_B\rangle$  and  $U_\theta = e^{-i\theta(n_A + n_B)}$ .

The iteration operator now becomes

$$R = \frac{1}{N} \sum_{X,\theta} \frac{n_{X,\theta}}{P(X|\theta)} U_\theta |X\rangle \langle X| U_\theta^\dagger. \quad (3.35)$$

Eqs. (3.32) hold for this operator and the maximization can be done according to the iteration described by Eq. (3.33). In practice it is necessary to restrict the

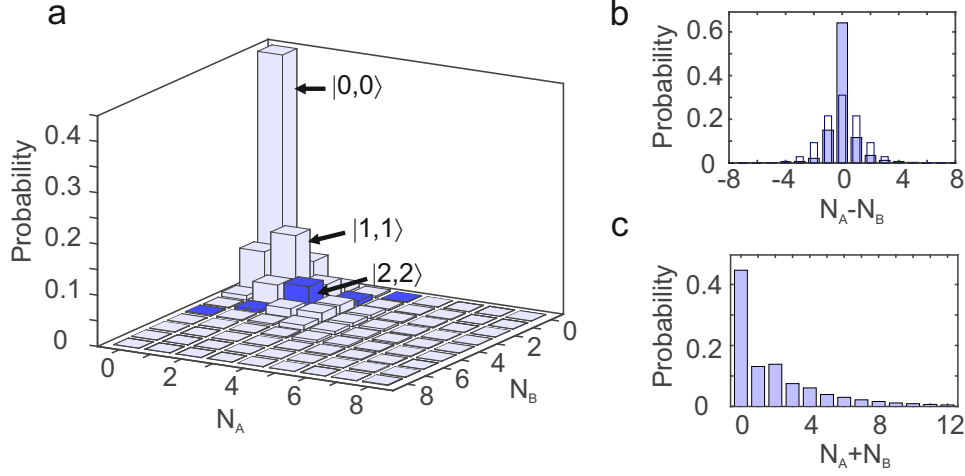


**Figure 3.9: Result of the state reconstruction.** **a** Diagonal elements  $\langle N_A, N_B | \rho | N_A, N_B \rangle$  of the reconstructed density matrix. The biggest contribution is from the vacuum state followed by the two-particle twin Fock state  $|1, 1\rangle$ . For each total particle number  $2n$ , the twin Fock state  $|n, n\rangle$  shows the largest contribution. This is exemplarily highlighted in dark blue for a total of four particles. **b** Reconstructed distribution of the difference of the number of particles in the two modes (solid bars). In comparison to a Poissonian distribution with the same mean number of particles (open bars) the distribution is strongly peaked. **c** Distribution of the total number of particles in the two modes showing an indication of even/odd oscillations that are linked to the pair production of the underlying spin dynamics.

density matrix by excluding Fock contributions over a certain threshold  $n_{cut}$  i.e.  $\rho = \sum_{n_a, n_b, m_A, m_B=0}^{n_{cut}} \rho_{n_a, n_b, m_A, m_B} |n_A, n_B\rangle \langle m_A, m_B|$ .

The result of the reconstruction is shown in Fig. 3.9a by the diagonal elements  $\langle N_A, N_B | \rho | N_A, N_B \rangle$  of the reconstructed density matrix. While the vacuum state  $|0, 0\rangle$  shows the strongest occupation, the creation of atom pairs is witnessed by the predominant contribution of the twin Fock states  $|n, n\rangle$  for a given total particle number  $2n$ . The non-classicality of the state also becomes apparent in the difference and sum of the number of particles  $N_A$  and  $N_B$  in the two modes (see Figs. 3.9b/c). Fig. 3.8 shows the experimental two-dimensional probability distributions in the first row and the reconstructed ones in the second row. The third row shows the ideal distributions with a squeezing parameter of  $\xi_{fit} = 0.63$  obtained from the reconstruction. For the reconstruction, the Fock basis was restricted to  $8 \times 8$  particles. We have checked, that the result doesn't change significantly by using an increased Fock basis. The fidelity of the reconstructed

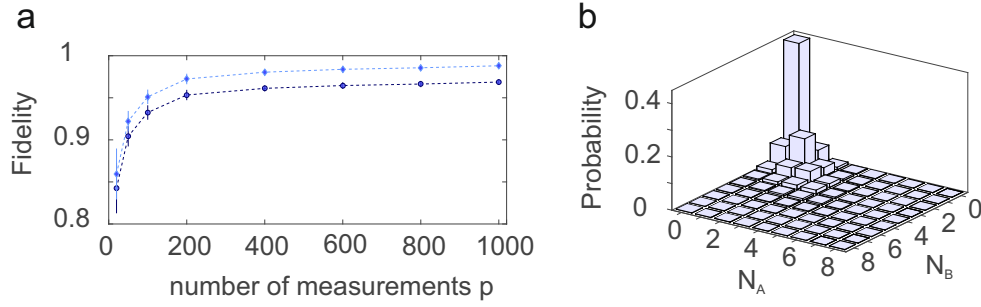


**Figure 3.10: Simulated quantum state tomography.** **a** The quantum fidelity between an ideal simulated reconstruction and the ideal two-mode squeezed vacuum state  $|\xi\rangle$  as a function of the number of measurements  $p$  per each  $\theta$  value.  $n_\theta = 29$  different phase values were used to obtain the simulated data. The dark blue circles indicate a binning of  $dX = 0.25$  and the light blue diamonds a binning of  $dX = 0.1$ . The dashed lines are a guide to the eye. **b** Tomographic reconstruction of a simulated noisy state. The reconstructed state agrees with a quantum fidelity of 90% with the reconstruction from experimental data in Fig. 3.9a.

state with the two-mode squeezed state can be determined as

$$\mathcal{F} = \sqrt{\langle \xi | \rho | \xi \rangle} \quad (3.36)$$

to be 78.4% with a squeezing parameter of  $\xi_{fit} = 0.63$ . As will be shown in the next section the consideration of an appropriate noise model increases this fidelity to 90%. The quantum Fisher information  $F_Q$  for the state projected on a fixed- $N$  subspace is  $F_Q/\bar{n} = 1.5 \pm 0.1 > 1$ , where  $\bar{n}$  is the average number of particles. This indicates a metrological usefulness of the state.

### Simulated quantum state tomography and noise model

As a consistency check for the reconstruction procedure, the reconstruction is applied to simulated data of an ideal two-mode squeezed vacuum. The distribution of the quadratures  $X_{A/B}$  follows the probability  $P(X_{A/B}, \theta) = |\langle \xi | U_\theta | X_{A/B} \rangle|^2$ . A Monte Carlo simulation is then used to generate  $N = pn_\theta$  quadrature data points,  $p$  points for each of the  $n_\theta$  values of  $\theta$ . This simulated data set is treated with the same reconstruction algorithm as the experimental data set.

Fig. 3.10 shows the result of this simulation. The fidelity of the reconstructed state with the ideal two-mode squeezed state is plotted depending on the number of data points  $p$  per  $\theta$  value that were used for the reconstruction. The dark blue circles correspond to a binning of  $dX = 0.25$ , while the light blue diamonds are obtained with  $dX = 0.1$ . With increasing number of measurements and

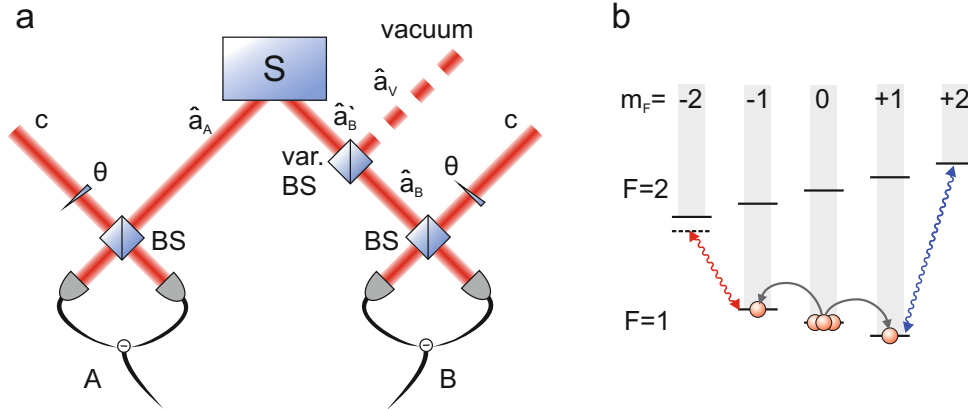


**Figure 3.11: Principle of one-way steering.** **a** One way steering in optics. The prepared squeezed state is sent to two detectors as in the standard homodyne measurement. While the state for detector  $A$  remains unperturbed the state for detector  $B$  is mixed with a variable amount of the vacuum mode on a variable beam splitter before entering the detection zone. With the right amount of vacuum coupling steering from  $A$  to  $B$  can be shown while at the same time steering from  $B$  to  $A$  is not possible [25]. **b** In the atomic system the vacuum contribution can be achieved by a microwave coupling applied to the transition  $|1, 1\rangle \rightarrow |2, 2\rangle$ , depicted in blue, for a variable time. Afterwards the normal homodyne sequence is performed. The microwave coupling that is used to shift the level  $|1, -1\rangle$  to achieve equal energy differences is depicted in red.

decreasing bin size, the fidelity tends to 1. For this simulation, the number of data points  $p$  per  $\theta$  value was kept constant. This was not the case for the experiment, where  $\sim 120$  data points were recorded for the 8  $\theta$  values where  $V_{X(\theta)}^{\pm}$  is minimal and  $\sim 30$  for additional 30  $\theta$  values, amounting to a total of 2864 measurements at 46 different values for  $\theta$ .

The main noise sources in the experiment are phase fluctuations of the condensate in  $m_F = 0$  that acts as the phase reference for the homodyning and fluctuations in the intensity of the radio-frequency coupling pulse. We estimate the phase noise to be  $0.044\pi$  and the intensity noise to be 0.4%. If this simple noise model is included in the simulated quantum state tomography, the experimental data can be matched with a fidelity of 90%. Fig. 3.10b shows the diagonal terms of the reconstructed density matrix from the simulated noisy data. It shows the same characteristic off-diagonal terms as Fig. 3.9a.

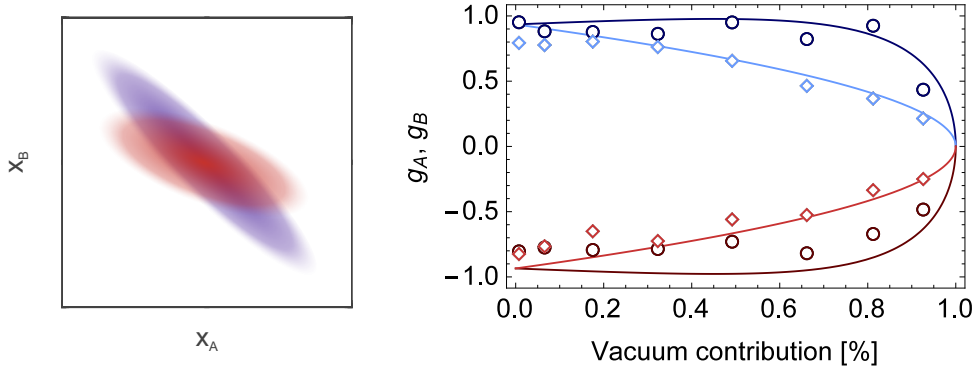


**Figure 3.12: Quadrature distribution for steering and steering factors.** **a** In the case of a vacuum contribution to  $B$ , the quadrature distribution (red) deviates in its angle and width from the quadrature distribution in the undisturbed case (blue). **b** Experimental and theoretical values for the steering factors  $g_{A/B}$ . The factors for the  $x$  quadratures are shown in blue, where the light blue diamonds denote  $g_A$  and the dark blue circles  $g_B$ . The  $p$  quadrature factors are shown in red, with the light red diamonds denoting  $g_A$  and the dark red circles  $g_B$ . The solid lines are the ideal theory curves.

### 3.4 One-way steering

The EPR paradox has an intrinsic directionality that stems from the fact, that one party makes the first measurement and thereby determines the decomposition of the bipartite state and the outcome of the second party's measurement. This process was first termed as "*steering*" by Schrödinger in a response to the original EPR proposal [18]. This directionality wasn't taken into account in the data analysis in the previous chapter, since the state preparation and manipulation is, to a very good approximation, symmetric. It is however possible to introduce an asymmetry to the system.

This one-way steering has been shown for the first time by Händchen et al. [25] in a system of entangled Gaussian modes of light as sketched in Fig. 3.11a. After the state has been prepared, it is sent to two independent detection zones where homodyne detection is performed. This setup shows EPR correlations in both directions, meaning that the measurement at  $A$  can steer the decomposition of the state at  $B$  and vice versa. Now an additional beam splitter is introduced to the path of  $B$ . This beam splitter couples a variable amount of the vacuum mode to the entangled Gaussian mode. If this vacuum contribution is 0%, the original situation is not disturbed. On the other hand, if the vacuum contribution amounts to 100%, steering will not be possible in either direction, since no information about the Gaussian input state reaches the detector of  $B$ . In between these two extrema lies a region where only  $A$  can steer  $B$  but  $B$  cannot steer  $A$ .

The vacuum contribution leads to a change in the quadrature distribution of the state as shown in Fig. 3.12a. The undisturbed distribution is shown in blue and the distribution for a vacuum contribution to  $B$  is shown in red. In the case of the vacuum contribution, the angle of the distribution deviates from the ideal  $45^\circ$  angle towards smaller angles, while the width of the distribution grows larger.

To certify this one-way steering behavior one has to again consider the inference error  $\Delta_{inf}^2 \hat{x}$  introduced in chapter 3.2. Assuming the estimator  $\hat{x}_{est}(\hat{x}_B)$  for the measurement of  $\hat{x}_A$  is of the linear form  $\hat{x}_{est}(\hat{x}_B) = g_B \hat{x}_B + d$ , the best estimator is the one that will minimize

$$\Delta_{inf}^2 \hat{x} = \langle [\hat{x}_A - \hat{x}_{est}(\hat{x}_B)]^2 \rangle = \langle [\hat{x}_A - (g_B \hat{x}_B + d)]^2 \rangle. \quad (3.37)$$

Since  $d$  is only a linearly added constant it does not have to be considered for the inference error. The best choice for  $g_B$  can be found numerically or calculated via linear regression as  $g_B = (\langle \hat{x}_A \hat{x}_B \rangle - \langle \hat{x}_A \rangle \langle \hat{x}_B \rangle) / \Delta^2 \hat{x}_B$ . The minimal inference error is then given by

$$(\Delta_{inf}^2 \hat{x})_{\min} = \Delta^2 (\hat{x}_A - g_B \hat{x}_B). \quad (3.38)$$

Similarly the minimal inference error for the phase quadrature can be calculated as

$$(\Delta_{inf}^2 \hat{p})_{\min} = \Delta^2 (\hat{p}_A + g_B \hat{p}_B). \quad (3.39)$$

The violation of  $(\Delta_{inf}^2 \hat{x})_{\min} (\Delta_{inf}^2 \hat{p})_{\min} \geq 1/4$  would now show a steering of  $A$  by  $B$ . Similarly a criterion for the steering of  $B$  by  $A$  can be expressed as

$$(V_x^- V_p^+)_A^{\min} = \Delta^2 (\hat{x}_B - g_A \hat{x}_A) \Delta^2 (\hat{p}_B + g_A \hat{p}_A) < 1/4. \quad (3.40)$$

If one now shows that the steering criterion holds for one direction that does not necessarily mean that the steering criterion for the other direction is also fulfilled [102].

The ideal theoretical variances and the coefficients  $g_{A/B}$  can now be derived from the EPR case. When regarding Fig. 3.11a, the state  $B$  before homodyning can be described by the operator  $\hat{a}_B = \sqrt{1-R} \hat{a}'_B + \sqrt{R} \hat{a}_V$ , where  $R$  is the vacuum contribution on the variable beam splitter while  $\hat{a}'_B$  and  $\hat{a}_V$  are the operators of the undisturbed state before the variable beam splitter and the vacuum state respectively. For  $R \in \mathbb{R}$ , the quadrature of  $\hat{a}_B$  can then be expressed as

$$\hat{x}_B = \frac{1}{\sqrt{2}} (\hat{a}_B + \hat{a}_B^\dagger) = \sqrt{1-R} \hat{x}'_B + \sqrt{R} \hat{x}_V \quad (3.41)$$

where  $\hat{x}'_B$  and  $\hat{x}_V$  are the quadratures of the undisturbed and the vacuum state. The variances of the undisturbed quadratures  $\hat{x}_A$  and  $\hat{x}'_B$  as well as the covariance  $\langle \hat{x}_A \hat{x}'_B \rangle = 1/2 \sinh 2\xi$  are known from the EPR case. The variance of the vacuum



state  $\langle \hat{x}_V \rangle = 0.5$  is given by shot noise. The covariances  $\langle \hat{x}_A \hat{x}_V \rangle$  and  $\langle \hat{x}'_B \hat{x}_V \rangle$  vanish since there are no correlations with the vacuum state.

This can be used to calculate

$$\begin{aligned}
\Delta^2(\hat{x}_B - g_A \hat{x}_A) &= \langle (\sqrt{1-R} \hat{x}'_B + \sqrt{R} \hat{x}_V - g_A \hat{x}_A)^2 \rangle \\
&= (1-R) \langle \hat{x}'_B \hat{x}'_B \rangle + R \langle \hat{x}_V \hat{x}_V \rangle + g_A^2 \langle \hat{x}_A \hat{x}_A \rangle \\
&\quad + 2\sqrt{R} \sqrt{1-R} \langle \hat{x}'_B \hat{x}_V \rangle - 2\sqrt{1-R} g_A \langle \hat{x}'_B \hat{x}_A \rangle - 2g_A \langle \hat{x}_V \hat{x}_A \rangle \\
&= \frac{1}{2} \cosh 2\xi (1 - R + g_A^2) - \sqrt{1-R} g_A \sinh 2\xi + R/2
\end{aligned} \tag{3.42}$$

and

$$\begin{aligned}
\Delta^2(\hat{x}_A - g_B \hat{x}_B) &= \langle (\hat{x}_A - g_B (\sqrt{1-R} \hat{x}'_B + \sqrt{R} \hat{x}_V))^2 \rangle \\
&= \frac{1}{2} \cosh 2\xi (1 + g_B^2 (1 - R)) - \sqrt{1-R} g_B \sinh 2\xi + g_B^2 R/2.
\end{aligned} \tag{3.43}$$

The functional relations for  $g_{A/B}$  can now be found by a minimization of these variances as

$$\begin{aligned}
g_A &= \sqrt{1-R} \tanh 2\xi \\
g_B &= \frac{\sqrt{1-R} \sinh 2\xi}{(1-R) \cosh 2\xi + R}.
\end{aligned} \tag{3.44}$$

The calculations for  $\Delta^2(\hat{p}_B + g_A \hat{p}_A)$  and  $\Delta^2(\hat{p}_A + g_B \hat{p}_B)$  are completely analogous, where the opposing sign of  $g_{A/B}$  cancels with the opposing sign in the variance.

In analogy to the experimental setup in quantum optics [25], a similar realization can be implemented in an atomic system. The additional beam splitter is replaced by an additional microwave on the transition  $|1, 1\rangle \rightarrow |2, 2\rangle$  that couples the two-mode squeezed state to a vacuum state (see Fig. 3.11b). The duration of the microwave pulse now determines the amount of the vacuum contribution. After this coupling, the normal homodyne measurement is performed. Again, the phase  $\theta$  of the local oscillator is set to  $\theta = 0.75\pi$  and  $\theta = 1.25\pi$  to only measure the  $\hat{x}_{A/B}$  and  $\hat{p}_{A/B}$  quadratures.

While the steering factors  $g_{A/B}$  for the  $\hat{x}_{A/B}$  and  $\hat{p}_{A/B}$  quadratures should theoretically be the same, only with opposing sign, they can differ slightly in the experiment as shown in Fig. 3.12b. While the factors for the  $\hat{x}_{A/B}$  quadrature follow the theory curve, the negative factors for the  $\hat{p}_{A/B}$  quadratures are slightly increased. This is again due to the increased contribution of radio-frequency noise. The steering factors are obtained by minimizing the inferred variances obtained from the experimental data. For a large vacuum contribution the steering factors tend towards zero, since the best estimate for the outcome of the other party's measurement will then also be zero. The slight deviation from  $\pm 1$  for no vacuum contribution is due to the finite squeezing  $\xi$ . For infinite squeezing the factors tend to  $\pm 1$  for zero vacuum contribution.

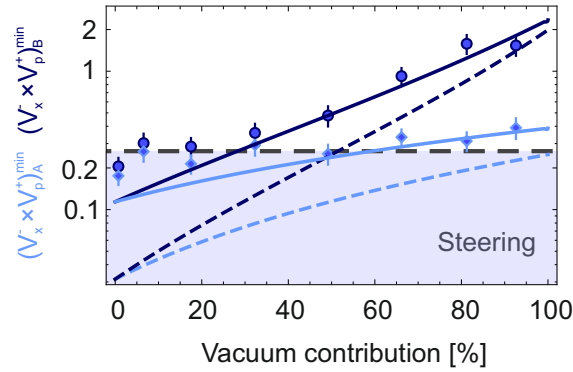


**Figure 3.13: Steering in an atomic system.** Steering criterion Eq. (3.40) for system  $B$  steering system  $A$  (dark blue circles) and vice versa (light blue diamonds) for different contributions of the vacuum state to system  $B$ . The dashed lines show the ideal theoretical variance, while the solid lines show the variance with  $0.044 \pi$  phase noise and radio-frequency noise of  $0.122$ .

The result for the variances of these measurements is shown in Fig. 3.13. While the very low vacuum contribution exhibits two-way steering and the high contributions show no steering in either direction, the one-way steering in between is not significant. The best data point for one-way steering has a vacuum contribution of  $17.5\%$ . For this point  $(V_x^- V_p^+)_{A}^{min} = 0.214$ , which is  $1.25$  standard deviations below the classical limit of  $0.25$  and  $(V_x^- V_p^+)_{B}^{min} = 0.285$ , which is  $0.814$  standard deviations above the classical limit. The significance could be increased by increasing statistics. The deviation from the ideal case, which is depicted as dashed lines, can be partly explained by the same noise contributions that are present in the case of the EPR measurements. The solid lines include  $0.044 \pi$  phase noise and a radio-frequency noise of  $0.122$  as in the EPR case. Due to  $g_{A/B} \neq 1$  the noise of the radio-frequency intensity will not be completely canceled for the variance of the difference in the one-way steering case, which leads to an increased noise.

At the high vacuum contributions the criteria for the two steering directions are clearly gapped, with  $(V_x^- V_p^+)_{A}^{min}$  near the classical limit and  $(V_x^- V_p^+)_{B}^{min}$  steadily increasing, which is an indicator for the directionality of the investigated process.

---

## SUB-SHOT-NOISE INTERFEROMETRY

Since the second was redefined with respect to the microwave transition between two hyperfine levels of the ground state of  $^{133}\text{Cs}$  in 1960, the stability and accuracy of atomic clocks has improved tremendously. Nowadays, microwave clocks operate with stabilities in the  $10^{-16}$  regime [103]. The stability can be improved further by employing transitions with higher frequencies such as optical transitions. By eliminating noise sources in the environment and monitoring all sources that cannot be completely suppressed, such as blackbody radiation, it was recently possible to achieve a stability of  $6.4 \cdot 10^{-18}$  in an optical  $^{133}\text{Cs}$  lattice clock [104].

However, the stability of all interferometers, including atomic clocks, with classical input states is fundamentally limited due to the shot-noise limit. In 1999, the first fundamentally limited microwave clock with a stability of  $4 \cdot 10^{-14}$  was realized [105] and today the best microwave clocks are limited by the shot-noise limit. In the future, this limit will also be a restriction for optical clocks. However, it can be overcome with interferometers that employ squeezed states or more complicated entangled states instead of classical input states.

The following chapter gives a short overview of interferometry, including atom interferometers and their use as frequency standards. The principle of sub-shot-noise interferometry is introduced before the experimental realization of a sub-shot-noise frequency standard is discussed.

### 4.1 Introduction to interferometry

In 1690 Christiaan Huygens published his book "*Traité de la lumière*" (engl. "*Disquisition on light*"), in which he first formulated his theory on wave propagation. He proposed that light propagates as a wave and each diffraction process can be explained by secondary spherical waves that originate at the point of diffraction.

If one assumes that these secondary waves travel only in the forward direction a qualitative explanation of the resulting wave fronts can be given. As a medium for the propagation of light waves Huygens proposed the luminiferous aether. At the beginning of the 19<sup>th</sup> century Fresnel published an extension of Huygens' principle, including the idea of interference, that can be used to predict the outcome of light diffraction experiments such as the double slit experiment by Young performed in 1802.

Early measurements utilizing the interference of light include the measurements on the speed of light by Michelson starting in 1878 and the Michelson-Morley experiment performed in 1887 [106]. A Michelson interferometer with a white light source and a folded path length of 11 m was used to disprove the theory of the luminiferous aether. The idea was to show the relative velocity of the aether to the earth via the interferometric measurement.

Henceforward, the interferometric sensitivity as well as the possible geometric configurations have been improved drastically. Many devices of modern technology rely on interferometers, such as navigation systems that are equipped with fiber optic gyroscopes for rotational sensing. Fig. 4.1a shows the so-called Mach-Zehnder geometry which presents one of the very basic interferometer concepts, that is employed for example in communication technology for demultiplexing. Interferometers with electromagnetic waves are also used in various areas of science including astro-physical observations at different wavelength [107, 108], geodetic studies [109] and medical imaging [110].

### 4.1.1 Atom interferometry

By analyzing the spectrum of black-body radiation, Planck found that the energy of electro-magnetic waves has to be quantized as  $E = hf$ , with  $h$  being Planck's constant and  $f$  the frequency of the wave, in order to replicate experimental observations. This was affirmed by Einstein's explanation for the photoelectric effect in 1905 which includes the postulation of photons with energy  $E = hf = hc/\lambda$ , where  $c$  is the speed of light and  $\lambda$  the wavelength of the photon.

This wave-particle dualism for electro-magnetic radiation was expanded by de Broglie to massive particles by associating a wavelength  $\lambda_{dB}$  to a particle with momentum  $p$  as  $\lambda_{dB} = h/p$ . The first observation of interference of matter waves was observed by diffraction of electron beams in thin metal films and crystalline structures in 1927. In 1961 Young's double slit experiment was repeated by Jönsson with an electron beam instead of light, again observing the associated interference pattern.

This matter wave interference can be utilized to build interferometers as in the optical case. The optical components of beam splitters and mirrors have to be replaced by their analoga for matter waves. A beam splitter can be replaced by a  $\pi/2$  pulse on the corresponding transition creating a superposition of the

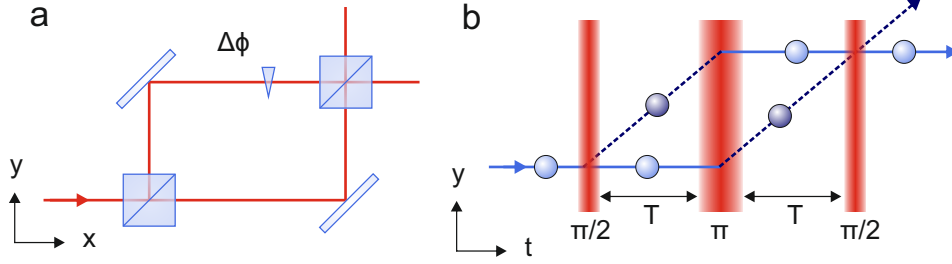


**Figure 4.1: Mach-Zehnder interferometer with light and matter.** **a** An initial beam is divided on a beam splitter. After reflection the beams are recombined on a second beam splitter, whose two output ports provide the readout signal of the interferometer. This signal will depend on the relative phase shift between the two beam paths. **b** With matter waves the same interferometer geometry can be realized. The first Raman-pulse is a  $\pi/2$  pulse which transfers the system from the ground state (light blue, solid lines) to a superposition of the ground state with an excited state (dark blue, dashed lines) that also experiences a momentum transfer of  $2\hbar\vec{k}$ , where  $\vec{k}$  is the wavevector of the light field. After an evolution time  $T$  a Raman  $\pi$  pulse is used to transfer  $2\hbar\vec{k}$  onto both paths while also inverting the states. The interferometer is closed by a second  $\pi/2$  pulse after a second evolution time  $T$ . The signal is read out via the population of the two atomic states.

two states, while a mirror is realized by a two-photon Raman-transition which leads to a momentum transfer of  $2\hbar\vec{k}$ , depending on  $\vec{k}$ , the wavevector of the involved light fields. The Raman-transition can also be used to realize a beam splitter with a momentum transfer on one of the states. These tools can be utilized for matter wave interferometry with various geometries, like a Mach-Zehnder configuration shown in Fig. 4.1b. This configuration is completely analogous to the optical case, in the sense that it encloses an area. While this is necessary for inertial sensing, it is not necessary for atomic clocks. These can be realized without a significant momentum transfer by employing radio-frequency or microwave pulses as beam splitters and omitting the mirror. In that case no area is enclosed in the interferometer.

Atom interferometers can be used for inertial sensing of accelerations [111, 112], including gravitation [113], which can be used for tests of Einstein's equivalence principle [114]. It is also possible to precisely measure gravity gradients [115, 116] and rotations [117–120]. These measurements are not only interesting from a fundamental point of view but also from the more applied side like geodesy for example. It has also been proposed to use atom interferometry for the detection of gravitational waves [121–123]. The measurement of time in atomic clocks will be discussed in the next section.

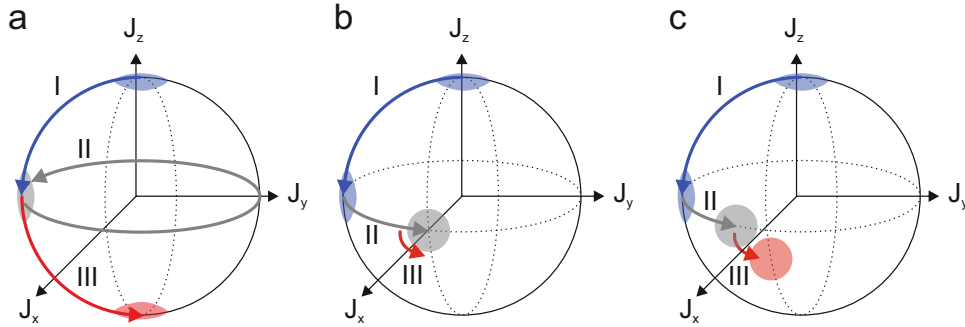


**Figure 4.2: Ramsey measurements with different phases  $\Delta\phi$ .** **a/b/c** The measurement starts with the atomic ensemble prepared in the ground state corresponding to the north pole of the Bloch sphere. I: A  $\pi/2$  pulse rotates the state around the  $J_x$  axis to the equator. II: The phase evolution of  $\Delta\phi = \Delta\omega t$  during the time  $t$  depends on the detuning  $\Delta\omega$  and is depicted by a rotation around the  $J_z$  axis. III: A final  $\pi/2$  pulse, again corresponding to a rotation around  $J_x$  transfers the phase shift to a population imbalance of the ground and excited state. **a** A phase evolution of  $2\pi$  leads to a complete transfer to the excited state, corresponding to the south pole of the sphere. **b** After a phase evolution of  $1.5\pi$  the state rests on the  $J_x$  axis corresponding to a perfect 50 : 50 superposition after the rotation. **c** If the rotation is applied after a phase evolution of  $1.25\pi$  the resulting state shows a population imbalance of the ground and excited states. For perfect  $\pi/2$  rotations, the resulting state will always be in the  $J_y$ -plane.

## 4.1.2 Atomic clocks

In order to operate a frequency standard different constituents need to be realized. A frequency reference is needed as well as an oscillator to probe this reference and a detector to analyze the signal. Depending on this signal a control loop gives a feedback to the probing oscillator. Such a frequency standard can be as a definition for time, if the frequency is suitably divided. In 1967 the second was redefined from the astronomical standard, referenced to the mean length of a solar day, to the atomic standard, referenced to a microwave transition between hyperfine-levels of  $^{133}\text{Cs}$  at 0 K.

The primary  $^{133}\text{Cs}$  standard is considered a passive frequency standard since it acts as the reference which is probed by an external oscillator. Active frequency standards on the other hand are those where the standard itself acts as the oscillator, for example an active hydrogen maser. While cesium is defined as the primary frequency standard many other atomic species can be used to act as a secondary frequency standard, that don't necessarily have to have a larger uncertainty.

The most commonly used probing method was first introduced by Ramsey in 1949 [124]. An ensemble of two-level atoms with ground state  $|0\rangle$  and excited state

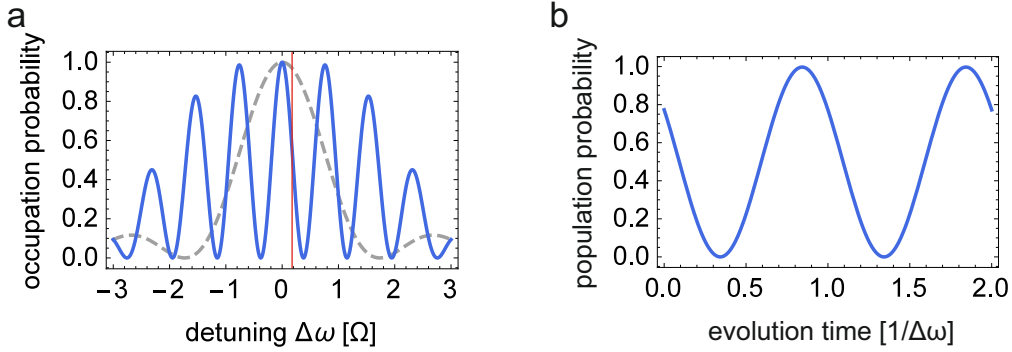


**Figure 4.3: Ramsey measurements for different detunings  $\Delta\omega$  and evolution times  $t$ .** **a** Population probability of the excited state  $|1\rangle$  as a function of the detuning  $\Delta\omega$ . The gray dashed line represents a Rabi transition, while the blue line is calculated for an evolution time  $t$  of  $1/\Omega$ . **b** Population probability of the excited state  $|1\rangle$  as a function of the evolution time  $t$ . The detuning is fixed to  $0.5\Omega$ .

$|1\rangle$  is prepared in the ground state. A  $\pi/2$  pulse is used to create a superposition of the two states. This can be achieved by either driving a single or a two-photon transition. This is depicted on the Bloch sphere in Fig. 4.2 and corresponds to a rotation around the  $J_x$  axis. An evolution time  $t$  follows, during which a phase shift is imprinted onto the ensemble. The phase shift depends on the detuning of the  $\pi/2$  pulse  $\Delta\omega$  from the resonance of the transition and the evolution time as  $\Delta\phi = \Delta\omega t$ . In the Bloch sphere picture, this corresponds to a rotation around  $J_z$  such that a phase shift  $\Delta\phi > 2\pi$  is depicted by multiple rotations around  $J_z$ . A second  $\pi/2$  pulse is applied, which maps the phase shift  $\Delta\phi$  onto a population imbalance between the ground and excited state. This is again depicted by a rotation around  $J_x$  on the Bloch sphere. If the rotation is perfect i.e. it reaches the south pole of the sphere, this corresponds to a complete transfer of the population to  $|1\rangle$  for  $\Delta\phi = n2\pi$ , where  $n$  is an integer (Fig. 4.2a). If  $\Delta\phi = (1 + 2n)\pi$ , the atoms are completely transferred back to the ground state  $|0\rangle$  of the system. If  $\Delta\phi = (1/2 + n)\pi$ , the state rests on the  $J_x$  axis and is therefore in a perfect 50 : 50 superposition after the rotation (Fig. 4.2b). Any phase in between leads to an imperfect transfer resulting in a population imbalance which corresponds to a state vector pointing in between the equator and the poles (Fig. 4.2c). For perfect  $\pi/2$ -pulses, the complete three-part sequence can be expressed as a single rotation around  $J_y$ .

This measurement technique has the advantage that the fringe spacing, and therefore the slope of the population probability as a function of the detuning  $\Delta\omega$ , can be adjusted by the evolution time  $t$ . This is shown in Fig. 4.3a, where a Rabi measurement, without any evolution time (dashed gray) is compared to a Ramsey measurement with an evolution time of  $t = 1/\Omega$ , where  $\Omega$  is the

undetuned Rabi frequency of the transition. Fig. 4.3b shows the population probability of the excited state in dependence on the evolution time  $t$ . For small evolution times, the population probability oscillates with a sinusoidal function. For longer evolution times, the system will start to decohere leading to a damping and a loss of contrast.

### 4.1.3 Sub-shot-noise interferometry

The phase sensitivity of the interferometer can be defined as

$$\Delta\phi = \frac{\Delta P}{\partial\langle P\rangle/\partial\phi}, \quad (4.1)$$

where  $P = N_0/N$  is the transferred fraction with  $N_0$  being the number of atoms in the ground state and  $N$  the total number of atoms.  $\partial\langle P\rangle/\partial\phi$  is the slope of the Ramsey measurement. For uncorrelated particles or successive measurements,  $N_0$  follows a binomial distribution with standard deviation  $\Delta N_0 = \sqrt{N_0(1 - N_0/N)}$ . This fundamental minimal error for  $N$  uncorrelated particles or measurements is called the shot noise limit. It can be reduced by increasing the number of particles or the number of measurements. If the central fringe can now be approximated by a sinusoidal function, the slope and standard deviation cancel, such that the phase sensitivity only depends on the number of particles  $N$  and not on the phase or the detuning, with  $\Delta\phi = \frac{1}{\sqrt{N}}$ .

In practice, the system will experience additional technical noise. Since the overall noise is divided by the slope of the signal in Eq. (4.1), technical noise sources are best suppressed at the middle position of a Ramsey fringe as indicated in red in Fig. 4.3a.

While the shot-noise limit restricts the measurement precision for uncorrelated states, it can be surpassed by correlated states, for example with spin squeezed states. These measurements are then restricted by a more fundamental limit, the Heisenberg limit. This limit is a direct consequence of the Heisenberg uncertainty  $\Delta\phi\Delta(N_1 - N_0) \geq 1$ , where  $\Delta\phi = \Delta(\phi_1 - \phi_0)$  is the variance of the relative phase between the two outputs. If one now assumes the largest possible fluctuations in the particle number difference  $N$ , the Heisenberg limit

$$\Delta\phi \geq 1/N \quad (4.2)$$

follows. As discussed in chapter 2.1.3 the spin squeezing parameter  $\xi$  defines the improvement, a squeezed state can have in a Ramsey measurement as  $\Delta\phi = \xi/\sqrt{N} < 1/\sqrt{N}$ .

The shot-noise limit has been surpassed in multiple experiments by populating both interferometer states symmetrically with an entangled many body state [11, 26–28]. Interferometric sub-shot noise measurements of physical properties include a magnetometer showing a sensitivity 2 dB below shot-noise is



presented in Ref. [29]. The state preparation relies on collective spin squeezing via a QND measurement in laser cooled  $^{87}\text{Rb}$ . Another magnetometer with a suppression of fluctuations of 3.8 dB is realized by employing a one-axis twisting Hamiltonian [30]. Other magnetometers include Ref. [24]. Ref. [32] demonstrates the mapping of a microwave field with a sensitivity of 4 dB below the standard quantum limit. This enhancement is again enabled by using spin squeezed input states that are prepared via the non-linear interactions of a one-axis twisting Hamiltonian. A measurement of a frequency standard 1.1 dB below the shot noise limit has been shown in Ref. [33]. The state was prepared with a quantum non-demolition measurement as presented in chapter 2.2. In Ref. [35] a frequency standard operating 0.57 dB below shot noise has been realized in a system of two entangled trapped  $^9\text{Be}^+$  ions.

Enhancing the interferometer by initializing both input ports with an equally divided entangled ensemble has the disadvantage, that the generation of the input state typically highly depends on the number of atoms and the procedure might therefore not be easily scalable. This competes with the idea of increasing the number of particles to enhance the interferometric sensitivity. The following section presents an alternative approach which circumvents the problem of the varying state preparation for varying particle numbers. The interferometer performance is enhanced by a squeezed vacuum state instead of acting on both input state [36]. This technique is commonly used in optics as for example at the GEO 600 gravitational wave observatory [37].

## 4.2 The three-mode interferometer

We realize a three-mode interferometer, since it can be easily combined with a two-mode squeezed vacuum state, as shown in chapter 3, to enhance the performance of the interferometer.

The important modes for the interferometer are the three modes of the  $F = 1$  manifold. In the following, these modes will be denoted as  $|1, 0\rangle = |0\rangle$  and  $|1, \pm 1\rangle = |\pm\rangle$  and their respective states as  $|N\rangle_i$  with  $i \in \{-1, 0, 1\}$ . The interferometer starts with a BEC in the mode  $|0\rangle$ . During all interferometric couplings that involve the states in  $|\pm\rangle$ , a microwave dressing is applied to the transition  $|-\rangle \rightarrow |2, -2\rangle$  to assure equal resonance conditions between the  $|\pm\rangle$  states. A resonant radio-frequency  $\pi/2$  pulse is applied and transfers 50 % of the atoms to  $|\pm\rangle$  (see Fig. 4.4a). This radio-frequency has to be well tuned to the resonance. If that is not the case the output ports of the interferometer are unbalanced as will be explained in more detail later.

A microwave pulse is applied to the transition  $|0\rangle \rightarrow |2, 0\rangle$  such that all atoms are transferred to  $|2, 0\rangle$  and back to  $|0\rangle$ . If this pulse is resonant, the condensate in  $|0\rangle$  gains a phase of  $\phi = \pi$  with respect to the atoms in  $|\pm\rangle$ . In this case, the

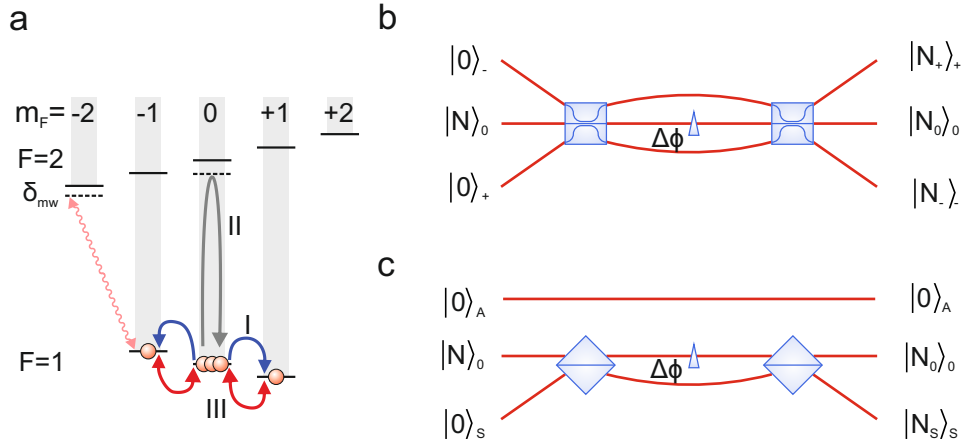


**Figure 4.4: Comparison of a three-mode and a two-mode interferometer.** **a** The interferometric sequence starts with the ensemble in the  $|0\rangle$  state. I: A  $\pi/2$  radio-frequency pulse transfers half of the atoms to the  $|\pm\rangle$  states. II: An off-resonant  $2\pi$  microwave pulse imprints a phase onto the condensate in  $|0\rangle$ . III: A second  $\pi/2$  radio-frequency pulse closes the interferometer. **b** Three mode interferometer. The interferometer is initialized with  $N$  particles in the  $|0\rangle$  mode and squeezed vacuum states in the modes  $|\pm\rangle$ . A three-port beam splitter couples the  $|0\rangle$  mode to the  $|\pm\rangle$  modes. Afterwards a phase shift is applied to the  $|0\rangle$  mode before a second three-port beam splitter closes the interferometer. **c** By changing the basis to the symmetric state  $|S\rangle = 1/\sqrt{2}(|+\rangle + |-\rangle)$  and the anti-symmetric state  $|A\rangle = 1/\sqrt{2}(|+\rangle - |-\rangle)$ . The three-mode interferometer can be reduced to an effective two-mode interferometer, where the interferometer acts on the symmetric mode  $|S\rangle$  and the  $|0\rangle$  mode, while the anti-symmetric mode  $|A\rangle$  propagates unperturbed.

following radio-frequency  $\pi/2$  pulse transfers all atoms back to  $|0\rangle$ . However, if a detuning is applied to the microwave, the atoms gain a different phase, which results in a population of  $|0\rangle$  and  $|\pm\rangle$  after the following  $\pi/2$  pulse.

Fig. 4.4b shows a depiction of the three mode interferometer. The modes  $|\pm\rangle$  are initialized with a two-mode squeezed vacuum state to achieve sub-shot noise sensitivity. A three-way beam splitter (in the atomic case realized by the radio-frequency coupling) couples the initially prepared state  $|N\rangle_0$  with the  $|\pm\rangle$  modes. A phase shift is applied to the mode  $|0\rangle$  before a second three-way beam splitter closes the interferometer.

If the basis is changed to the symmetric and anti-symmetric superposition of  $|\pm\rangle$ , the three-mode interferometer can be reduced to a two-mode interferometer. Fig. 4.4c shows this two-mode interferometer, where the input modes are given by  $|S\rangle = 1/\sqrt{2}(|+\rangle + |-\rangle)$ ,  $|A\rangle = 1/\sqrt{2}(|+\rangle - |-\rangle)$  and  $|0\rangle$ . The symmetric mode  $|S\rangle$  and  $|0\rangle$  form the interferometer. They are coupled by a two-way beam splitter,

a phase shift is applied to  $|0\rangle$  and a second two-way beam splitter closes the interferometer. The asymmetric mode stays unperturbed, which can be easily seen if one considers the Hamiltonian for the coupling in the new two-mode basis. Under the assumption that the Rabi frequencies for the two transitions are equal, with  $\Omega_{\pm 1} \approx \Omega$ , the Hamiltonian associated with the radio-frequency coupling can be written as

$$\begin{aligned}
H_{rf} &= \frac{\hbar\Omega_+}{2\sqrt{2}}(a_+^\dagger a_0 + a_+ a_0^\dagger) + \frac{\hbar\Omega_-}{2\sqrt{2}}(a_-^\dagger a_0 + a_- a_0^\dagger) \\
&= \frac{\hbar\Omega}{2} \left[ \frac{1}{\sqrt{2}}(a_+^\dagger + a_-^\dagger)a_0 + \frac{1}{\sqrt{2}}(a_+ + a_-)a_0^\dagger \right] \\
&= \frac{\hbar\Omega}{2} [a_S a_0^\dagger + a_S^\dagger a_0] \\
&= \hbar\Omega J_x,
\end{aligned} \tag{4.3}$$

with  $a_i$  being the annihilation operators of the states and  $J_x = \frac{1}{2}(a_0^\dagger a_S + a_S^\dagger a_0)$  the spin operator. Similarly, the two-mode squeezing Hamiltonian can be written as the difference of the single mode squeezing Hamiltonians  $H_{A/S} = \frac{1}{2}\hbar\Omega (a_{A/S}^\dagger a_{A/S}^\dagger + a_{A/S} a_{A/S})$  as

$$\begin{aligned}
H &= \hbar\Omega (a_+^\dagger a_-^\dagger + a_+ a_-) \\
&= \frac{1}{2}\hbar\Omega ((a_S^\dagger + a_A^\dagger)(a_S^\dagger - a_A^\dagger) + (a_S + a_A)(a_S - a_A)) \\
&= H_S - H_A,
\end{aligned} \tag{4.4}$$

with  $[a_S, a_A] = 0$ . The same technique is used in optics, where a two-mode squeezed vacuum, generated by parametric down conversion, is transformed to single mode squeezed vacuum. This is accomplished by mixing the signal and idler beams on a beam splitter and working with either the symmetric or anti-symmetric superposition [94]. Thus, both the interferometer pulses and the squeezed input state can be described in the two-mode picture instead of the three-mode picture. The symmetric mode  $|S\rangle$  has the advantage, that it is independent of magnetic field fluctuations in first order. Thus, the involved states have the same advantages as conventional clock states.

The two-mode interferometer can be depicted on the Bloch sphere with basis  $|0\rangle$  and  $|S\rangle$  as shown in Fig. 4.5. The sequence starts with a state prepared on the north pole of the Bloch sphere. The squeezed vacuum can be prepared in an arbitrary direction. Here depicted are the two extrema, squeezing in the phase quadrature Fig. 4.5a and squeezing in the amplitude quadrature Fig. 4.5b. This corresponds to a reduced uncertainty on the Bloch sphere in either  $J_x$  or  $J_y$  direction. The first radio-frequency pulse now performs a quarter rotation around the  $J_x$  axis. The following microwave pulse induces a phase evolution, corresponding to a rotation around  $J_z$ . Depicted here is a relative phase of

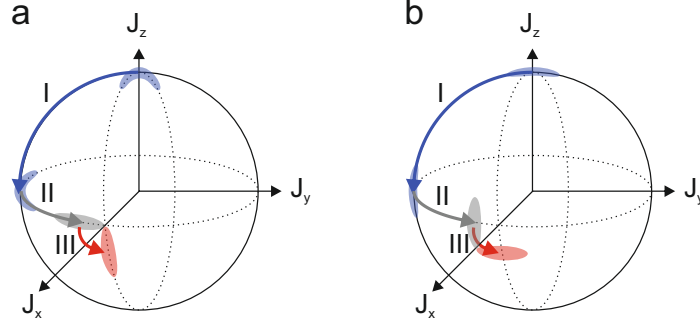


**Figure 4.5: Interferometric sequence depicted on the Bloch sphere.** **a/b** The interferometer starts with an input state on the  $J_z$  pole, i.e. all atoms are in the state  $|0\rangle$ . In **a** the input state is squeezed in the  $J_x$  direction and in **b** in  $J_y$ . I: A radio-frequency  $\pi/2$  pulse is applied, which rotates the state around  $J_x$  by coupling the input state  $|0\rangle$  to the symmetric state  $|S\rangle = 1/\sqrt{2}(|+\rangle + |-\rangle)$  (depicted in blue). II: A variable phase shift is applied via an off-resonant coupling between  $|0\rangle$  and  $|2,0\rangle$ . This rotates the state around  $J_z$ . Here depicted in gray is a phase shift  $< \pi/2$ . III: A final radio-frequency  $\pi/2$  pulse rotates around  $J_x$ . The final state is depicted in red. For **a** the interferometer output is anti-squeezed while for **b** it is squeezed along  $J_z$ .

$\phi < \pi/2$ . The final  $\pi/2$  pulse rotates again around the  $J_x$  axis. Depending on the direction of the squeezing of the input state, the output is anti-squeezed (a) or squeezed (b) along  $J_z$ . The whole interferometer can therefore be expressed as a rotation around  $J_y$ .

The radio frequency  $\pi/2$ -pulses are described by  $U_{rf} = \exp(-i\pi/2J_x)$ . The phase shift applied to the  $m_F = 0$  condensate can be written as  $U_{ps} = \exp(-i\phi a_0^\dagger a_0)$ , where  $a_0^\dagger a_0 = J_z + N/2 - a_A^\dagger a_A/2$  and  $N = a_0^\dagger a_0 + a_S^\dagger a_S + a_A^\dagger a_A$ . If one now neglects the overall phase shift  $\exp(-i\phi/2N)$ , the phase shift simplifies to  $U_{ps} = \exp(-i\phi J_z) \exp(i\phi/2a_A^\dagger a_A)$ . The overall transformation of the interferometer can be expressed as

$$\begin{aligned}
 U_{int} &= U_{rf} U_{ps} U_{rf} \\
 &= e^{i\pi/2J_x} e^{-i\phi J_z} e^{i\phi/2a_A^\dagger a_A} e^{-i\pi/2J_x} \\
 &= e^{i\pi/2J_x} e^{-i\phi J_z} e^{-i\pi/2J_x} e^{i\phi/2a_A^\dagger a_A}
 \end{aligned} \tag{4.5}$$

and since  $[a_A, J_x] = 0$  the phase shift to the antisymmetric mode can be treated independently from the rest of the transformation. The first part of the equation,  $e^{i\pi/2J_x} e^{-i\phi J_z} e^{-i\pi/2J_x}$ , can then be simplified by using the associated rotation matrices

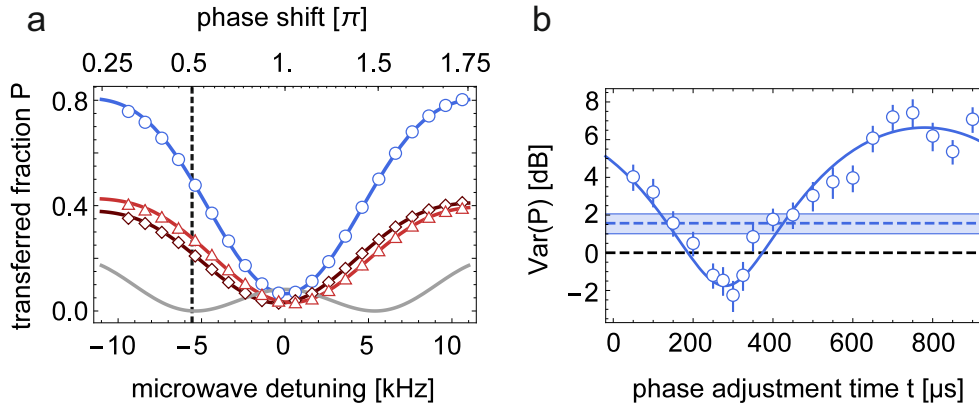


**Figure 4.6: Interferometer for different microwave detunings and different input states.** **a** Transferred fraction  $P$  in the interferometer for different microwave detunings. The microwave detuning directly corresponds to the imprinted phase. The blue data marks the transferred fraction  $P$ , while the light and dark red data mark the fraction transferred to the  $|\pm\rangle$  states. The solid lines are a theory fit from the single particle calculation. The gray line marks the fraction transferred to the  $F = 2$  manifold. The black dashed line marks the mid-fringe position that further measurements are performed at. This position of  $-5.6$  kHz detuning corresponds to a phase of  $0.5\pi$ . The error bars are on the order of the size of the plot markers. **b** Variance  $\text{Var}(P)$  of the transferred fraction  $P$  with respect to shot noise as a function of the input state, measured at the mid-fringe position. The input state is varied via the phase adjustment time  $t$ . The blue solid line is a  $\sin^2$  fit to the data. The black dashed line corresponds to shot noise, while the blue dashed line corresponds to the interferometer with a classical input state.

as

$$\begin{aligned}
 & \begin{pmatrix} 1 & 0 & 0 \\ 0 & \cos \pi/2 & -\sin \pi/2 \\ 0 & \sin \pi/2 & \cos \pi/2 \end{pmatrix} \begin{pmatrix} \cos \phi & -\sin \phi & 0 \\ \sin \phi & \cos \phi & 0 \\ 0 & 0 & 1 \end{pmatrix} \begin{pmatrix} 1 & 0 & 0 \\ 0 & \cos \pi/2 & -\sin \pi/2 \\ 0 & \sin \pi/2 & \cos \pi/2 \end{pmatrix} \\
 &= \begin{pmatrix} \cos \phi & 0 & \sin \phi \\ 0 & -1 & 0 \\ \sin \phi & 0 & -\cos \phi \end{pmatrix} = \begin{pmatrix} \cos \pi - \phi & 0 & \sin \pi - \phi \\ 0 & 1 & 0 \\ -\sin \pi - \phi & 0 & \cos \pi - \phi \end{pmatrix} \begin{pmatrix} -1 & 0 & 0 \\ 0 & -1 & 0 \\ 0 & 0 & 1 \end{pmatrix} \quad (4.6)
 \end{aligned}$$

which corresponds to a spatial transformation around the  $J_z$  axis and a rotation around  $J_y$ .

In Fig. 4.6a the fraction  $P = (N_+ + N_-)/N$  of the population transferred to  $|\pm\rangle$ , which corresponds to the population of the symmetric state, is plotted against the detuning of the microwave  $2\pi$ -pulses. For this measurement, the pulse duration was set to  $90.4 \mu\text{s}$  which is the perfect time for the detuning that results

in the mid-fringe position. Since the pulse length is not adjusted to the perfect  $2\pi$ -pulse for all other detunings, it leads to a population of  $|2, 0\rangle$ , and therefore to a population of  $|2, \pm 1\rangle$  after the final radio-frequency  $\pi/2$ -pulse. The behavior of the interferometer can be well simulated by a simple single-particle simulation as shown by the blue solid line. The detuning  $\delta$  directly corresponds to the phase  $\phi$  imprinted on the  $|0\rangle$  condensate via

$$\phi = \left( \frac{\delta}{\sqrt{\Omega_0^2 + \delta^2}} + 1 \right) \pi, \quad (4.7)$$

where  $\Omega_0$  is the undetuned Rabi frequency of the transition.

The mid-fringe position of  $\pm 5.6$  kHz detuning is used for further measurements. A squeezed vacuum state is prepared in the  $|\pm\rangle$  states. This state is prepared by initiating spin dynamics in the  $m_F = 0$  condensate for 32 ms with a spin dynamics rate of  $\Omega = 2\pi 3.9$  Hz, which creates a mean atom number of 0.75 atoms in the  $|\pm\rangle$  modes. The number of atoms in the  $|0\rangle$  state is on the order of  $10^4$ , thus, the influence of the asymmetric state to interferometer is negligible, while the symmetric state enhances its performance drastically.

The direction of the squeezing is varied via a phase adjustment time  $t$  as explained in chapter 3. The results of chapters 3.2.3 and 3.3.1 can also be viewed as a state characterization of this squeezed input state. Fig. 4.6b shows the variance  $\text{Var}(P)$  of the transferred fraction  $P$  for varied phase adjustment times  $t$  from 25  $\mu\text{s}$  to 900  $\mu\text{s}$ . The variance reaches a minimum of 2.25 dB below shot noise at  $t = 300$   $\mu\text{s}$ . This corresponds to the case of the anti-squeezed variance of the transferred fraction before the final  $\pi/2$ -pulse as shown in Fig. 4.5b. Fig. 4.5a corresponds to  $t = 800$   $\mu\text{s}$ .

To evaluate the phase sensitivity of the interferometer, the slope around the mid-fringe position is measured. This is shown in Fig. 4.7a. The slope can be approximated by a linear fit (solid blue line), which agrees quite well with the single particle simulation (black dashed line). A slope of  $\partial P/\partial\phi = 0.474 \pm 0.003 \text{ rad}^{-1}$  is reached, which compares well to the theoretical optimum of  $(\partial P/\partial\phi)_{\text{max}} = 0.5 \text{ rad}^{-1}$  for the interferometer discussed here.

The phase sensitivity, defined according to Eq. (4.1), is depicted in dark blue in Fig. 4.7b. A good estimator  $\Delta^2\phi_{ST}$  for the short term sensitivity can be defined via the first point of the Allan variance, depicted in dark blue, as

$$\Delta^2\phi_{ST} = \frac{1}{2N} \sum_{i=1}^N \left( \frac{p_i - p_{i+1}}{\partial P/\partial\phi} \right)^2, \quad (4.8)$$

where  $N$  is the total number of measurements and  $p_i$  are the outcomes of these measurements. The mean short term sensitivity is  $1.50 \pm 0.15$  dB below the shot noise limit.

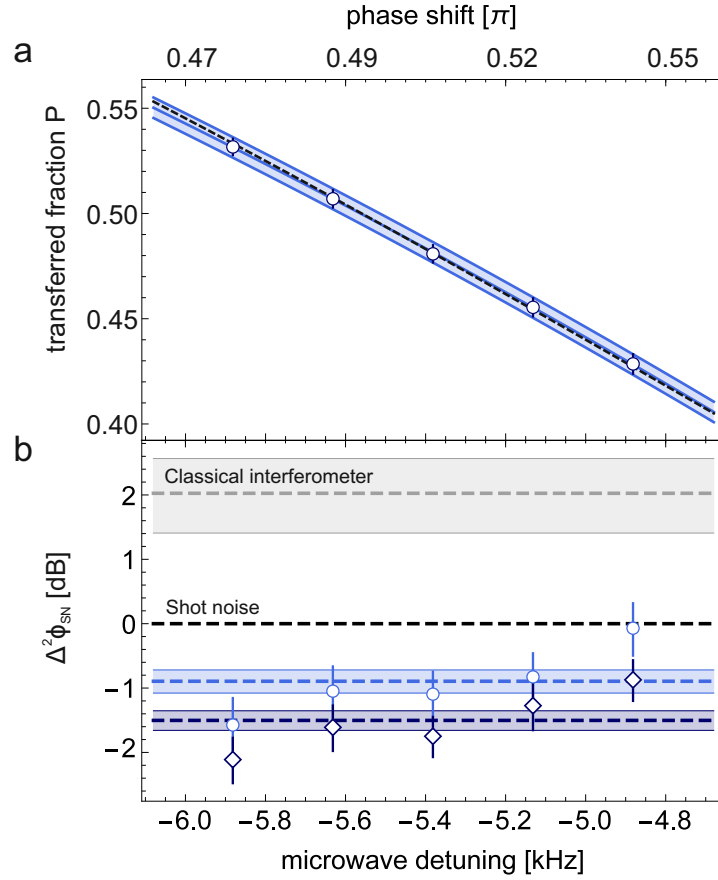


**Figure 4.7: Slope and sensitivity of the interferometer around the mid-fringe position.** **a** Transferred fraction  $P$  as a function of the phase shift or microwave detuning, measured around the mid-fringe position of  $0.5\pi$  phase shift. The black dashed line is the single-particle simulation, while the blue solid line is a linear fit to the data with an error region corresponding to shot noise. The slope of the linear fit is  $0.474 \pm 0.003 \text{ rad}^{-1}$  which agrees well with the theoretical optimum of  $0.5 \text{ rad}^{-1}$ . **b** Phase sensitivity  $\Delta^2\phi_{\text{SN}}$  with respect to shot noise (black dashed line) as a function of the phase shift or microwave detuning. The sensitivity of the classical interferometer is depicted in gray. The dark blue data points represent the short term sensitivity of the interferometer with a mean sensitivity of  $1.50 \pm 0.15 \text{ dB}$  below shot noise (dashed, dark blue line). The light blue data points show the sensitivity of the interferometer with the mean sensitivity depicted by the dashed light blue line.

The transition  $|0\rangle \rightarrow |2,0\rangle$ , which serves as the clock transition, has a frequency of  $\sim 6.8 \text{ GHz}$ . This leads to a minimal fractional instability of  $6.09 \cdot 10^{-10}$  for the first point of the measurement in Fig. 4.7b. The averaging behavior can be evaluated by the Allan variance as shown in Fig. 4.8. The features that can

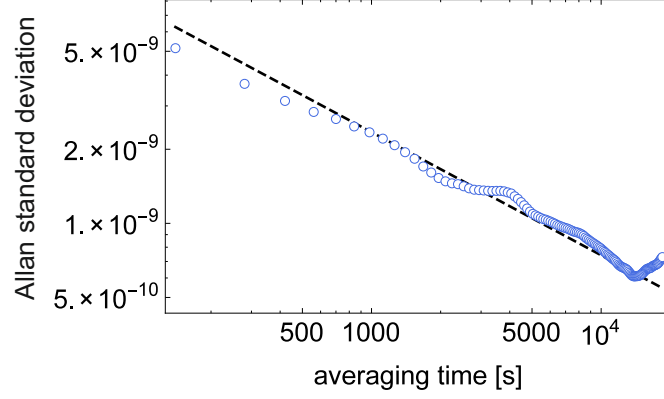


**Figure 4.8: Allan variance of the fractional instability.** The fractional uncertainty as a function of the averaging time. The data set is the same as for the first data point of Fig. 4.7. The black dashed line represents shot noise. The averaging stays below the shot noise limit until it is dominated by environmental noise.

be seen at an averaging time of  $\sim 1000$  s and  $\sim 4000$  s are associated with the air conditioning cycle in the lab. A second, larger feature arising at  $\sim 1.5 \cdot 10^4$  s is related to the day-night cycle in the lab.

### Single-particle model

The transferred fraction after the interferometer can be well simulated by a single-particle model. It is governed by the three Rabi frequencies of the involved transitions.  $\Omega_0$  represents the undetuned Rabi frequency of the transition  $|0\rangle \rightarrow |2,0\rangle$ , while  $\Omega_{\pm}$  represent the frequencies associated to the transitions  $|0\rangle \rightarrow |\pm\rangle$ . Each of these transitions has an associated detuning  $\delta_i$ .

The simulation will be restricted to the states  $|0\rangle, |\pm\rangle$  and  $|2,0\rangle$ , which will be represented by their respective relative population  $a_i$ . Initially, the system is prepared in the state  $(a_+, a_0, a_-, a_2) = (0, 1, 0, 0)$ .

The radio-frequency coupling is represented by the time evolution  $H_{rf}(t) = \exp(itH_{rf})$  with

$$H_{rf} = \frac{1}{2\sqrt{2}} \begin{pmatrix} \delta_{\pm} & \Omega_{+} & 0 & 0 \\ \Omega_{+} & 0 & \Omega_{-} & 0 \\ 0 & \Omega_{-} & -\delta_{\pm} & 0 \\ 0 & 0 & 0 & 0 \end{pmatrix}. \quad (4.9)$$

The microwave coupling can similarly be described by

$$H_{mw} = \frac{1}{2} \begin{pmatrix} \delta_{\pm} & 0 & 0 & 0 \\ 0 & 0 & 0 & \Omega_0 \\ 0 & 0 & -\delta_{\pm} & 0 \\ 0 & \Omega_0 & 0 & -2\delta_0 \end{pmatrix} \quad (4.10)$$



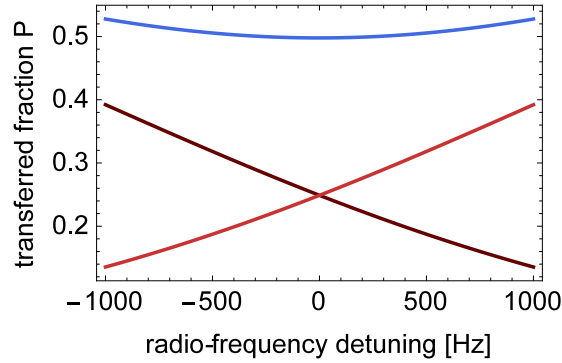


**Figure 4.9: Transferred fraction  $P$  for different radio-frequency detunings.** While the total transferred fraction  $P$  (blue) stays constant for small detunings the fraction of atoms in  $|\pm\rangle$  (dark and light red) show opposite trends with the detuning.

and its time evolution  $U_{mw}(t) = \exp(itH_{mw})$ . The complete interferometer is then simulated by

$$\begin{pmatrix} a_+ \\ a_0 \\ a_- \\ a_2 \end{pmatrix}_{out} = U_{rf}(t_3)U_{mw}(t_2)U_{rf}(t_1) \begin{pmatrix} a_+ \\ a_0 \\ a_- \\ a_2 \end{pmatrix}. \quad (4.11)$$

When comparing the result of the model to the measured data, one has to take into account the detection scheme which leads to an overlap, and therefore only a simultaneous detection, of  $|0\rangle$  with  $|2, 0\rangle$  and of  $|\pm\rangle$  with  $|2, \pm 1\rangle$ . Fig. 4.6 shows the comparison of this model with the measured data. The gray line shows the fraction of atoms transferred into the  $F = 2$  manifold. The distribution of these atoms to  $|2, \pm 1\rangle$  and the simultaneous detection is taken into account in the red curves corresponding to the fraction of atoms in  $|\pm\rangle$  and the blue curve, the sum of those. The slight imbalance of the  $|\pm\rangle$  modes originates from a small detuning in the radio-frequency. Fig. 4.9 shows the transferred fraction in the  $|\pm\rangle$  modes as a function of the radio-frequency detuning. The fractions in the  $|\pm\rangle$  modes, shown in light and dark red, show opposite trends with the detuning which leads to a nearly constant total transferred fraction  $P$ , which is depicted in blue. A change in magnetic field has the same effect as a change in radio-frequency. This shows, that the interferometer is not sensitive to moderate magnetic field fluctuations.



---

# AUTOMATIZED OPTIMIZATION

The use of optimization algorithms is wide spread in most fields of experimental physics, including the setup and adjustment of accelerator [125, 126] and decelerator [127] beam lines, automated scanning probe microscopy in solid state physics [128] or the shaping of ultrashort laser pulses [129, 130]. The rapid development of new preparation and manipulation techniques in the field of ultracold quantum gases led to experiments with growing complexity and an increasing number of adjustable parameters. While most parameters in cold atom experiments are computer controlled, optimization is still mainly done manually. Especially in experiments with a high-dimensional parameter space and unknown correlations, this can be a time consuming task. Therefore most experiments benefit from an automated optimization. An automated optimization of up to four correlated parameters in such an experiment has been shown in Ref. [131, 132]. Recently, an up to 16-dimensional optimization of a BEC experiment was presented, utilizing a machine-learning based algorithm, where a model of the target space is developed in order to optimize the process [133].

The chapter will give a short introduction to optimization before explaining the Differential Evolution algorithm and its extensions used for optimization in an atom optics setup. A simulation of the algorithm is presented which evaluates its performance before applying it to a 21-dimensional optimization task in an experimental setup. The main results of this chapter are published in Ref. [134].

## 5.1 The optimization algorithm

An optimization problem consists of two main parts. First, one has to formulate a target function that has to be optimized. In an atom optics setting this target function can for example be atom number or temperature or also a compound function that includes multiple objectives. Since any optimization problem can

be traced back to a maximization problem, only the maximization will be considered in the following. Second, the parameter space on which the optimization takes place has to be defined and appropriately restricted. For the experiment, the parameter space consists for example of currents, that provide magnetic fields, strength and detunings of light fields or timings in the experimental cycle. These different parameters will be regarded as the different dimensions of the parameter space. The boundaries for these parameters would need to be set such that they are experimentally feasible, i.e. restrict currents such that they do not overheat the system. Now that the target function and the parameter space are defined, an optimization approach can be started.

Optimization strategies can be divided into two groups, derivative-based searches and derivative-free searches. While derivative based approaches work well for unimodal, differentiable target functions they are not feasible in an experimental setting with an unknown target function that might contain multiple local optima. Another problem that the optimization has to be able to overcome is the different scaling of the different dimensions in the parameter space. The optimization still has to be efficient, even if one parameter has a very small or big influence on the outcome or a large or small parameter space compared to the other parameters. Even for modern experiments with cycling times in the few second range it is important to find an optimization strategy that finds the optimum quickly. Also, the time scaling for increasing parameter spaces or increasing number of dimensions has to be favorable. The scaling has to be compared to that of a simple grid-based optimization, where the parameter space is incrementally searched. For that case the effort grows exponentially with the number of parameters, which a well scaling algorithm should be able to beat.

### 5.1.1 Differential Evolution

One such algorithm is "*Differential Evolution*" (DE), which was first proposed in 1995 [135]. The algorithm is well understood and has been tested on a variety of problems, mainly in computer science [136, 137]. It finds the global optimum of an objective function in a high dimensional parameter space while scaling favorably with an increasing parameter space.

DE belongs to a family of optimization strategies that are called evolutionary algorithms, since they operate on generations of populations that are gained from the previous generation via a mutation process. Each generation consists of multiple vectors on the parameter space. Evolutionary algorithms rely on "survival of the fittest" such that the target functions of vectors are compared to those of the previous generation and the best performing vectors are chosen to form the next generation.

The basic sequence of DE is outlined in Fig. 5.1. For each optimization the number  $N$  of  $d$ -dimensional vectors on the  $d$ -dimensional parameter space has

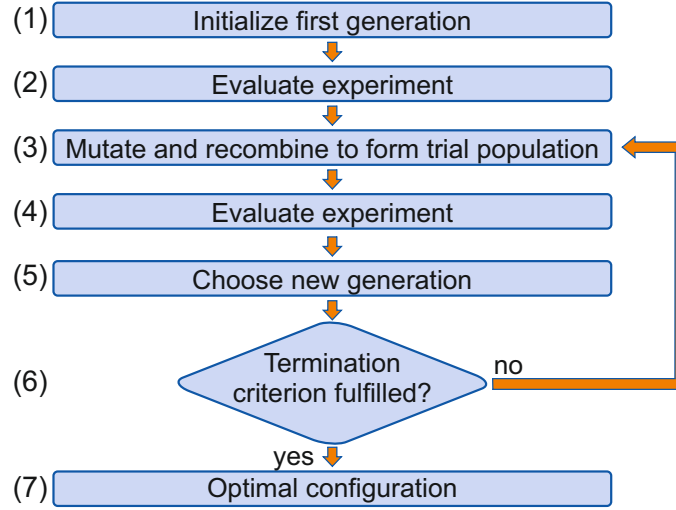


**Figure 5.1: Graphical representation of Differential Evolution.** (1) The first generation is randomly initialized. (2) The target function is evaluated i.e. the experiment is run for every parameter vector of that generation. (3) The current generation is mutated to form a trial population. (4) This trial population is again evaluated. (5) If a better result is achieved by a vector in the trial population than in the original one, the new candidate replaces the old one. (6) The process is repeated until a termination criterion is fulfilled, which (7) indicates that the optimal configuration is reached.

to be chosen with regard to the specific optimization problem. The initial generation  $\{\vec{x}_i | i \in [0, N - 1]\}$  is randomly distributed over the whole parameter space with lower boundaries  $L^n$  and upper boundaries  $U^n$ , where  $n \in [0, d - 1]$ . Alternatively, different strategies for the distribution of the first generation can be used. If the optimum can be guessed with good confidence but the parameter space should not be restricted it can be feasible to form a Gaussian distribution around said optimum to enhance convergence times. In other scenarios it can be favorable to distribute the initial vectors evenly or restrict the parameter space for initial distribution only. This first generation is then evaluated in the experiment.

A two step process is applied to form a trial population  $\{\vec{u}_i | i \in [0, N - 1]\}$ . A mutated population  $\{\vec{v}_i | i \in [0, N - 1]\}$  is generated before each mutated vector  $\vec{v}_i$  is combined with one vector  $\vec{x}_i$  from the original generation. The resulting vectors  $\vec{u}_i$  now form the trial population that is evaluated in the experiment. For the mutation process, three randomly chosen, mutually exclusive vectors  $\vec{x}_k, \vec{x}_l, \vec{x}_m$  with  $k, l, m \in [0, N - 1]$  are picked from the original generation for each original vector  $x_i$ . They are combined via

$$\vec{v}_i = \vec{x}_k + F(\vec{x}_l - \vec{x}_m), \quad (5.1)$$

where  $F \in ]0, 1]$  is the amplification constant, which determines the step size of the mutation on the parameter space. The amplification constant has to be chosen such that it neither prohibits convergence by mutation steps that are too large nor increases the time needed for convergence drastically by a very small step size.

To enhance the convergence speed a second constant  $E \in ]0, 1]$  called the elite parameter can be introduced. The vectors  $\vec{x}_k, \vec{x}_l, \vec{x}_m$  are then not picked from the entire set but from a subset of the vectors with the best performance, where the relative size of the subset is determined by  $E$ . If  $E$  is chosen too small, it can lead to a premature convergence on a not optimal configuration since the choice of parent vectors for the mutation process is restricted on too small a subset.

The components of  $\vec{v}_i$  are tested with respect to the boundaries  $L^n$  and  $U^n$ . If a component falls outside of these boundaries it is set on the appropriate boundaries. Other approaches include a mirroring of the component on the boundary to place it again inside the parameter space. While this can be advantageous for certain optimization tasks, especially those where the optimum is not expected to lie on a boundary, it slows convergence if the optimum does lie on the boundary, which is expected at least in some experimental cases.

The combination of  $\vec{x}_i$  and  $\vec{v}_i$  yields a new vector  $\vec{u}_i$  that is part of the trial population. To this end individual components of  $\vec{x}_i$  are replaced by the associated component of  $\vec{v}_i$ . Each component has a probability  $CR$  of being replaced by the mutated component.  $CR \in ]0, 1]$  is called the crossover parameter. To ensure that at least one component of each vector is altered, a component  $x_i^m$  is chosen for each vector and replaced by  $v_i^m$ , where  $m$  is randomly chosen for each vector. This means that for each vector a random integer  $m_i \in [0, d - 1]$  is generated and a random real number  $X_i^n \in ]0, 1]$  is generated for each component  $n$  of each vector  $i$ . The trial vector is then build according to

$$u_i^n = \begin{cases} v_i^n & ; X_i^n \leq CR \vee n = m_i \\ x_i^n & ; \text{otherwise.} \end{cases}$$

Each vector  $\vec{u}_i$  of this trial population is evaluated with respect to the target function. The results are compared pairwise to the results of the previous generation. This means the result of  $\vec{u}_i$  is compared to that of its base vector  $\vec{x}_i$ . The better performing vector is chosen for the next generation. Thus, each generation and its corresponding trial population form the next generation which outperforms the previous one. A repetition of this process then leads to a convergence towards the global optimum.

### 5.1.2 Limited Lifetime Differential Evolution

While DE works well in many situations, it has to be adapted to cope with noisy target functions. Two types of noise are common in atom optics experiments.

The first comes from shot to shot fluctuations due to technical noise, the second from drifts in the environment for example room temperature drifts that influence laser powers. Therefore, an extension to DE was developed to improve the performance in noisy environments. The extended algorithm is called "*Limited Lifetime Differential Evolution*" (LILDE).

Each vector that survives a certain number of generations is considered to be outdated and is remeasured. While this increases the number of measurements that need to be performed for a noiseless system, it avoids problems with a noisy target function. If no such lifetime is introduced the generations accumulate falsely high rated vectors, that only performed well due to shot to shot fluctuations. If the system is subjected to a drift that lowers its overall performance a false optimum might be reached which performed well at the beginning of the experiments but would not perform well after the optimization is completed.

For an analytic function the optimum is known and therefore convergence can easily be tested. In a real life optimization problem a criterion for convergence has to be developed. Strategies discussed in literature [138] include schemes that target the improvement of one generation compared to the previous one. If this improvement diminishes this can be sign for convergence. Other schemes target the distribution of the vectors in the parameter space or the average movement of a vector compared to its counterpart in the previous generation. Here a different approach is chosen. A termination threshold  $T$  that compares to the standard deviation divided by the mean of the objective function of one generation is introduced. As long as objective functions close to zero are avoided this termination criterion can be employed and is invariant to the starting conditions as well as the nature of the target function. The result of the optimization is then given by the best performing vector of the last generation.

## 5.2 Simulation

To evaluate the performance of LILDE in different situations a simulation of the optimization is carried out. The target function is given by a multimodal analytic function, the  $d$ -dimensional Ackley's function [139]. The function is parametrized according to

$$f(\vec{x}_i) = \frac{1}{0.3} \left\{ 10 \exp \left( -\frac{1}{200} \sqrt{\frac{1}{d} \sum_{j=0}^{d-1} x_i^j{}^2} \right) + \exp \left( \frac{1}{d} \sum_{j=0}^{d-1} \cos \left( \frac{\pi}{4} x_i^j \right) \right) - 9.7 \right\}, \quad (5.2)$$

where  $d$  is the number of dimensions and the parameter space  $x_i$  is ranging from -10 to 10. The function features  $3^d$  local maxima that are well separated but only 13% lower than the global optimum in the center (see Fig. 5.2).

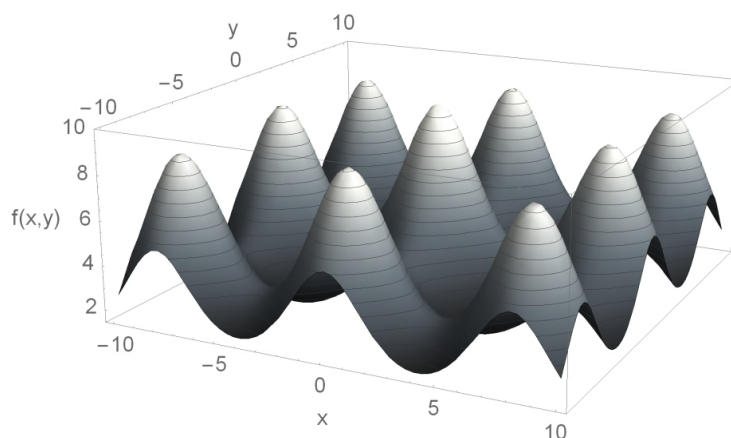


**Figure 5.2: Analytic test function in two dimensions.** Ackley's function features  $3^d$  well-separated maxima that are 13% lower than the central global optimum.

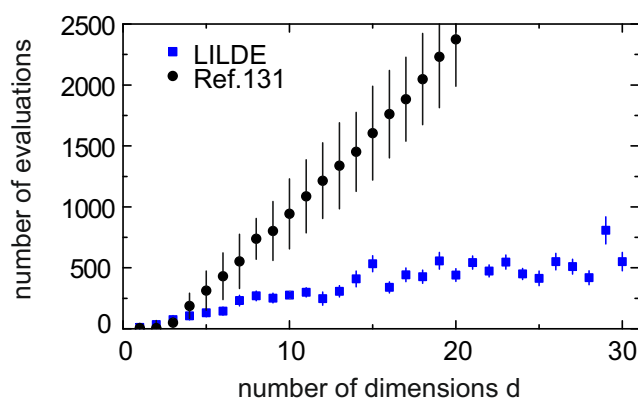


**Figure 5.3: Scaling with the number of dimensions.** The number of evaluations that is needed by the algorithm for convergence is depicted as a function of the number of dimensions. The blue squares correspond to number of evaluations needed by the LILDE algorithm and the black circles to those needed by the algorithm of Ref. [131]. Each data point is averaged over 50 runs of the simulation and the error bars indicate the standard deviation.

This test bed is used to show the number of evaluations that are necessary to find the global optimum for different number of dimensions as depicted in Fig. 5.3. This test is performed for LILDE as well as the algorithm of Ref. [131]. This algorithm constructs the vectors of the next generation by recombining two parent vectors to form two new vectors which are then also mutated. A detailed description of this algorithm can be found in Ref. [132]. The optimal number of individuals per generations ranges for both algorithms between 6 and 15. Within this range the performance is nearly independent of the exact number



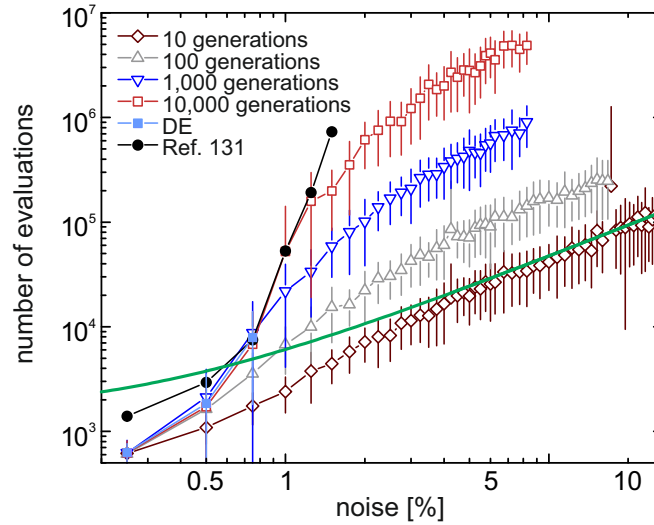


**Figure 5.4: Performance of algorithms for increasing noise on the objective function.** For increasing noise, the DE algorithm (solid light blue squares) and the algorithm of Ref. [131] quickly become inefficient. For decreasing lifetimes LILDE becomes more efficient (open symbols). For a lifetime of 10 generations and large noise, the algorithm scales linearly (green solid line) with the noise. Each data point is averaged over 50 runs and the error bars indicate the standard deviation.

of individuals. Since the global maximum is known in this case the termination criterion was based on the best individuals proximity to it. All parameters of the best performing individual have to be within a 5% range of the ideal optimum. This excludes premature convergence to a local optimum. Each optimization was run 50 times and the data point denotes its average with the error bars indicating the standard deviation. Both algorithms show a linear scaling with increasing number of dimensions. While Ref. [131] slightly outperforms LILDE for up to three dimensions, LILDE performs over a factor 5 better for higher dimensions.

Previous efforts to extend DE to noisy environments are mainly restricted to resampling each trial vector multiple times and averaging over the outcomes, which leads to a quadratic increase of the optimization time [140, 141]. To evaluate the performance of LILDE in a noisy experimental environment, shot-to-shot Gaussian noise is added to Ackley's function in ten dimensions. The standard deviation of the corresponding function value is increased from 0% to 25% percent and the number of evaluations needed for the optimization is recorded. (see Fig. 5.4). If an algorithm needs more than 7.5 million evaluations before convergence, the optimization is regarded as failed. As soon as one of the 50 runs that are carried out for each data point fails, the whole data point

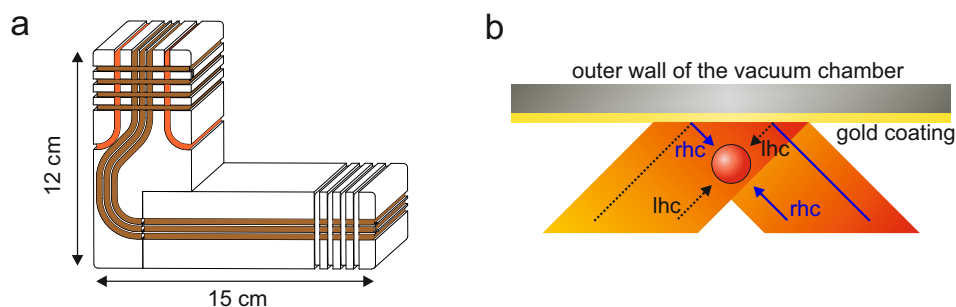


**Figure 5.5: Sketch of the magnetic field generating wire structure used in the optimization.** **a** A copper wire structure is mounted onto a water-cooled copper base structure. The current conducting wires generate all magnetic fields needed for the experiments. The nine wires used in the 21-dimensional optimization are depicted in orange and are supplied by eight different currents. The two light orange wires carry the same current, while all other wires are individually addressed. **b** A thin, gold coated steel foil separates the wire structure from the vacuum. The magnetic fields from the current conducting wires form a minimum below this steel foil. The gold coating is used to realize a mirror MOT configuration with two light beams that are reflected in a  $45^\circ$  angle on the surface. The confinement in the third direction is realized by a third beam reflected on a mirror inside the vacuum. The right hand circular polarized light (rhc) is indicated as solid blue arrows, while the left hand circular polarized light (lhc) is indicate in dashed black.

is regarded as failed. For DE (light blue solid squares) this is the case for 0.75% Gaussian noise, while Ref. [131] (black solid circles) is able to cope with up to 1.5% noise. LILDE however is able to find the optimum also for noisy environments. Already a life time of 10,000 generations (red open squares) enables convergence for over 8% noise. While shorter lifetimes increase the effort for remeasurement, they drastically improve the overall performance (open symbols). The best performance is found for a lifetime of 10 generations (dark red open diamonds), where the remeasurement effort amounts to 10% of the measurements. For large noise, the increase of effort scales linearly (green solid line). Thereby, LILDE scales better than the quadratically scaling approaches in literature.

### 5.3 Experimental application

The optimization is carried out in an experimental system with many independently addressable parameters. The number of  $^{87}\text{Rb}$  atoms trapped in a magnetic quadrupole trap is used as the target function to optimize the output of this source of ultracold atoms. A precooled atomic beam from a two-dimensional magneto-optical trap (MOT) is used to load a three-dimensional MOT, which is set up in

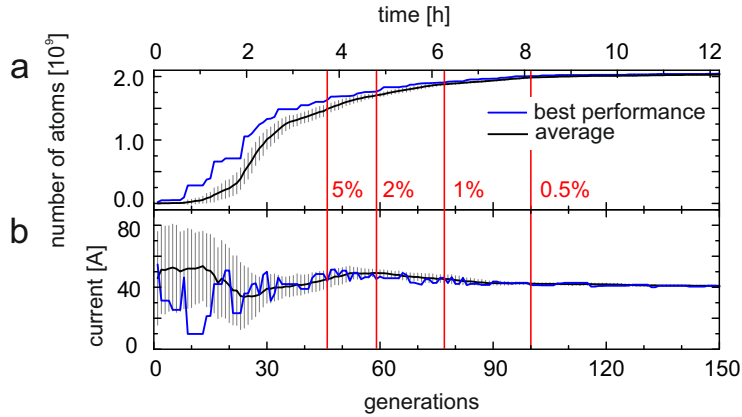


**Figure 5.6: Experimental optimization in 21 dimensions.** The experiment is optimized on a 21-dimensional parameter space, that is composed of currents and laser frequencies. The population size for this optimization was set to  $N = 4 \cdot d = 84$ . The vertical lines indicate different termination criteria. The 0.5%-termination criterion is met after 100 generations corresponding to  $\sim 8$  hours of optimization. The blue line denotes the best performing vector, while the black line denotes the average, where the error bars indicate the standard deviation of each generation. **a** The objective function is defined by the number of atoms in the final trap. **b** The evolution of one of the optimization parameters, a current, is shown as a function of the generations.

a mirror MOT configuration. All magnetic fields for this MOT are supplied by nine current carrying wires with eight different currents as shown in Fig. 5.5. The wire structure is separated from the vacuum by a thin steel foil which is gold coated on the inside of the vacuum to serve as a retro-reflective mirror for two MOT beams coming in under a  $45^\circ$  angle. The confinement in the third direction is realized by a third beam perpendicular to the two other beams. This beam is retro-reflected by a mirror inside the vacuum chamber which also has a  $\lambda/4$  retardation coating. The atoms are further cooled in an optical molasses before they undergo optical pumping to a magnetically trappable spin state and are then transferred to a magnetic quadrupole trap. Like all magnetic fields in this experiment the trap is also provided by the wire structure, which is constructed of millimeter-scale wires and acts as a mesoscopic atom chip. The detuning of the red-detuned MOT beams is adjustable, such that the beams are also used for the optical molasses. A separate beam is used for the optical pumping. For a detailed description of the experiment please refer to Refs. [142, 143].

The optimization of the source can be divided into two independent optimization procedures. In the first step the nine parameters involved in the MOT are optimized. Eight parameters control the nine wires that provide the magnetic field, with two of these wires connected in series. The ninth parameter is

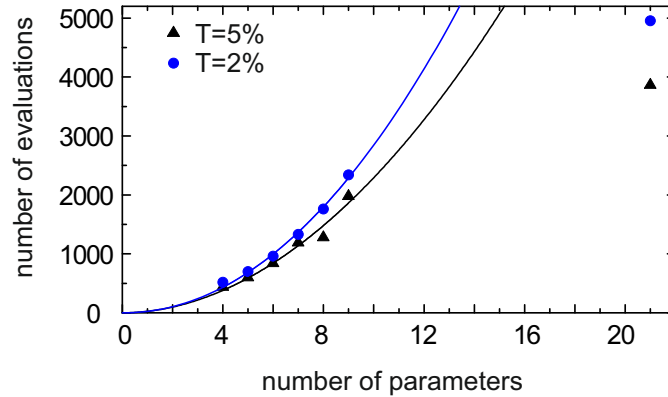


**Figure 5.7: Scaling of the experimental optimization with the number of parameters.** The number of evaluations that are necessary for the optimization is shown as a function of the number of parameters. The black triangles correspond to the 5% termination criterion, while the blue circles correspond to 2%. The lines are quadratic fits to the data for up to 9 parameters. The number of evaluations needed in the 21-dimensional optimization falls below this quadratic scaling, since a smaller number of vector  $N$  per generation is used.

given by the detuning of the MOT beams. The second step involves 21 experimental parameters. This optimization consists of different experimental parts that are correlated via the position and shape of the atomic cloud after each part. After the MOT is loaded the atoms are first pulled closer towards the chip by dynamically adjusting eight currents and the detuning of the MOT beams, amounting to a total of nine parameters. The subsequent optical molasses is a two stage process. First, the MOT laser detuning is ramped linearly from a first to a second frequency. Afterwards, it is fixed to a third value, amounting to a total of three parameters for this part. During the optical pumping two currents provide an approximately homogeneous field. The final trap consists of seven different currents. All this amounts to 21 correlated parameters that need to be optimized.

The LILDE algorithm is implemented into the experiment control in LabVIEW. The software controls the complete experimental cycle including all mentioned parameters and their timings. This is realized by a real-time capable control that utilizes a field-programmable gate array to output all digital channels directly and all analogue channels via digital-to-analog converters [144]. The number of atoms is evaluated on a separate system using fluorescence imaging on a CCD camera. This information is then read in by LabVIEW and used as the target function for the optimization. The cycling time for the 21 dimensional optimization is 3.5 s.

Fig. 5.6 shows the performance of the optimization as a function of the number of generations. The number of atoms rises as the optimization continues,

with the best performing target vector clearly outperforming the average in the beginning but approaching the common optimum for longer times. The evolution of one current is shown exemplarily. The red vertical lines indicate the different termination thresholds  $T$  at 5%, 2%, 1% and 0.5%. To reach the 0.5% threshold an optimization time of 8 h 10 min is needed.

The scaling of the needed evaluations for different numbers of parameters can also be regarded in the experimental case as shown in Fig. 5.7. It includes the two described sets of 9 and 21 parameters as well as subsets of the 9 parameter case. Each set is evaluated with respect to both the 5% as well as the 2% termination criterion. The 2% threshold results in an optimization time of 2 h 45 min for the 9-dimensional set and 5 h 45 min for the 21-dimensional set. All optimizations are performed with the DE constants set to  $F = 0.9$ ,  $CR = 0.9$  and  $E = 0.5$ . The number of vectors per generation is set to  $N = d \cdot 10$  for  $d \leq 9$ . These values are adopted from literature [135]. For larger dimensional parameter spaces less vectors per dimension are needed. The 21-dimensional set is optimized with  $N = d \cdot 4 = 84$ , which minimizes the evaluation effort while maintaining a high convergence rate. While the effort for the lower dimensional parameter spaces increases quadratically as shown by the fits in Fig. 5.7, this scaling can thus be beaten in higher dimensional cases.



---

## OUTLOOK

This thesis has presented the realization of two experiments enabled by spin-dynamics induced entanglement. The first experiment showed EPR entanglement in an atomic system. The relevant noise sources from the experiment as well as strategies to further suppress them are discussed in the first part of this outlook. The second experiment demonstrated the application of a squeezed atomic vacuum state to enhance the performance of an interferometer. Further investigations that can be implemented in the current experimental setup are presented in the following sections of this outlook.

### Technical improvements

As discussed in chapter 3, the measurements of EPR entanglement suffer from two main noise sources. Firstly, the radio-frequency intensity noise of 0.4% induces a fluctuation of the corresponding Rabi-frequencies, leading to an increased noise in the quadrature sum. The frequency generator (MARCONI 2025) that provides the radio-frequency is specified with an intensity drift of  $\pm 0.04\%K^{-1}$ . Considering a maximal temperature oscillation of 2 K in the laboratory, this can not fully explain the intensity noise. One possible explanation is the temperature dependence of the following components in the frequency chain, which includes switches, the amplifier and the antenna. The easiest way to reduce the intensity noise without changing the components of the frequency chain would be to monitor and stabilize the intensity directly during the experimental sequence. However, the short pulse duration of 30  $\mu s$ , which leads to only 55 oscillations of the radio-frequency field, makes the compensation of fast fluctuations challenging. Assuming only slow drifts in comparison to the cycling time, like those induced by temperature oscillations in the laboratory, the intensity can be monitored by a longer pulse during the MOT-loading phase

of the experiment. This monitoring result can then either be used to adjust the intensity of the following pulse or to post-correct the data.

The second noise source in the EPR experiments, the phase noise of the local oscillator, could stem from different effects. The first effect is magnetic field noise, which we measure to be  $90 \mu\text{G}$  shot-to-shot. Magnetic field fluctuations lead to a shift in the energy of the  $|1, \pm 1\rangle$  states due to the Zeeman shift. While the linear shift is not important here, the quadratic Zeeman shift leads to a change in phase evolution. The magnetic field noise can be controlled by better monitoring and active stabilization of the magnetic field, which is currently being implemented. A similar effect stems from microwave intensity noise in the dressing field. Here the monitoring and active stabilization could also be improved. A second effect is caused by a magnetic field gradient over the size of the ensembles, which leads to a blurring of the phase. The main effect on the phase will be caused in the direction of the magnetic offset field. The gradient can be measured in a Ramsey-type experiment, where the atoms are loaded into an elongated dipole trap. For a homogeneous magnetic field, the spatial distribution of the fraction of atoms in the involved states would be homogeneous. In the case of a gradient, the spatial distribution would lead to an inhomogeneous phase evolution and thus to a spatial dependence of the transferred fraction. A similar effect stems from density dependent shifts, which are in our case correlated with the total atom number. Several approaches can be taken to suppress this noise contribution. The stability of the total number of atoms could be improved, the total number of atoms could be postselected, or the density shift could be postcorrected. The last contribution to phase noise is the finite temperature of the local oscillator ensemble in  $m_F = 0$ . It has recently been shown, that ultra-low temperatures in BECs can be measured in a single shot measurement with high precision [145]. While this technique could be used to evaluate the temperatures in our system, further investigation on the role of finite temperature effects in the phase evolution are needed.

### **Multipartite steering via programmable quantum networks**

It has recently been shown [146] that multipartite EPR steering can be realized artificially by a programmable linear optics circuit [147]. A photodiode array consisting of eight segments is used to measure an input basis of eight modes. The basis consists of two perpendicular quadrature modes and six perpendicular vacuum modes. These eight modes can now be coupled in an emulated programmable linear optics circuit. It can emulate beam splitters as well as  $\pi$  phase shifts by applying an electronic gain to each part of the input array via a unitary matrix.

This approach can be translated to our system. The easiest case is that of one-way steering as described in chapter 3. In the experiment, one mode of the



EPR entangled state is coupled with a vacuum mode. The result is detected in the form of atom number counting in the absorption image on a CCD camera. Artificially, the coupling to the vacuum mode could be achieved by performing a standard two-way steered EPR measurement (see chapter 3) and restricting the region of interest on one of the two output modes such, that it is only taken into account partially. By varying the size of the region of interest, this emulates the action of a beam splitter with a variable vacuum port. This would allow to explore the regime of one-way steering.

Due to the nature of our detection with a CCD camera, more complex geometries for a programmable optics circuit are imaginable. This opens the path to further investigate multipartite entanglement in our system.

### The Hong-Ou-Mandel effect

The Hong-Ou-Mandel (HOM) effect is another example of a counterintuitive effect in quantum mechanics. Published in 1987, it shows that the simultaneous input of one photon at each port of a symmetric beam splitter gives an asymmetric result [148]. The photons are both found in either of the output ports but never one photon in each port. After a proposal for a HOM experiment with ballistic atom pairs in 2014 [149], the first atomic realization has been presented in Ref. [150]. While they show a significant drop in the correlation function of their two output ports for simultaneous detection, they were not able to show a complete suppression of symmetric events. A more generalized HOM effect arises when a Fock state of  $n$  particles enters each input port of the beam splitter. This results in  $n$  possible outcomes, namely those with even particle number in the output ports. This has been shown for two particles per input mode in optics [151].

In our atomic system, such a measurement of the HOM and the generalized HOM effect could be realized. The input states for the beam splitter are prepared via spin-changing collisions, creating a two-mode squeezed state in  $m_F = \pm 1$ . These two modes are then coupled via a two-photon transition involving the  $|2, 0\rangle$  state. This acts as the beam splitter while leaving the condensate in  $|1, 0\rangle$  intact. Due to the generalized HOM effect one now expects an even number of atoms in both  $m_F = \pm 1$  states. To analyze this, a homodyne detection is performed whose outputs are used to perform a full state reconstruction, where the suppression of odd number particle states should become evident.

### Bell tests utilizing two-mode squeezed vacuum states

In their seminal papers, Bell [81] and later Clauser, Horne, Shimony and Holt (CHSH) [82] showed, that a local hidden variable theory, as hinted at by EPR, cannot unify quantum mechanics with the notion of local reality. They derived

constrains, referred to as Bell's or CHSH inequalities, whose violation negates the existence of a local hidden variable theory. These so called Bell tests are typically formulated for discrete variables like spin-1/2 systems.

In contrast, Refs. [152–154] propose a continuous variable Bell test based on the linear optical displacement operator, that can be used to violate a CHSH inequality. The test utilizes a two-mode squeezed vacuum state that is measured with a variable displacement, realized by unbalanced homodyning with a coherent local oscillator state. Both involved states are weakly populated with average photon numbers below one. The result, either one photon or no photons, is then recorded on a click detector. The setup is robust to losses. The total transmission efficiency, including losses during the displacement as well as the detection efficiency, can be as low as 66.7%.

Our atomic system is ideal to adopt this scheme, since two of the prerequisites of the measurement have already been used successfully in other contexts in our experimental setup. The displacement operator was implemented in Ref. [155] to show an interaction-free measurement implemented via quantum Zeno stabilization. The two-mode squeezed vacuum state has been discussed in the previous chapters of this work. It would therefore be possible to implement such a Bell test in the current system. One would create a squeezed vacuum state in  $|1, \pm 1\rangle$  via spin-changing collisions, before applying a weak homodyning with the remaining condensate in  $|1, 0\rangle$ . A single atom detection could be implemented using a fluorescence detection. Two counter-propagating beams in the vertical direction form a one-dimensional optical molasses. The molasses would be aligned with the splitting of the atomic states. This ensures a longer interrogation time than a standard one beam detection. The fluorescence is then recorded in the perpendicular direction. Such a setup allows for the first Bell test of quantum mechanics with a continuous variable state.

# Bibliography

- [1] C. S. Wu and I. Shakhov, *The angular correlation of scattered annihilation radiation*, Phys. Rev., 1950, DOI: 10.1103/PhysRev.77.136.
- [2] M. A. Finger, T. S. Iskhakov, N. Y. Joly, M. V. Chekhova, and P. S. J. Russell, *Raman-free, noble-gas-filled photonic-crystal fiber source for ultrafast, very bright twin-beam squeezed vacuum*, Phys. Rev. Lett., 2015, DOI: 10.1103/PhysRevLett.115.143602.
- [3] X.-C. Yao, T.-X. Wang, P. Xu, H. Lu, G.-S. Pan, X.-H. Bao, C.-Z. Peng, C.-Y. Lu, Y.-A. Chen, and J.-W. Pan, *Observation of eight-photon entanglement*, Nature Photon., 2012, DOI: 10.1038/nphoton.2011.354.
- [4] L. DiCarlo, M. D. Reed, L. Sun, B. R. Johnson, J. M. Chow, J. M. Gambetta, L. Frunzio, S. M. Girvin, M. H. Devoret, and R. J. Schoelkopf, *Preparation and measurement of three-qubit entanglement in a superconducting circuit*, Nature, 2010, DOI: 10.1038/nature09416.
- [5] P. Neumann, N. Mizuochi, F. Rempp, P. Hemmer, H. Watanabe, S. Yamasaki, V. Jacques, T. Gaebel, F. Jelezko, and J. Wrachtrup, *Multipartite entanglement among single spins in diamond*, Science, 320, 2008, DOI: 10.1126/science.1157233.
- [6] T. Monz, P. Schindler, J. T. Barreiro, M. Chwalla, D. Nigg, W. A. Coish, M. Harlander, W. Hänsel, M. Hennrich, and R. Blatt, *14-qubit entanglement: Creation and coherence*, Phys. Rev. Lett., 2011, DOI: 10.1103/PhysRevLett.106.130506.
- [7] B. Julsgaard, A. Kozhekin, and E. S. Polzik, *Experimental long-lived entanglement of two macroscopic objects*, Nature, 2001, DOI: 10.1038/35096524.
- [8] M. H. Schleier-Smith, I. D. Leroux, and V. Vuletić, *States of an ensemble of two-level atoms with reduced quantum uncertainty*, Phys. Rev. Lett., 2010, DOI: 10.1103/PhysRevLett.104.073604.
- [9] R. McConnell, H. Zhang, J. Hu, S. Čuk, and V. Vuletić, *Entanglement with negative Wigner function of almost 3,000 atoms heralded by one photon*, Nature, 519, 2015, DOI: 10.1038/nature14293.

- 
- [10] M. Kitagawa and M. Ueda, *Squeezed spin states*, Phys. Rev. A, 1993, DOI: 10.1103/PhysRevA.47.5138.
- [11] C. Gross, T. Zibold, E. Nicklas, J. Estève, and M. K. Oberthaler, *Non-linear atom interferometer surpasses classical precision limit*, Nature, 2010, DOI: 10.1038/nature08919.
- [12] P. Boehi, M. F. Riedel, J. Hoffrogge, J. Reichel, T. W. Haensch, and P. Treutlein, *Coherent manipulation of Bose-Einstein condensates with state-dependent microwave potentials on an atom chip*, Nat. Phys., 2009, DOI: 10.1038/nphys1329.
- [13] C. Klempt, O. Topic, G. Gebreyesus, M. Scherer, T. Henninger, P. Hyllus, W. Ertmer, L. Santos, and J. J. Arlt, *Parametric amplification of vacuum fluctuations in a spinor condensate*, Phys. Rev. Lett., 2010, DOI: 10.1103/PhysRevLett.104.195303.
- [14] S. R. Leslie, J. Guzman, M. Vengalattore, J. D. Sau, M. L. Cohen, and D. M. Stamper-Kurn, *Amplification of fluctuations in a spinor Bose-Einstein condensate*, Phys. Rev. A, 79, 2009, DOI: 10.1103/PhysRevA.79.043631.
- [15] C. Gross, H. Strobel, E. Nicklas, T. Zibold, N. Bar-Gill, G. Kurizki, and M. K. Oberthaler, *Atomic homodyne detection of continuous-variable entangled twin-atom states*, Nature, 2011, DOI: 10.1038/nature10654.
- [16] C. D. Hamley, C. S. Gerving, T. M. Hoang, E. M. Bookjans, and M. S. Chapman, *Spin-nematic squeezed vacuum in a quantum gas*, Nature Phys., 2012, DOI: 10.1038/nphys2245.
- [17] A. Einstein, B. Podolsky, and N. Rosen, *Can quantum-mechanical description of physical reality be considered complete?*, Phys. Rev., 1935, DOI: 10.1103/PhysRev.47.777.
- [18] E. Schrödinger, *Discussion of probability relations between separated systems*, Math. Proc. Cambridge, 1935, DOI: 10.1017/S0305004100013554.
- [19] E. Schrödinger, *Die gegenwärtige Situation in der Quantenmechanik*, Die Naturwissenschaften, 1935, DOI: 10.1007/BF01491891.
- [20] Z. Y. Ou, S. F. Pereira, H. J. Kimble, and K. C. Peng, *Realization of the Einstein-Podolsky-Rosen paradox for continuous variables*, Phys. Rev. Lett., 1992, DOI: 10.1103/PhysRevLett.68.3663.
- [21] P.-A. Moreau, F. Devaux, and E. Lantz, *Einstein-Podolsky-Rosen paradox in twin images*, Phys. Rev. Lett., 2014, DOI: 10.1103/PhysRevLett.113.160401.
- [22] W. H. Furry, *Note on the quantum-mechanical theory of measurement*, Phys. Rev., 1936, DOI: 10.1103/PhysRev.49.393.

- [23] M. D. Reid, *Demonstration of the Einstein-Podolsky-Rosen paradox using non-degenerate parametric amplification*, Phys. Rev. A, 1989, DOI: 10.1103/PhysRevA.40.913.
- [24] W. Wasilewski, K. Jensen, H. Krauter, J. J. Renema, M. V. Balabas, and E. S. Polzik, *Quantum noise limited and entanglement-assisted magnetometry*, Phys. Rev. Lett., 2010, DOI: 10.1103/PhysRevLett.104.133601.
- [25] V. Händchen, T. Eberle, S. Steinlechner, A. Samblowski, T. Franz, R. F. Werner, and R. Schnabel, *Observation of one-way Einstein-Podolsky-Rosen steering*, Nature Photonics, 6, 2012, DOI: 10.1038/nphoton.2012.202.
- [26] B. Lücke, M. Scherer, J. Kruse, L. Pezzé, F. Deuretzbacher, P. Hyllus, O. Topic, J. Peise, W. Ertmer, J. Arlt, L. Santos, A. Smerzi, and C. Klempt, *Twin matter waves for interferometry beyond the classical limit*, Science, 2011, DOI: 10.1126/science.1208798.
- [27] J. Appel, P. J. Windpassinger, D. Oblak, U. B. Hoff, N. Kærgaard, and E. S. Polzik, *Mesoscopic atomic entanglement for precision measurements beyond the standard quantum limit*, Proc. Natl. Acad. Sci. U. S. A., 106, 2009, DOI: 10.1073/pnas.0901550106.
- [28] M. Riedel, P. Böhi, Y. Li, T. Hänsch, A. Sinatra, and P. Treutlein, *Atom-chip-based generation of entanglement for quantum metrology*, Nature, 2010, DOI: 10.1038/nature08988.
- [29] R. J. Sewell, M. Koschorreck, M. Napolitano, B. Dubost, N. Behbood, and M. W. Mitchell, *Magnetic sensitivity beyond the projection noise limit by spin squeezing*, Phys. Rev. Lett., 2012, DOI: 10.1103/PhysRevLett.109.253605.
- [30] W. Muessel, H. Strobel, D. Linnemann, D. B. Hume, and M. K. Oberthaler, *Scalable spin squeezing for quantum-enhanced magnetometry with Bose-Einstein condensates*, Phys. Rev. Lett., 2014, DOI: 10.1103/PhysRevLett.113.103004.
- [31] J. A. Jones, S. D. Karlen, J. Fitzsimons, A. Ardavan, S. C. Benjamin, G. A. D. Briggs, and J. J. L. Morton, *Magnetic field sensing beyond the standard quantum limit using 10-spin NOON states*, Science, 324, 2009, DOI: 10.1126/science.1170730.
- [32] C. F. Ockeloen, R. Schmied, M. F. Riedel, and P. Treutlein, *Quantum metrology with a scanning probe atom interferometer*, Phys. Rev. Lett., 2013, DOI: 10.1103/PhysRevLett.111.143001.
- [33] A. Louchet-Chauvet, J. Appel, J. J. Renema, D. Oblak, N. Kjaergaard, and E. S. Polzik, *Entanglement-assisted atomic clock beyond the projection noise limit*, New Journal of Physics, 12, 2010, DOI: 10.1088/1367-2630/12/6/065032.

- 
- [34] I. D. Leroux, M. H. Schleier-Smith, and V. Vuletić, *Orientation-dependent entanglement lifetime in a squeezed atomic clock*, Phys. Rev. Lett., 2010, DOI: 10.1103/PhysRevLett.104.250801.
- [35] V. Meyer, M. A. Rowe, D. Kielpinski, C. A. Sackett, W. M. Itano, C. Monroe, and D. J. Wineland, *Experimental demonstration of entanglement-enhanced rotation angle estimation using trapped ions*, Phys. Rev. Lett., 2001, DOI: 10.1103/PhysRevLett.86.5870.
- [36] C. M. Caves, *Quantum-mechanical noise in an interferometer*, Phys. Rev. D, 1981, DOI: 10.1103/PhysRevD.23.1693.
- [37] LIGO Scientific Collaboration, *A gravitational wave observatory operating beyond the quantum shot-noise limit*, Nature Physics, 7, 2011, DOI: 10.1038/nphys2083.
- [38] R. Horodecki, P. Horodecki, M. Horodecki, and K. Horodecki, *Quantum entanglement*, Rev. Mod. Phys., 2009, DOI: 10.1103/RevModPhys.81.865.
- [39] F. Bloch, *Nuclear induction*, Phys. Rev., 70, 1946, DOI: 10.1103/PhysRev.70.460.
- [40] R. P. Feynman, F. L. Vernon, and R. W. Hellwarth, *Geometrical representation of the Schrödinger equation for solving maser problems*, J. Appl. Phys., 28, 1957, DOI: 10.1063/1.1722572.
- [41] R. H. Dicke, *Coherence in spontaneous radiation processes*, Phys. Rev., 1954, DOI: 10.1103/PhysRev.93.99.
- [42] J. K. Stockton, J. M. Geremia, A. C. Doherty, and H. Mabuchi, *Characterizing the entanglement of symmetric many-particle spin-1/2 systems*, Phys. Rev. A, 2003, DOI: 10.1103/PhysRevA.67.022112.
- [43] M. Bourennane, M. Eibl, S. Gaertner, N. Kiesel, C. Kurtsiefer, and H. Weinfurter, *Entanglement persistency of multiphoton entangled states*, Phys. Rev. Lett., 2006, DOI: 10.1103/PhysRevLett.96.100502.
- [44] R. Prevedel, G. Cronenberg, M. S. Tame, M. Paternostro, P. Walther, M. S. Kim, and A. Zeilinger, *Experimental realization of Dicke states of up to six qubits for multiparty quantum networking*, Phys. Rev. Lett., 2009, DOI: 10.1103/PhysRevLett.103.020503.
- [45] W. Wieczorek, R. Krischek, N. Kiesel, P. Michelberger, G. Tóth, and H. Weinfurter, *Experimental entanglement of a six-photon symmetric Dicke state*, Phys. Rev. Lett., 2009, DOI: 10.1103/PhysRevLett.103.020504.
- [46] H. Häffner, W. Hänsel, C. F. Roos, J. Benhelm, D. Chek-al kar, M. Chwalla, T. Körber, U. D. Rapol, M. Riebe, P. O. Schmidt, C. Becher, O. Gühne,

- W. Dür, and R. Blatt, *Scalable multiparticle entanglement of trapped ions*, Nature, 2005, DOI: 10.1038/nature04279.
- [47] F. Haas, J. Volz, R. Gehr, J. Reichel, and J. Estève, *Entangled states of more than 40 atoms in an optical fiber cavity*, Science, 344, 2014, DOI: 10.1126/science.1248905.
- [48] G. Barontini, L. Hohmann, F. Haas, J. Estève, and J. Reichel, *Deterministic generation of multiparticle entanglement by quantum Zeno dynamics*, Science, 349, 2015, DOI: 10.1126/science.aaa0754.
- [49] B. Lücke, J. Peise, G. Vitagliano, J. Arlt, L. Santos, G. Tóth, and C. Klempt, *Detecting multiparticle entanglement of Dicke states*, Phys. Rev. Lett., 2014, DOI: 10.1103/PhysRevLett.112.155304.
- [50] D. J. Wineland, J. J. Bollinger, W. M. Itano, F. L. Moore, and D. J. Heinzen, *Spin squeezing and reduced quantum noise in spectroscopy*, Phys. Rev. A, 1992, DOI: 10.1103/PhysRevA.46.R6797.
- [51] J. Ma, X. Wang, C. Sun, and F. Nori, *Quantum spin squeezing*, Phys. Rep., 509, 2011, DOI: 10.1016/j.physrep.2011.08.003.
- [52] A. Sørensen, L.-M. Duan, J. I. Cirac, and P. Zoller, *Many-particle entanglement with Bose-Einstein condensates*, Nature, 2001, DOI: 10.1038/35051038.
- [53] S. Raghavan, H. Pu, P. Meystre, and N. Bigelow, *Generation of arbitrary Dicke states in spinor Bose-Einstein condensates*, Optics Communications, 188, 2001, DOI: 10.1016/S0030-4018(00)01163-9.
- [54] G. Tóth, C. Knapp, O. Gühne, and H. Briegel, *Optimal spin squeezing inequalities detect bound entanglement in spin models*, Phys. Rev. Lett., 2007, DOI: 10.1103/PhysRevLett.99.250405.
- [55] L. Pezzé and A. Smerzi, *Entanglement, nonlinear dynamics and the Heisenberg limit*, Phys. Rev. Lett., 2009, DOI: 10.1103/PhysRevLett.102.100401.
- [56] R. A. Fisher, *Theory of statistical estimation*, In *Mathematical Proceedings of the Cambridge Philosophical Society*, volume 22, pages 700–725. Cambridge Univ Press, 1925.
- [57] S. L. Braunstein and C. M. Caves, *Statistical distance and the geometry of quantum states*, Phys. Rev. Lett., 1994, DOI: 10.1103/PhysRevLett.72.3439.
- [58] P. Hyllus, L. Pezzé, and A. Smerzi, *Entanglement and sensitivity in precision measurements with states of a fluctuating number of particles*, Phys. Rev. Lett., 2010, DOI: 10.1103/PhysRevLett.105.120501.

- [59] H. Strobel, W. Muessel, D. Linnemann, T. Zibold, D. B. Hume, L. Pezzè, A. Smerzi, and M. K. Oberthaler, *Fisher information and entanglement of non-Gaussian spin states*, *Science*, 345, 2014, DOI: 10.1126/science.1250147.
- [60] A. Kuzmich, L. Mandel, and N. Bigelow, *Generation of spin squeezing via continuous quantum nondemolition measurement*, *Physical Review Letters*, 85, 2000, DOI: 10.1103/PhysRevLett.85.1594.
- [61] J. G. Bohnet, K. C. Cox, M. A. Norcia, J. M. Weiner, Z. Chen, and J. K. Thompson, *Reduced spin measurement back-action for a phase sensitivity ten times beyond the standard quantum limit*, *Nature Photonics*, 8, 2014, DOI: 10.1038/nphoton.2014.151.
- [62] M. J. Steel and M. J. Collett, *Quantum state of two trapped Bose-Einstein condensates with a Josephson coupling*, *Phys. Rev. A*, 1998, DOI: 10.1103/PhysRevA.57.2920.
- [63] D. W. Berry and B. C. Sanders, *Equivalence between two-mode spin squeezed states and pure entangled states with equal spin*, *Journal of Physics A: Mathematical and General*, 38, 2005, DOI: 10.1088/0305-4470/38/14/L01.
- [64] M. Scherer, B. Lücke, G. Gebreyesus, O. Topic, F. Deuretzbacher, W. Ertmer, L. Santos, J. J. Arlt, and C. Klempt, *Spontaneous breaking of spatial and spin symmetry in spinor condensates*, *Phys. Rev. Lett.*, 2010, DOI: 10.1103/PhysRevLett.105.135302.
- [65] J.-W. Pan, Z.-B. Chen, C.-Y. Lu, H. Weinfurter, A. Zeilinger, and M. Żukowski, *Multiphoton entanglement and interferometry*, *Rev. Mod. Phys.*, 2012, DOI: 10.1103/RevModPhys.84.777.
- [66] L.-A. Wu, H. J. Kimble, J. L. Hall, and H. Wu, *Generation of squeezed states by parametric down conversion*, *Phys. Rev. Lett.*, 1986, DOI: 10.1103/PhysRevLett.57.2520.
- [67] H. Schmaljohann, M. Erhard, J. Kronjäger, K. Sengstock, and K. Bongs, *Dynamics and thermodynamics in spinor quantum gases*, *Appl. Phys. B*, 2004, DOI: 10.1007/s00340-004-1664-6.
- [68] M. Scherer, *Nichtklassische Zustände in Spinor-Bose-Einstein-Kondensaten*, PhD thesis, Leibniz Universität Hannover, 2012.
- [69] C. Klempt, T. van Zoest, T. Henninger, O. Topic, E. Rasel, W. Ertmer, and J. Arlt, *Ultraviolet light-induced atom desorption for large rubidium and potassium magneto-optical traps*, *Phys. Rev. A*, 73, 2006, DOI: 10.1103/PhysRevA.73.013410.



- 
- [70] Y.-J. Lin, A. R. Perry, R. L. Compton, I. B. Spielman, and J. V. Porto, *Rapid production of  $^{87}\text{Rb}$  Bose-Einstein condensates in a combined magnetic and optical potential*, Phys. Rev. A, 2009, DOI: 10.1103/PhysRevA.79.063631.
- [71] W. Ketterle and N. V. Druten, Evaporative cooling of trapped atoms, In B. Bederson and H. Walther, editors, *Advances In Atomic, Molecular, and Optical Physics*, volume 37 of *Advances In Atomic, Molecular, and Optical Physics*, pages 181 – 236. Academic Press, 1996, DOI: 10.1016/S1049-250X(08)60101-9.
- [72] G. Reinaudi, T. Lahaye, Z. Wang, and D. Guéry-Odelin, *Strong saturation absorption imaging of dense clouds of ultracold atoms*, Opt. Lett., 2007, DOI: 10.1364/OL.32.003143.
- [73] B. Lücke, *Multiparticle entanglement in a spinor Bose-Einstein condensate for quantum-enhanced interferometry*, PhD thesis, Leibniz Universität Hannover, 2014.
- [74] F. Deuretzbacher, G. Gebreyesus, O. Topic, M. Scherer, B. Lücke, W. Ertmer, J. Arlt, C. Klempt, and L. Santos, *Parametric amplification of matter waves in dipolar spinor Bose-Einstein condensates*, Phys. Rev. A, 2010, DOI: 10.1103/PhysRevA.82.053608.
- [75] J. Kronjäger, C. Becker, P. Navez, K. Bongs, and K. Sengstock, *Magnetically tuned spin dynamics resonance*, Phys. Rev. Lett., 97, 2006, DOI: 10.1103/PhysRevLett.97.110404.
- [76] C. C. Gerry and P. Knight, *Introductory quantum optics*. Cambridge University Press, 2005.
- [77] C. K. Law, H. Pu, and N. P. Bigelow, *Quantum spins mixing in spinor Bose-Einstein condensates*, Phys. Rev. Lett., 1998, DOI: 10.1103/PhysRevLett.81.5257.
- [78] C. Klempt, O. Topic, G. Gebreyesus, M. Scherer, T. Henninger, P. Hyllus, W. Ertmer, L. Santos, and J. J. Arlt, *Multiresonant spinor dynamics in a Bose-Einstein condensate*, Phys. Rev. Lett., 2009, DOI: 10.1103/PhysRevLett.103.195302.
- [79] J. Peise, I. Kruse, K. Lange, B. Lücke, L. Pezzè, J. Arlt, W. Ertmer, K. Hammerer, L. Santos, A. Smerzi, and C. Klempt, *Satisfying the Einstein-Podolsky-Rosen criterion with massive particles*, Nat. Commun., 6, 2015, DOI: 10.1038/ncomms9984.
- [80] N. Bohr, *Can quantum-mechanical description of physical reality be considered complete?*, Phys. Rev., 1935, DOI: 10.1103/PhysRev.48.696.
- [81] J. S. Bell, *On the Einstein-Podolsky-Rosen paradox*, Physics, 1, 1964.

- 
- [82] J. F. Clauser, M. A. Horne, A. Shimony, and R. A. Holt, *Proposed experiment to test local hidden-variable theories*, Phys. Rev. Lett., 1969, DOI: 10.1103/PhysRevLett.23.880.
- [83] S. J. Freedman and J. F. Clauser, *Experimental test of local hidden-variable theories*, Phys. Rev. Lett., 1972, DOI: 10.1103/PhysRevLett.28.938.
- [84] M. A. Rowe, D. Kielpinski, V. Meyer, C. A. Sackett, W. M. Itano, C. Monroe, and D. J. Wineland, *Experimental violation of a Bell's inequality with efficient detection*, Nature, 2001, DOI: 10.1038/35057215.
- [85] N. Brunner, D. Cavalcanti, S. Pironio, V. Scarani, and S. Wehner, *Bell nonlocality*, Rev. Mod. Phys., 2014, DOI: 10.1103/RevModPhys.86.419.
- [86] J. C. Howell, R. S. Bennink, S. J. Bentley, and R. W. Boyd, *Realization of the Einstein-Podolsky-Rosen paradox using momentum- and position-entangled photons from spontaneous parametric down conversion*, Phys. Rev. Lett., 2004, DOI: 10.1103/PhysRevLett.92.210403.
- [87] L.-M. Duan, A. Sørensen, J. I. Cirac, and P. Zoller, *Squeezing and entanglement of atomic beams*, Phys. Rev. Lett., 2000, DOI: 10.1103/PhysRevLett.85.3991.
- [88] R. Simon, *Peres-Horodecki separability criterion for continuous variable systems*, Phys. Rev. Lett., 2000, DOI: 10.1103/PhysRevLett.84.2726.
- [89] M. D. Reid, *Quantum cryptography with a predetermined key, using continuous-variable Einstein-Podolsky-Rosen correlations*, Phys. Rev. A, 2000, DOI: 10.1103/PhysRevA.62.062308.
- [90] C. H. Bennett, G. Brassard, C. Crépeau, R. Jozsa, A. Peres, and W. K. Wootters, *Teleporting an unknown quantum state via dual classical and Einstein-Podolsky-Rosen channels*, Phys. Rev. Lett., 1993, DOI: 10.1103/PhysRevLett.70.1895.
- [91] L. Vaidman, *Teleportation of quantum states*, Phys. Rev. A, 1994, DOI: 10.1103/PhysRevA.49.1473.
- [92] M. D. Reid, P. D. Drummond, W. P. Bowen, E. G. Cavalcanti, P. K. Lam, H. A. Bachor, U. L. Andersen, and G. Leuchs, *Colloquium : The Einstein-Podolsky-Rosen paradox: From concepts to applications*, Rev. Mod. Phys., 2009, DOI: 10.1103/RevModPhys.81.1727.
- [93] L.-M. Duan, G. Giedke, J. I. Cirac, and P. Zoller, *Inseparability criterion for continuous variable systems*, Phys. Rev. Lett., 2000, DOI: 10.1103/PhysRevLett.84.2722.

- [94] A. I. Lvovsky, Squeezed light, In D. L. Andrews, editor, *Photonics, Volume 1: Fundamentals of Photonics and Physics*, chapter 5, pages 121–164. John Wiley & Sons, 2015, DOI: 10.1002/9781119009719.ch1.
- [95] R. Schmied and P. Treutlein, *Tomographic reconstruction of the Wigner function on the Bloch sphere*, New J. Phys., 13, 2011, DOI: 10.1088/1367-2630/13/6/065019.
- [96] A. I. Lvovsky and M. G. Raymer, *Continuous-variable optical quantum-state tomography*, Rev. Mod. Phys., 2009, DOI: 10.1103/RevModPhys.81.299.
- [97] V. D’Auria, S. Fornaro, A. Porzio, S. Solimeno, S. Olivares, and M. G. A. Paris, *Full characterization of Gaussian bipartite entangled states by a single homodyne detector*, Phys. Rev. Lett., 2009, DOI: 10.1103/PhysRevLett.102.020502.
- [98] M. Vasilyev, S.-K. Choi, P. Kumar, and G. M. D’Ariano, *Tomographic measurement of joint photon statistics of the twin-beam quantum state*, Phys. Rev. Lett., 2000, DOI: 10.1103/PhysRevLett.84.2354.
- [99] Z. Hradil, J. Řeháček, J. Fiurášek, and M. Ježek, 3 maximum-likelihood methods in quantum mechanics, In M. Paris and J. Řeháček, editors, *Quantum State Estimation*, volume 649 of *Lecture Notes in Physics*, pages 59–112. Springer Berlin Heidelberg, 2004, DOI: 10.1007/978-3-540-44481-7\_3.
- [100] Z. Hradil, *Quantum-state estimation*, Physical Review A, 55, 1997, DOI: 10.1103/PhysRevA.55.R1561.
- [101] J. Řeháček, Z. Hradil, E. Knill, and A. Lvovsky, *Diluted maximum-likelihood algorithm for quantum tomography*, Physical Review A, 75, 2007, DOI: 10.1103/PhysRevA.75.042108.
- [102] E. G. Cavalcanti, S. J. Jones, H. M. Wiseman, and M. D. Reid, *Experimental criteria for steering and the Einstein-Podolsky-Rosen paradox*, Phys. Rev. A, 2009, DOI: 10.1103/PhysRevA.80.032112.
- [103] S. Weyers, V. Gerginov, N. Nemitz, R. Li, and K. Gibble, *Distributed cavity phase frequency shifts of the caesium fountain PTB-CSF2*, Metrologia, 49, 2012, DOI: 10.1088/0026-1394/49/1/012.
- [104] B. Bloom, T. Nicholson, J. Williams, S. Campbell, M. Bishof, X. Zhang, W. Zhang, S. Bromley, and J. Ye, *An optical lattice clock with accuracy and stability at the  $10^{-18}$  level*, Nature, 506, 2014, DOI: 10.1038/nature12941.
- [105] G. Santarelli, P. Laurent, P. Lemonde, A. Clairon, A. G. Mann, S. Chang, A. N. Luiten, and C. Salomon, *Quantum projection noise in an atomic fountain: A high stability cesium frequency standard*, Phys. Rev. Lett., 1999, DOI: 10.1103/PhysRevLett.82.4619.

- 
- [106] A. A. Michelson and E. W. Morley, *On the relative motion of the earth and the luminiferous ether*, American journal of science, 1887, DOI: 10.1080/14786448708628130.
- [107] J. J. Condon, W. D. Cotton, E. W. Greisen, Q. F. Yin, R. A. Perley, G. B. Taylor, and J. J. Broderick, *The NRAO VLA sky survey*, The Astronomical Journal, 115, 1998, DOI: 10.1086/300337.
- [108] J. E. Baldwin and C. A. Haniff, *The application of interferometry to optical astronomical imaging*, Philosophical Transactions of the Royal Society of London A: Mathematical, Physical and Engineering Sciences, 360, 2002, DOI: 10.1098/rsta.2001.0977.
- [109] K. U. Schreiber, T. Klügel, J.-P. R. Wells, R. B. Hurst, and A. Gebauer, *How to detect the Chandler and the annual wobble of the Earth with a large ring laser gyroscope*, Phys. Rev. Lett., 2011, DOI: 10.1103/PhysRevLett.107.173904.
- [110] D. Huang, E. A. Swanson, C. P. Lin, J. S. Schuman, W. G. Stinson, W. Chang, M. R. Hee, T. Flotte, K. Gregory, C. A. Puliafito, et al., *Optical coherence tomography*, Science, 254, 1991, DOI: 10.1126/science.1957169.
- [111] M. Kasevich and S. Chu, *Atomic interferometry using stimulated Raman transitions*, Phys. Rev. Lett., 67, 1991, DOI: 10.1103/PhysRevLett.67.181.
- [112] H. J. McGuinness, A. V. Rakholia, and G. W. Biedermann, *High data-rate atom interferometer for measuring acceleration*, Appl. Phys. Lett., 100, 2012, DOI: 10.1063/1.3673845.
- [113] A. Louchet-Chauvet, S. Merlet, Q. Bodart, A. Landragin, F. Pereira Dos Santos, H. Baumann, G. D'Agostino, and C. Origlia, *Comparison of 3 absolute gravimeters based on different methods for the e-MASS project*, IEEE T. Instr. Meas., 2011, DOI: 10.1109/TIM.2010.2099951.
- [114] D. Schlippert, J. Hartwig, H. Albers, L. L. Richardson, C. Schubert, A. Roura, W. P. Schleich, W. Ertmer, and E. M. Rasel, *Quantum test of the universality of free fall*, Phys. Rev. Lett., 112, 2014, DOI: 10.1103/PhysRevLett.112.203002.
- [115] J. B. Fixler, G. T. Foster, J. M. McGuirk, and M. A. Kasevich, *Atom interferometer measurement of the Newtonian constant of gravity*, Science, 315, 2007, DOI: 10.1126/science.1135459.
- [116] G. Lamporesi, A. Bertoldi, L. Cacciapuoti, M. Prevedelli, and G. M. Tino, *Determination of the Newtonian gravitational constant using atom interferometry*, Phys. Rev. Lett., 2008, DOI: 10.1103/PhysRevLett.100.050801.

- [117] T. Müller, M. Gilowski, M. Zaiser, P. Berg, C. Schubert, T. Wendrich, W. Ertmer, and E. M. Rasel, *A compact dual atom interferometer gyroscope based on laser-cooled rubidium*, *Eur. Phys. J. D*, 2009, DOI: 10.1140/epjd/e2009-00139-0.
- [118] T. Lévêque, A. Gauguet, F. Michaud, F. Pereira Dos Santos, and A. Landragin, *Enhancing the area of a Raman atom interferometer using a versatile double-diffraction technique*, *Phys. Rev. Lett.*, 2009, DOI: 10.1103/PhysRevLett.103.080405.
- [119] J. K. Stockton, K. Takase, and M. A. Kasevich, *Absolute geodetic rotation measurement using atom interferometry*, *Phys. Rev. Lett.*, 2011, DOI: 10.1103/PhysRevLett.107.133001.
- [120] G. Tackmann, P. Berg, C. Schubert, S. Abend, M. Gilowski, W. Ertmer, and E. M. Rasel, *Self-alignment of a compact large-area atomic Sagnac interferometer*, *New J. Phys.*, 14, 2012, DOI: 10.1088/1367-2630/14/1/015002.
- [121] S. Dimopoulos, P. W. Graham, J. M. Hogan, M. A. Kasevich, and S. Rajendran, *Atomic gravitational wave interferometric sensor*, *Phys. Rev. D*, 2008, DOI: 10.1103/PhysRevD.78.122002.
- [122] P. Delva and E. Rasel, *Matter wave interferometry and gravitational waves*, *J. Mod. Opt.*, 56, 2009, DOI: doi:10.1080/09500340903326169.
- [123] J. Hogan, D. Johnson, S. Dickerson, T. Kovachy, A. Sugarbaker, S.-w. Chiow, P. Graham, M. Kasevich, B. Saif, S. Rajendran, P. Bouyer, B. Seery, L. Feinberg, and R. Keski-Kuha, *An atomic gravitational wave interferometric sensor in low earth orbit (AGIS-LEO)*, *Gen. Rel. Grav.*, 43, 2011, DOI: 10.1007/s10714-011-1182-x.
- [124] N. F. Ramsey, *A new molecular beam resonance method*, *Phys. Rev.*, 1949, DOI: 10.1103/PhysRev.76.996.
- [125] R. Hajima, N. Takeda, H. Ohashi, and M. Akiyama, *Optimization of wiggler magnets ordering using a genetic algorithm*, *Nucl. Instrum. Methods*, 318, 1992, DOI: 10.1016/0168-9002(92)91167-8.
- [126] A. Bacci, C. Maroli, V. Pettillo, A. Rossi, and L. Serafini, *Maximizing the brightness of an electron beam by means of a genetic algorithm*, *Nucl. Instrum. Methods*, 263, 2007, DOI: 10.1016/j.nimb.2007.07.006.
- [127] J. J. Gilijamse, J. Küpper, S. Hoekstra, N. Vanhaecke, S. Y. T. van de Meerakker, and G. Meijer, *Optimizing the Stark-decelerator beamline for the trapping of cold molecules using evolutionary strategies*, *Phys. Rev. A*, 2006, DOI: 10.1103/PhysRevA.73.063410.

- [128] R. A. Woolley, J. Stirling, A. Radocea, N. Krasnogor, and P. Moriarty, *Automated probe microscopy via evolutionary optimization at the atomic scale*, *Appl. Phys. Lett.*, 98, 2011, DOI: 10.1063/1.3600662.
- [129] D. Zeidler, S. Frey, K.-L. Kompa, and M. Motzkus, *Evolutionary algorithms and their application to optimal control studies*, *Phys. Rev. A*, 2001, DOI: 10.1103/PhysRevA.64.023420.
- [130] A. Assion, T. Baumert, M. Bergt, T. Brixner, B. Kiefer, V. Seyfried, M. Strehle, and G. Gerber, *Control of chemical reactions by feedback-optimized phase-shaped femtosecond laser pulses*, *Science*, 282, 1998, DOI: 10.1126/science.282.5390.919.
- [131] W. Rohringer, R. Bucker, S. Manz, T. Betz, C. Koller, M. Gobel, A. Perrin, J. Schmiedmayer, and T. Schumm, *Stochastic optimization of a cold atom experiment using a genetic algorithm*, *Appl. Phys. Lett.*, 93, 2008, DOI: 10.1063/1.3058756.
- [132] W. Rohringer, D. Fischer, M. Trupke, J. Schmiedmayer, and T. Schumm, *Stochastic optimization of Bose-Einstein condensation using a genetic algorithm*, In D. I. Dritsas, editor, *Stochastic Optimization - Seeing the optimal for the uncertain*. InTech, 2011, DOI: 10.5772/623.
- [133] P. B. Wigley, P. J. Everitt, A. Hengel, J. W. Bastian, M. A. Sooriyabandara, G. D. McDonald, K. S. Hardman, C. D. Quinlivan, M. Perumbil, C. C. N. Kuhn, I. R. Petersen, A. Luiten, J. J. Hope, N. P. Robins, and M. R. Hush, *Fast machine-learning online optimization of ultra-cold-atom experiments*, arXiv preprint arXiv:1507.04964, 2015.
- [134] I. Geisel, K. Cordes, J. Mahnke, S. Jöllenbeck, J. Ostermann, J. Arlt, W. Ertmer, and C. Klempt, *Evolutionary optimization of an experimental apparatus*, *Appl. Phys. Lett.*, 102, 2013, DOI: <http://dx.doi.org/10.1063/1.4808213>.
- [135] R. Storn and K. Price, *Differential evolution—a simple and efficient adaptive scheme for global optimisation over continuous spaces*, Technical report, 1995.
- [136] K. Price, R. Storn, and J. Lampinen, *Differential evolution: a practical approach to global optimization*. Springer-Verlag New York Inc, 2005, DOI: 10.1007/3-540-31306-0.
- [137] K. Cordes, P. Mikulastik, A. Vais, and J. Ostermann, *Extrinsic calibration of a stereo camera system using a 3D CAD model considering the uncertainties of estimated feature points*, 2009, DOI: 10.1109/CVMP.2009.10.
- [138] K. Zielinski and R. Laur, *Stopping criteria for differential evolution in constrained single-objective optimization*, In *Advances in differential evolution*, pages 111–138. Springer, 2008, DOI: 10.1007/978-3-540-68830-3\_4.

- 
- [139] D. H. Ackley, *A connectionist machine for genetic hillclimbing*. Kluwer Academic Publishers, Norwell, MA, USA, 1987, DOI: 10.1007/978-1-4613-1997-9.
- [140] Y. Jin and J. Branke, *Evolutionary optimization in uncertain environments—a survey*, IEEE Trans. Evol. Comput., 9, 2005, DOI: 10.1109/TEVC.2005.846356.
- [141] S. Das, A. Konar, and U. Chakraborty, *Improved differential evolution algorithms for handling noisy optimization problems*, 2, 2005, DOI: 10.1109/CEC.2005.1554892.
- [142] S. Jöllenbeck, *Eine Quelle Bose-Einstein-kondensierter Ensembles auf Basis eines mesoskopischen Atomchips*, PhD thesis, Leibniz Universität Hannover, 2012.
- [143] J. Mahnke, *A continuously pumped reservoir of ultracold atoms*, PhD thesis, Leibniz Universität Hannover, 2015.
- [144] I. Geisel, *Präparation eines magnetisch geführten Strahls ultrakalter Atome*, Master's thesis, Leibniz Universität Hannover, 2011.
- [145] R. Olf, F. Fang, G. E. Marti, A. MacRae, and D. M. Stamper-Kurn, *Thermometry and cooling of a Bose gas to 0.02 times the condensation temperature*, Nature Physics, 11, 2015, DOI: 10.1038/nphys3408.
- [146] S. Armstrong, M. Wang, R. Y. Teh, Q. Gong, Q. He, J. Janousek, H.-A. Bachor, M. D. Reid, and P. K. Lam, *Multipartite Einstein-Podolsky-Rosen steering and genuine tripartite entanglement with optical networks*, Nature Phys., 2015, DOI: 10.1038/nphys3202.
- [147] S. Armstrong, J.-F. Morizur, J. Janousek, B. Hage, N. Treps, P. K. Lam, and H.-A. Bachor, *Programmable multimode quantum networks*, Nat. Commun., 3, 2012, DOI: 10.1038/ncomms2033.
- [148] C. K. Hong, Z. Y. Ou, and L. Mandel, *Measurement of subpicosecond time intervals between two photons by interference*, Phys. Rev. Lett., 1987, DOI: 10.1103/PhysRevLett.59.2044.
- [149] R. J. Lewis-Swan and K. V. Kheruntsyan, *Proposal for demonstrating the Hong-Ou-Mandel effect with matter waves*, Nat. Commun., 5, 2014, DOI: 10.1038/ncomms4752.
- [150] R. Lopes, A. Imanaliev, A. Aspect, M. Cheneau, D. Boiron, and C. I. Westbrook, *Atomic Hong-Ou-Mandel experiment*, Nature, 520, 2015, DOI: 10.1038/nature14331.
- [151] B. H. Liu, F. W. Sun, Y. X. Gong, Y. F. Huang, G. C. Guo, and Z. Y. Ou, *Four-photon interference with asymmetric beam splitters*, Opt. Lett., 2007, DOI: 10.1364/OL.32.001320.

- [152] K. Banaszek and K. Wódkiewicz, *Testing quantum nonlocality in phase space*, Phys. Rev. Lett., 1999, DOI: 10.1103/PhysRevLett.82.2009.
- [153] S.-W. Lee, H. Jeong, and D. Jaksch, *Testing quantum nonlocality by generalized quasiprobability functions*, Phys. Rev. A, 2009, DOI: 10.1103/PhysRevA.80.022104.
- [154] J. B. Brask and R. Chaves, *Robust nonlocality tests with displacement-based measurements*, Phys. Rev. A, 2012, DOI: 10.1103/PhysRevA.86.010103.
- [155] J. Peise, B. Lücke, L. Pezzè, F. Deuretzbacher, W. Ertmer, J. Arlt, A. Smerzi, L. Santos, and C. Klempt, *Interaction-free measurements by quantum Zeno stabilisation of ultracold atoms*, Nat. Commun., 6, 2015, DOI: 10.1038/ncomms7811.



# LIST OF PUBLICATIONS

---

- J. Peise, I. Kruse, K. Lange, B. Lücke, L. Pezzè, J. Arlt, W. Ertmer, K. Hammerer, L. Santos, A. Smerzi, C. Klempt,  
*Satisfying the Einstein-Podolsky-Rosen criterion with massive particles*  
Nat. Commun. **6**, 8984 (2015),  
DOI: 10.1038/ncomms9984
- J. Mahnke, I. Kruse, A. Hüper, S. Jöllenbeck, W. Ertmer, J. Arlt, C. Klempt,  
*A continuously pumped reservoir of ultracold atoms*  
J. Phys. B: At. Mol. Opt. Phys. **48**, 165301 (2015),  
DOI: 10.1088/0953-4075/48/16/165301
- J. Mahnke, S. Kulas, I. Geisel, S. Jöllenbeck, W. Ertmer, C. Klempt,  
*Microwave sidebands for laser cooling by direct modulation of a tapered amplifier*  
Rev. Sci. Instrum. **84**, 063110 (2013),  
DOI: 10.1063/1.4811196
- I. Geisel, K. Cordes, J. Mahnke, S. Jöllenbeck, J. Ostermann, J. Arlt, W. Ertmer, C. Klempt,  
*Evolutionary optimization of an experimental apparatus*  
Appl. Phys. Lett. **102**, 214105 (2013),  
DOI: 10.1063/1.4808213



# CURRICULUM VITAE

---

## Personal Details

Name Ilka Kruse, née Geisel  
Date of birth October 5, 1987  
Place of birth Hamburg, Germany

## Education

07/2011 - 12/2015 Doctoral studies at Institut für Quantenoptik , Leibniz  
Universität Hannover  
05/2012 - 10/2012 Visiting scientist at University of Maryland, MD, USA  
10/2009 - 07/2011 Master's studies at Leibniz Universität Hannover  
07/2009 - 10/2009 Summer student program at DESY, Hamburg  
09/2008 - 01/2009 Bachelor's studies at National University of Ireland,  
Maynooth, Ireland  
10/2006 - 09/2009 Bachelor's studies at Leibniz Universität Hannover  
07/2006 Abitur at Gymnasium Julianum, Helmstedt

